

Jordan Journal of P H Y S I C S

An International Peer-Reviewed Research Journal

Volume 10, No. 3, Dec. 2017, Rabi Al-Awaal 1439 H

Jordan Journal of Physics (JJP): An International Peer-Reviewed Research Journal funded by the Scientific Research Support Fund, Jordan, and published biannually by the Deanship of Research and Graduate Studies, Yarmouk University, Irbid, Jordan.

EDITOR-IN-CHIEF:

Ibrahim O. Abu Al-Jarayesh

Department of Physics, Yarmouk University, Irbid, Jordan.

ijaraysh@yu.edu.jo

EDITORIAL BOARD:

Dia-Eddin M. Arafah

President, AL- al Bait University, Mafrq, Jordan.

darafah@ju.edu.jo

Nabil Y. Ayoub

President, American University of Madaba, Madaba, Jordan.

nabil.ayoub@gu.edu.jo

Jamil M. Khalifeh

Department of Physics, University of Jordan, Amman, Jordan.

jkhalifa@ju.edu.jo

Sami H. Mahmood

Department of Physics, University of Jordan, Amman, Jordan.

s.mahmood@ju.edu.jo

Nihad A. Yusuf

Princess Sumaya University for Technology, Amman, Jordan.

E-mail: n.yusuf@psut.edu.jo

Marwan S. Mousa

Department of Physics, Mu'tah University, Al-Karak, Jordan.

mmousa@mutah.edu.jo

Akram A. Rousan

Department of Applied Physical Sciences, Jordan University Of Science and Technology, Irbid, Jordan.

akram@just.edu.jo

Mohammad Al-Sugheir

Department of Physics, The Hashemite University, Zarqa, Jordan.

msugh@hu.edu.jo

EDITORIAL SECRETARY: Majdi Al-Shannaq.

Manuscripts should be submitted to:

Prof. Ibrahim O. Abu Al-Jarayesh
Editor-in-Chief, Jordan Journal of Physics
Deanship of Research and Graduate Studies
Yarmouk University-Irbid-Jordan
Tel. 00 962 2 7211111 Ext. 2075
E-mail: jjp@yu.edu.jo
Website: <http://Journals.yu.edu.jo/jjp>

Jordan Journal of P H Y S I C S

An International Peer-Reviewed Research Journal

Volume 10, No. 3, Dec. 2017, Rabi Al-Awaal 1439 H

INTERNATIONAL ADVISORY BOARD

Prof. Dr. Ahmad Saleh

Department of Physics, Yarmouk University, Irbid, Jordan.
salema@yu.edu.jo

Prof. Dr. Aurore Savoy-Navarro

LPNHE Université de Paris 6/IN2P3-CNRS, Tour 33, RdC 4,
Place Jussieu, F 75252, Paris Cedex 05, France.
auore@lphnhe.in2p3.fr

Prof. Dr. Bernard Barbara

Laboratoire Louis Neel, Salle/Room: D 108, 25, Avenue des
Martyrs BP 166, 38042-Grenoble Cedex 9, France.
Barbara@grenoble.cnrs.fr

Prof. Dr. Bruno Guiderdoni

Observatoire Astronomique de Lyon, g, avenue Ch. Antre-F-69561,
Saint Genis Laval Cedex, France.
Bruno.guiderdoni@olos.univ-lyon1.fr

Prof. Dr. Buford Price

Physics Department, University of California, Berkeley, CA 94720,
U. S. A.
bprice@berkeley.edu

Prof. Dr. Colin Cough

School of Physics and Astronomy, University of Birmingham, B15
2TT, U. K.
c.gough@bham.ac.uk

Prof. Dr. Desmond Cook

Department of Physics, Condensed Matter and Materials Physics
Research Group, Old Dominion University, Norfolk, Virginia
23529, U. S. A.
Dcook@physics.odu.edu

Prof. Dr. Evgeny Sheshin

MIPT, Institutskij per. 9, Dogoprudnyi 141700, Russia.
sheshin@lafeet.mipt.ru

Prof. Dr. Hans Ott

Laboratorium fuer Festkorperphysik, ETH Honggerberg, CH-
8093 Zurich, Switzerland.
ott@solid.phys.ethz.ch

Prof. Dr. Herwig Schopper

President SESAME Council, Chairman Scientific Board UNESCO
IBSP Programme, CERN, 1211 Geneva, Switzerland.
Herwig.Schopper@cern.ch

Prof. Dr. Humam Ghassib

Department of Physics, The University of Jordan, Amman 11942,
Jordan.
humamg@ju.edu.jo

Prof. Dr. Ingo Hofmann

GSI Darmstadt, Planckstr. 1, 64291, Darmstadt, Germany.
i.hofmann@gsi.de

Prof. Dr. Jozef Lipka

Department of Nuclear Physics and Technology, Slovak University
of Technology, Bratislava, Ilkovicova 3, 812 19 Bratislava,
Slovakia.
Lipka@elf.stuba.sk

Prof. Dr. Khalid Touqan

Chairman of Jordan Atomic Energy Commission, Amman, Jordan.

Prof. Dr. Mark J. Hagmann

Desert Electronics Research Corporation, 762 Lacey Way, North
Salt Lake 84064, Utah, U. S. A.
MHagmann@NewPathResearch.Com

Prof. Dr. Nasr Zubeidey

President: Al-Zaytoonah University of Jordan, Amman, Jordan.
President@alzaytoonah.edu.jo

Prof. Dr. Patrick Roudeau

Laboratoire de l'Accelérateur, Lineaire (LAL), Université Paris-
Sud 11, Batiment 200, 91898 Orsay Cedex, France.
roudeau@mail.cern.ch

Prof. Dr. Paul Chu

Department of Physics, University of Houston, Houston, Texas
77204-5005, U. S. A.
Ching-Wu.Chu@mail.uh.edu

Prof. Dr. Peter Dowben

Nebraska Center for Materials and Nanoscience, Department of
Physics and Astronomy, 255 Behlen Laboratory (10th and R
Streets), 116 Brace Lab., P. O. Box 880111, Lincoln, NE 68588-
0111, U. S. A.
pdowben@unl.edu

Prof. Dr. Peter Mulser

Institute fuer Physik, T.U. Darmstadt, Hochschulstr. 4a, 64289
Darmstadt, Germany.
Peter.mulser@physik.tu-darmstadt.de

Prof. Dr. Rasheed Azzam

Department of Electrical Engineering, University of New Orleans
New Orleans, Louisiana 70148, U. S. A.
razzam@uno.edu

Dr. Richard G. Forbes

University of Surrey, FEPS (X1), Guildford, Surrey GU2 7XH,
U. K.
R.Forbes@surrey.ac.uk

Prof. Dr. Roy Chantrell

Physics Department, York University, York, YO10 5DD, U. K.
Rc502@york.ac.uk

Prof. Dr. Shawqi Al-Dallal

Department of Physics, Faculty of Science, University of Bahrain,
Manamah, Kingdom of Bahrain.

Prof. Dr. Susamu Taketomi

Matsumoto Yushi-Seiyaku Co. Ltd., Shibukawa-Cho, Yao City,
Osaka 581-0075, Japan.
staketomi@hotmail.com

Prof. Dr. Wolfgang Nolting

Institute of Physics / Chair: Solid State Theory, Humboldt-
University at Berlin, Newtonstr. 15 D-12489 Berlin, Germany
Wolfgang.nolting@physik.hu-berlin.de



The Hashemite Kingdom of Jordan



Yarmouk University

Jordan Journal of PHYSICS

An International Peer-Reviewed Research Journal
Funded by the Scientific Research Support Fund

Volume 10, No. 3, Dec. 2017, Rabi Al-Awaal 1439 H

Instructions to Authors

Instructions to authors concerning manuscript organization and format apply to hardcopy submission by mail, and also to electronic online submission via the Journal homepage website (<http://jip.yu.edu.jo>).

Manuscript Submission

1- **E-mail to :** jip@yu.edu.jo

2- **Online:** Follow the instructions at the journal homepage website.

Original *Research Articles*, *Communications* and *Technical Notes* are subject to critical review by minimum of two competent referees. Authors are encouraged to suggest names of competent reviewers. *Feature Articles* in active Physics research fields, in which the author's own contribution and its relationship to other work in the field constitute the main body of the article, appear as a result of an invitation from the Editorial Board, and will be so designated. The author of a *Feature Article* will be asked to provide a clear, concise and critical status report of the field as an introduction to the article. *Review Articles* on active and rapidly changing Physics research fields will also be published. Authors of *Review Articles* are encouraged to submit two-page proposals to the Editor-in-Chief for approval. Manuscripts submitted in *Arabic* should be accompanied by an Abstract and Keywords in English.

Organization of the Manuscript

Manuscripts should be typed double spaced on one side of A4 sheets (21.6 x 27.9 cm) with 3.71 cm margins, using Microsoft Word 2000 or a later version thereof. The author should adhere to the following order of presentation: Article Title, Author(s), Full Address and E-mail, Abstract, PACS and Keywords, Main Text, Acknowledgment. Only the first letters of words in the Title, Headings and Subheadings are capitalized. Headings should be in **bold** while subheadings in *italic* fonts.

Title Page: Includes the title of the article, authors' first names, middle initials and surnames and affiliations. The affiliation should comprise the department, institution (university or company), city, zip code and state and should be typed as a footnote to the author's name. The name and complete mailing address, telephone and fax numbers, and e-mail address of the author responsible for correspondence (designated with an asterisk) should also be included for official use. The title should be carefully, concisely and clearly constructed to highlight the emphasis and content of the manuscript, which is very important for information retrieval.

Abstract: A one paragraph abstract not exceeding 200 words is required, which should be arranged to highlight the purpose, methods used, results and major findings.

Keywords: A list of 4-6 keywords, which expresses the precise content of the manuscript for indexing purposes, should follow the abstract.

PACS: Authors should supply one or more relevant PACS-2006 classification codes, (available at <http://www.aip.org/pacs/pacs06/pacs06-toc.html>)

Introduction: Should present the purpose of the submitted work and its relationship to earlier work in the field, but it should not be an extensive review of the literature (e.g., should not exceed 1 ½ typed pages).

Experimental Methods: Should be sufficiently informative to allow competent reproduction of the experimental procedures presented; yet concise enough not to be repetitive of earlier published procedures.

Results: should present the results clearly and concisely.

Discussion: Should be concise and focus on the interpretation of the results.

Conclusion: Should be a brief account of the major findings of the study not exceeding one typed page.

Acknowledgments: Including those for grant and financial support if any, should be typed in one paragraph directly preceding the References.

References: References should be typed double spaced and numbered sequentially in the order in which they are cited in the text. References should be cited in the text by the appropriate Arabic numerals, enclosed in square brackets. Titles of journals are abbreviated according to list of scientific periodicals. The style and punctuation should conform to the following examples:

1. Journal Article:

- a) Heisenberg, W., Z. Phys. 49 (1928) 619.
- b) Bednorz, J. G. and Müller, K. A., Z. Phys. B64 (1986) 189
- c) Bardeen, J., Cooper, L.N. and Schrieffer, J. R., Phys. Rev. 106 (1957) 162.
- d) Asad, J. H., Hijawi, R. S., Sakaji, A. and Khalifeh, J. M., Int. J. Theor. Phys. 44(4) (2005), 3977.

2. Books with Authors, but no Editors:

- a) Kittel, C., "Introduction to Solid State Physics", 8th Ed. (John Wiley and Sons, New York, 2005), chapter 16.
- b) Chikazumi, S., C. D. Graham, JR, "Physics of Ferromagnetism", 2nd Ed. (Oxford University Press, Oxford, 1997).

3. Books with Authors and Editors:

- a) Allen, P. B. "Dynamical Properties of Solids", Ed. (1), G. K. Horton and A. A. Maradudin (North-Holland, Amsterdam, 1980), p137.
- b) Chantrell, R. W. and O'Grady, K., "Magnetic Properties of Fine Particles" Eds. J. L. Dormann and D. Fiorani (North-Holland, Amsterdam, 1992), p103.

4. Technical Report:

Purcell, J. "The Superconducting Magnet System for the 12-Foot Bubble Chamber", report ANL/HEP6813, Argonne Natl. Lab., Argonne, III, (1968).

5. Patent:

Bigham, C. B., Schneider, H. R., US patent 3 925 676 (1975).

6. Thesis:

Mahmood, S. H., Ph.D. Thesis, Michigan State University, (1986), USA (Unpublished).

7. Conference or Symposium Proceedings:

Blandin, A. and Lederer, P. Proc. Intern. Conf. on Magnetism, Nottingham (1964), P.71.

8. Internet Source:

Should include authors' names (if any), title, internet website, URL, and date of access.

9. Prepublication online articles (already accepted for publication):

Should include authors' names (if any), title of digital database, database website, URL, and date of access.

For other types of referenced works, provide sufficient information to enable readers to access them.

Tables: Tables should be numbered with Arabic numerals and referred to by number in the Text (e.g., Table 1). Each table should be typed on a separate page with the legend above the table, while explanatory footnotes, which are indicated by superscript lowercase letters, should be typed below the table.

Illustrations: Figures, drawings, diagrams, charts and photographs are to be numbered in a consecutive series of Arabic numerals in the order in which they are cited in the text. Computer-generated illustrations and good-quality digital photographic prints are accepted. They should be black and white originals (not photocopies) provided on separate pages and identified with their corresponding numbers. Actual size graphics should be provided, which need no further manipulation, with lettering (Arial or Helvetica) not smaller than 8 points, lines no thinner than 0.5 point, and each of uniform density. All colors should be removed from graphics except for those graphics to be considered for publication in color. If graphics are to be submitted digitally, they should conform to the following minimum resolution requirements: 1200 dpi for black and white line art, 600 dpi for grayscale art, and 300 dpi for color art. All graphic files must be saved as TIFF images, and all illustrations must be submitted in the actual size at which they should appear in the journal. Note that good quality hardcopy original illustrations are required for both online and mail submissions of manuscripts.

Text Footnotes: The use of text footnotes is to be avoided. When their use is absolutely necessary, they should be typed at the bottom of the page to which they refer, and should be cited in the text by a superscript asterisk or multiples thereof. Place a line above the footnote, so that it is set off from the text.

Supplementary Material: Authors are encouraged to provide all supplementary materials that may facilitate the review process, including any detailed mathematical derivations that may not appear in whole in the manuscript.

Revised Manuscript and Computer Disks

Following the acceptance of a manuscript for publication and the incorporation of all required revisions, authors should submit an original and one more copy of the final disk containing the complete manuscript typed double spaced in Microsoft Word for Windows 2000 or a later version thereof. All graphic files must be saved as PDF, JPG, or TIFF images.

Allen, P.B., “.....”, in: Horton, G.K., and Muradudin, A. A., (eds.), “Dynamical.....”, (North.....), pp....

Reprints

Twenty (20) reprints free of charge are provided to the corresponding author. For orders of more reprints, a reprint order form and prices will be sent with the article proofs, which should be returned directly to the Editor for processing.

Copyright

Submission is an admission by the authors that the manuscript has neither been previously published nor is being considered for publication elsewhere. A statement transferring copyright from the authors to Yarmouk University is required before the manuscript can be accepted for publication. The necessary form for such transfer is supplied by the Editor-in-Chief. Reproduction of any part of the contents of a published work is forbidden without a written permission by the Editor-in-Chief.

Disclaimer

Opinions expressed in this Journal are those of the authors and neither necessarily reflects the opinions of the Editorial Board or the University, nor the policy of the Higher Scientific Research Committee or the Ministry of Higher Education and Scientific Research. The publisher shoulders no responsibility or liability whatsoever for the use or misuse of the information published by JJP.

Indexing

JJP is currently indexing in:

- 1- **Emerging Sources Citation Index (ESCI)**



Jordan Journal of P H Y S I C S

An International Peer-Reviewed Research Journal

Volume 10, No. 3, Dec. 2017, Rabi Al-Awaal 1439 H

Table of Contents:

Communication	Pages
Reflectance Enhancement Factor Associated with Coherent Interference of Light in an Unbacked or Embedded Quarter-Wave Layer R. M. A. Azzam	113-116
English Articles	Pages
Estimation of Natural and Anthropogenic Exposures to Gamma Ray from a High Agricultural Area in Jordan "Bani-Kananah District" Hamed S. Hamadneh, Molham M. Eyadeh, Manal J. Abdallah and Omar A. Al-Khidrat	117-125
Semi-Quantitative Analysis for Pottery Fragments Excavated at Udhruh Site, Jordan Using Non-destructive SR-XRF Analysis Employing Multivariate Statistical Methods K. AbuSaleem, A. Aldrabee, A. Wriekat, M. Tarawneh and F. Abudanah	127-137
Assessment of Indoor Radon Levels in Selected Locations within Lagos State University, Ojo, Lagos M. A. Olaoye, T. J. Aluko, O. A. Jegede, M. F. Agbesi and O. O. Ajayi	139-141
Fuel Ignition Conditions in Thermonuclear Fusion M. Mahdavi	143-151
Assessment of Human Exposures to Radiation Arising from Radon in Groundwater Samples from Parts of Abeokuta, Ogun State, Nigeria J. A. Rabi, O. A. Mustapha, V. Makinde and A.M. Gbadebo	153-164
Electromagnetic Transmission from a Dielectric Loaded Resistive Cylindrical Pipe M. S. Bawa'aneh, A. M. Al-Khateeb and N. Laham	165-172

Reflectance Enhancement Factor Associated with Coherent Interference of Light in an Unbacked or Embedded Quarter-Wave Layer

R. M. A. Azzam

Department of Electrical Engineering, University of New Orleans, New Orleans, Louisiana 70148, USA.

Received on: 12/1/2017;

Accepted on: 28/3/2017

Abstract: If a semi-infinite transparent substrate is replaced by a quarter-wave layer (QWL) of the same material, which is embedded in the same ambient, the intensity reflectance is increased by a significant factor. A simple expression is derived for this reflectance enhancement factor (REF) η that results from coherent multiple-beam interference of monochromatic light within the QWL. The REF η is a monotonically decreasing function of the Fresnel intensity reflectance at the ambient-layer interface with maximum and minimum values of 4 and 1, respectively. The expression for η is applicable for the p and s linear polarizations, at any angle of incidence and for any wavelength within the common transparency bandwidth of both layer and ambient. The results are particularly relevant to light reflection by index-near-one materials and Brewster-angle reflection polarizers that use high-index, IR-transparent semiconductors such as Ge and Si, in bulk and pellicle form.

Keywords: Interference, Reflection, Polarization, Thin films.

Introduction

Thin film optics is a well-established field with many important applications (see, e.g. [1 – 5]). For example, it is well known that the reflectance of a surface can be deliberately increased or decreased by exploiting the coherent interference of light in transparent thin films.

In this paper, an expression is derived for the reflectance enhancement factor (REF) that results when a semi-infinite transparent substrate is replaced by an unbacked quarter-wave layer (QWL) of the same material. The functional expression of the REF, associated with coherent multiple-beam interference in the QWL, is independent of incident light polarization (p or s), wavelength and angle of incidence. The significance of the REF is demonstrated by two examples: (a) the reflection of light by index-near-one (INO) skeletal or porous materials [6] and (b) Brewster-angle reflection polarizers that use high-index, IR-transparent semiconductor

materials both in bulk and thin-film (pellicle) form.

Reflectance Enhancement Factor

The reflection of p - and s -polarized monochromatic light at the planar interface between two transparent media (e.g. air and glass, denoted by 0 and 1) at an angle of incidence ϕ is governed by the well-known Fresnel reflection coefficients $r_{01\nu}$, $\nu = p, s$ [7].

If the semi-infinite substrate is truncated to a thin film of uniform thickness d and the exit medium below the dashed line in Fig. 1 is the same as the ambient medium 0, the complex-amplitude reflection coefficients that account for coherent multiple reflections within the unbacked layer are given by [8]:

$$R_{\nu} = \frac{r_{01\nu}(1-X)}{(1-r_{01\nu}^2 X)}, \nu = p, s. \quad (1)$$

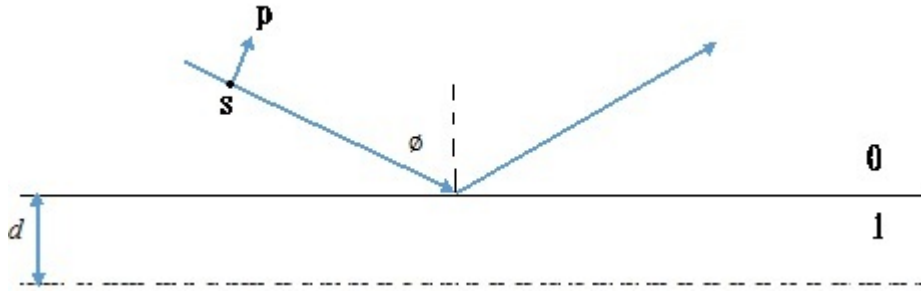


FIG. 1. Reflection of p - and s -polarized light at the interface between two transparent media 0 and 1. Reflectance enhancement due to the coherent interference of light within a truncated slab of thickness d (and exit medium 0) is the subject of this paper. In this figure, the s polarization is normal to the page; i.e., the plane of incidence.

In Eq. (1), X is a complex periodic function of film thickness d :

$$X = \exp(-i2\pi d / D_\phi), \quad (2)$$

with a period given by:

$$D_\phi = (\lambda/2)(n_1^2 - n_0^2 \sin^2 \phi)^{-1/2}. \quad (3)$$

In Eq. (3), λ is the wavelength of light, while n_0 and n_1 are the refractive indices of the transparent media of incidence and refraction, respectively.

For a layer of half-wave optical thickness [$d = D_\phi$ and $X = 1$ from Eq. (2)], destructive interference leads to zero reflectance, $R_\nu = 0$, $\nu = p, s$, according to Eq. (1).

On the other hand, the highest reflectance is achieved with a quarter-wave layer (QWL) of thickness $d = D_\phi / 2$ and $X = -1$ [from Eq. (2)]. Substitution of $X = -1$ in Eq. (1) leads to the desired expression:

$$R_\nu = \frac{2r_{01\nu}^2}{(1 + r_{01\nu}^2)^2}, \nu = p, s. \quad (4)$$

The relation between the intensity reflectance of a QWL and that of a semi-infinite substrate ($d \rightarrow \infty$) of the same refractive index is obtained by squaring both sides of Eq. (4):

$$R_\nu^2 = \frac{4r_{01\nu}^2}{(1 + r_{01\nu}^2)^2}, \nu = p, s. \quad (5)$$

The reflectance enhancement factor (REF) η is defined by:

$$\eta = R_\nu^2 / r_{01\nu}^2 = 4 / (1 + r_{01\nu}^2)^2, \nu = p, s. \quad (6)$$

For simplicity, the intensity reflectance of the 01 interface for the ν polarization is denoted by:

$$x = r_{01\nu}^2, \quad (7)$$

so that the REF η becomes:

$$\eta = 4 / (1 + x)^2. \quad (8)$$

The REF of Eq. (8) is applicable for: (a) the p and s orthogonal linear polarizations, parallel and perpendicular to the plane of incidence, respectively; (b) any angle of incidence ϕ of external reflection ($n_1 > n_0$) or partial internal reflection below the critical angle in the case of an embedded low-index layer [$n_1 < n_0, \phi < \arcsin(n_1 / n_0)$]; and (c) any wavelength of incident light or refractive indices of the two transparent media.

For a given interface between two transparent media $r_{01p}^2 \leq r_{01s}^2$ at all angles of incidence [7], hence from Eqs. (7) and (8) one obtains:

$$\eta_p \geq \eta_s. \quad (9)$$

Fig. 2 shows a graph of the REF η over the full range of $x = r_{01\nu}^2$ ($0 \leq x \leq 1$). In Fig. 2, the maximum value $\eta = 4$ is attained in the limit as $x \rightarrow 0$ and the minimum value $\eta = 1$ in the limit as $x \rightarrow 1$ and the initial and final slopes of the η -versus- x curve in Fig. 2 are -8 and -1 , respectively.

Two examples are given in the next section that illustrate the significance of the REF.

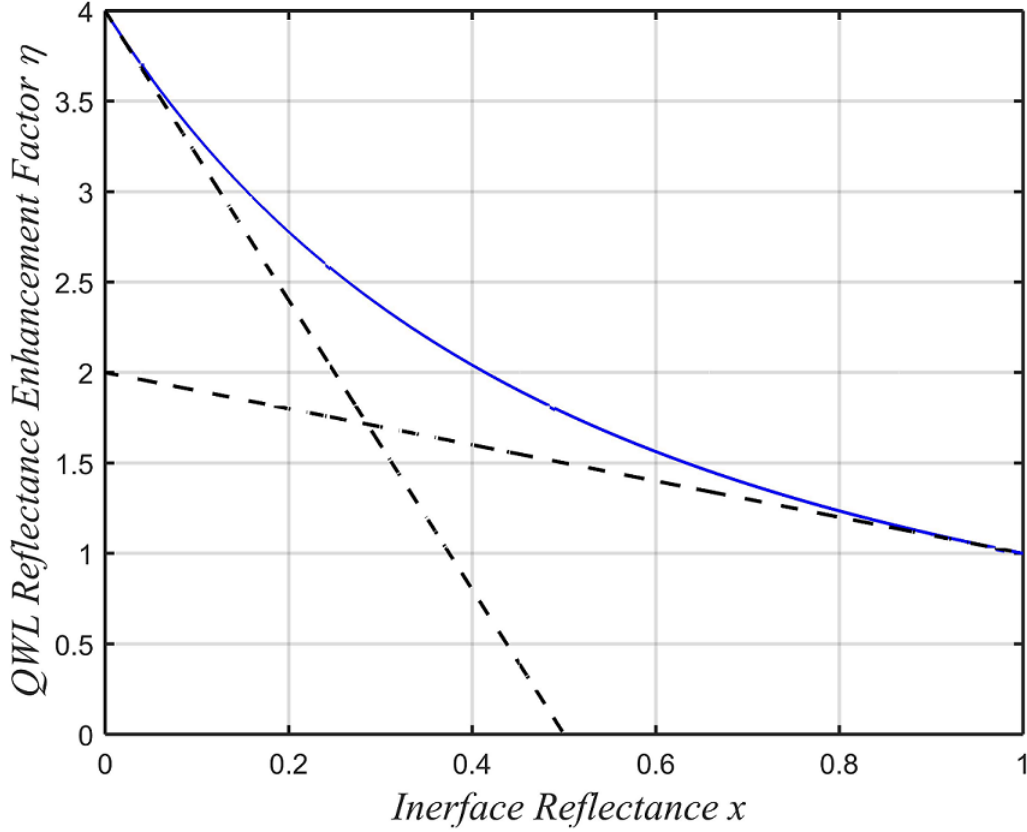


FIG. 2. Reflectance enhancement factor η [Eq. (8)] due to coherent interference of light in a QWL is plotted as a function of the intensity reflectance of the ambient-layer interface $x = r_{0lv}^2$.

Reflection by Index-Near-One Materials and Bulk-versus-Pellicle Brewster-Angle Reflection Polarizers

Except near grazing incidence, the reflection of light by a skeletal or porous index-near-one (INO) material [6] is very weak. For example, the intensity reflectance of s -polarized light at the interface between air and a bulk INO material with $n = 1.1$ at 60° angle of incidence is only $r_{0ls}^2 = 0.02288$. On the other hand, if the theoretically semi-infinite INO substrate is replaced by a QWL of the same refractive index ($n = 1.1$), the intensity reflectance is boosted by a significant factor of $\eta_s = 3.911$ or nearly 6 dB.

As another example, consider the simplest method for generating linearly polarized light by reflection at the Brewster angle (BA) $\phi_B = \arctan(n); n = n_1/n_0$ of an air-dielectric plane boundary. At the BA, the p polarization is suppressed on reflection ($r_{0lp} = 0$) and the reflected light is s polarized. The intensity reflectance for the s polarization at the BA is given by:

$$r_{0ls}^2 = \cos^2(2\phi_B) = (n^2 - 1)^2 / (n^2 + 1)^2. \quad (10)$$

For an *efficient* BA polarizer, the s reflectance of Eq. (10) should be as high as possible. This is feasible only with high-index, IR-transparent semiconductors [9, 10] such as Si and Ge with $n \approx 3.4$ and 4, respectively.

For bulk Ge BA reflection polarizer ($n = 4$), Eq. (10) gives $r_{0ls}^2 = 0.7785$, which may be considered sufficiently high. However, the s reflectance of the Ge substrate at the BA (75.964°) can be enhanced by replacing bulk Ge by an unbacked Ge pellicle of QWL thickness. (At the BA, a transparent layer or parallel slab of *any* thickness is, of course, *non-reflecting* for the p polarization.) Substitution of $r_{0ls}^2 = 0.7785$ in Eq. (6) gives a REF for the s polarization of $\eta_s = 1.2645$. Therefore, the enhanced s reflectance of the QWL Ge pellicle BA polarizer is $\eta_s r_{0ls}^2 = 1.2645 \times 0.7785 = 0.9844$. This 20.6% increase in efficiency of the BA polarizer is clearly traceable to coherent multiple-beam interference of s -polarized light within the Ge QWL.

Conclusion

In this communication, a reflectance enhancement factor η [Eq. (8)] is introduced to quantify the role of coherent multiple-beam interference in augmenting the intensity reflectance of an unbacked or embedded QWL, when compared to the intensity reflectance of a semi-infinite substrate of the same material as the QWL. The result is valid for the p or s linear polarizations, at any angle of incidence or

wavelength within the common transparency spectral range of the media of incidence and refraction. The results are particularly relevant to light reflection by index-near-one (INO) materials and Brewster-angle reflection polarizers that use high-index, IR-transparent semiconductors, such as Ge and Si, in bulk and pellicle form.

References

- [1] Heavens, O.S., "Optical Properties of Thin Solid Films", (Dover, New York, 1965).
- [2] Knittl, Z., "Optics of Thin Films", (Wiley, New York, 1976).
- [3] Dobrowolski, J.A., in "Handbook of Optics", Vol. II, Bass, M.E., Van Stryland, W., Williams, D.R. and Wolfe, W.L., eds., (McGraw-Hill, New York, 1995).
- [4] Macleod, H. A., "Thin Film Optical Filters", (Institute of Physics, Bristol, 2001).
- [5] Piegari, A. and Flory, F., eds., "Optical Thin Film Coatings: From Materials to Applications", (Woodhead Publishing, Cambridge, 2013).
- [6] Schubert, E.F., Kim, J.K. and Xi, J.-Q., Phys. Stat. Sol. (b), 244 (2007) 3002.
- [7] Azzam, R.M.A. and Bashara, N.M., "Ellipsometry and Polarized Light", (North-Holland, Amsterdam, 1987).
- [8] Azzam, R.M.A. and Sudradjat, F.F., Appl. Opt., 47 (2008) 1103.
- [9] Bennet, J.M., in "Handbook of Optics", Vol. I, Chap. 12, Bass, M. and Mahajan, V.N., eds., (McGraw-Hill, New York, 2010).
- [10] Baumel, R.T. and Schnatterly, S.E., J. Opt. Soc. Am., 61 (1971) 832.

Estimation of Natural and Anthropogenic Exposures to Gamma Ray from a High Agricultural Area in Jordan "Bani-Kananah District"

Hamed S. Hamadneh^a, Molham M. Eyadeh^a, Manal J. Abdallah^a and Omar A. Al-Khidrat^b

^a Physics Department., Yarmouk University, Irbid 211-63, Jordan.

^b Ministry of Education, Amman, Jordan.

Received on: 26/12/2016;

Accepted on: 20/7/2017

Abstract: The activity concentrations of some artificial and natural radionuclides in some soil samples from high agricultural area, in North West Jordan "Bani-Kananah District", were measured by using gamma ray spectrometry. The activity concentrations of ¹³⁷Cs (Cesium), ⁴⁰K (Potassium), ²³⁸U (Uranium) and ²³²Th (Thorium) were measured in 38 soil samples which were collected from agricultural area. The radiation hazard indices of soil samples were also calculated. The results showed that the average values of either radionuclides activity concentrations or radiation hazard indices of all soil samples under study were in the internationally allowable and lower range. From the accumulated spectra, the activity concentrations were determined in (Bq/kg) to be on the average of 22.7 ± 15.2 for ²³²Th, 20.4 ± 9.8 for ²³⁸U, 160 ± 76 for ⁴⁰K and 4.6 ± 5.0 for ¹³⁷Cs. The mean value of the radium equivalent activity index (Ra_{eq}) was found to be 65.0 ± 27.8 Bq/kg, while the average value of the total absorbed dose (D) was 30.5 ± 13.1 nGy/h. In addition, the average value of the annual effective dose was 37.4 ± 16.0 μ Sv/y. The calculated values of external and internal radiation hazard indices (H_{ex} and H_{in}) were lower than unity. Results therefore emphasize that the radionuclide activity found in the surveyed area is nominal and does not pose any potential health hazard to the general public. This work can be added to other works on Jordan environment in order to establish baseline data for levels of radioactivity.

Keywords: Gamma ray spectrometry, Radionuclides, Hazard indices, Soil.

PACS number: 29.30.Kv

Introduction

Environmental radioactivity and the correlated gamma radiation exposure appear at different levels in each area in the world [1]. Therefore, estimating a baseline level of gamma radiation is behind the extended surveys taken worldwide. In addition, the evaluation of radiation dose distribution is important for assessing the health risk to the general public and serves as a reference in environmental radioactivity [2], especially for humans that maybe exposed to irradiation by contamination of the food chain which happens as a deposition of radionuclides from contaminated soil,

sediment or water on the plant leaves and root uptake [3].

Natural radionuclides are present mostly in soils since the foundation of earth; they are entering the human body during the food chain by the plant roots such as potassium radioisotope ⁴⁰K [4]. The main potential hazard of the natural radioactive series (uranium, thorium and actinium) is from external exposure; they enter in many building materials or by direct exposure to soil [5]. Artificial radionuclides, ¹³⁷Cs in particular, are released to the atmosphere from various sources such as medical waste, nuclear accidents like Chernobyl and Fukushima and

nuclear weapons testing in the 1950s and 1960s [5]. Since ^{137}Cs has a long half life time (30.2 y), it is a significant health pose when the level of internal exposure of human increases due to the intake of contaminated food stuff after the migration of radiocesium into soil [6].

Previous radioactivity studies assessed the natural and artificial radionuclides in soil samples around the world. However, the number of studies made on countries in the Mideast remains somewhat limited by comparison. In Jordan, several studies on soil radioactivity measurements in selected regions have been performed [5, 7-11]; among them, Ahmad et al., 1997 [7] have measured the concentration levels of indoor radon in a number of randomly selected houses and natural radioactivity in soil in different areas of Jordan using CR-39 based dosimeters. Al-Hamadneh et al., 2003 [8] studied surface and core soil samples from different regions of Jordan. They measured the concentration of artificial radionuclides (^{137}Cs). The estimation of the annual effective dose equivalent due to ^{137}Cs was more than 200 μSv . Al-Jundi, 2002 [9] has found that the concentration values of ^{40}K and ^{232}Th obtained from old phosphate mine of Russaifa city are normal compared to other worldwide standards in other countries, but the concentrations of ^{238}U are much higher than the worldwide range. Abusuni, et al., 2008 [10] studied the activity concentrations of ^{238}U , ^{232}Th and ^{40}K in soil cores of Araba Valley. The mean concentrations of these radioactive nuclei were below than in other populated areas and the mean activity concentrations were decreased with depth. More recently, Abu Haija, 2012 [11] studied the natural radionuclide activity concentration in soil of Tafila city. The activities of the collected samples were below the world average activity rates. Ababneh et al., 2012 [5] studied the vertical distribution of both natural and anthropogenic radionuclides in heavy rainfall areas (Ras Muneef region). They found that ^{137}Cs has two types of depth profile depending on land use; Gaussian distribution and exponential distribution.

The United Nations Scientific Committee on the Effects of Atomic Radiation (UNSCEAR) report [1] does not provide data concerning these radionuclides in Jordan. So, establishing a baseline for natural and artificial radioactivity is

becoming essential to develop future guidelines in the country and the region for radiological protection of the population. Further investigations on the level of these radionuclides in the area, as no such study has been carried out, along with previous existing studies will contribute to establishing such a baseline level.

The natural and artificial radionuclides may transport to the human body through the food chain; i.e., mainly through the soil. Thus, in this work, the area of high agricultural use in the northwestern corner of Jordan, "Bani-Kananah District", was selected to investigate its radioactive content, calculating radium equivalent and examining the internal and external hazard indices. The area was chosen to be undisturbed away from the street, cultivated, uniform and inclusive of all regions in the area.

Materials and Methods

Sampling Area and Sample Collection

The area of the study lies within Bani-Kananah District in the northwestern corner of Jordan which covers an area of about 250 km^2 (Fig. 1). The area of agricultural use in Bani-Kananah District is 200 km^2 which is 80% of the total area. The area was chosen for this study because of the amount of rainfall and the type of soil making it suitable for agricultural use. The major crops grown are olives and pomegranate.

A total of 38 surface soil samples were collected from different sections at 0-10 cm depth level all over; (i.e., one sample for every section). The longitude and latitude for every sample position were taken using GPS. The samples were collected from agricultural, uniform, undisturbed and cultivated regions in the described area, packed in plastic bags and assembled in the laboratory. Then, the samples were oven dried for at least 2 hr at 100°C until a constant weight is reached and sieved through 0.05 mm mesh to remove stones, pebbles and other impurities. Samples were then weighed and transferred to standard 100 ml cylindrical cups of 2 cm radius and 6 cm height. Thereafter, the samples were stored for at least 5 weeks before conducting gamma spectrometric analysis to ensure that secular equilibrium between ^{238}U and ^{232}Th and their respective daughters was reached.

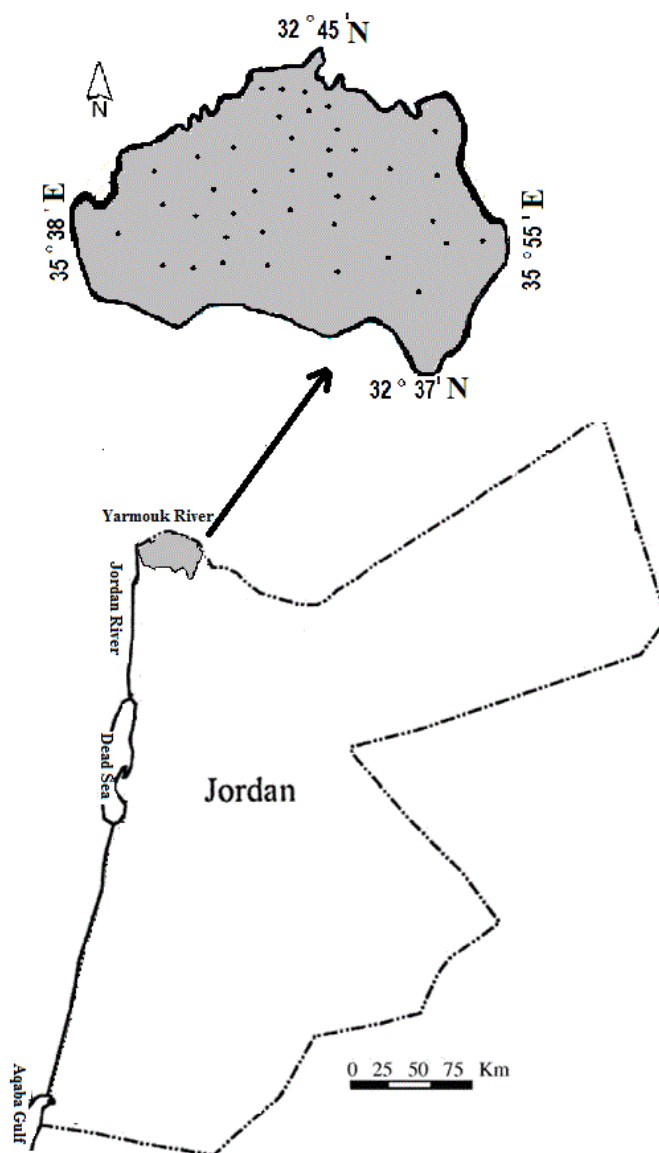


FIG. 1. Location map of the soil samples.

Activity Concentration Measurements

The radioactivity of the soil samples was measured using a low level counting system (gamma ray spectrometer) consisting of a high – purity germanium (HPGe) detector (GC2519) described elsewhere [12]. The detector has an active volume of 105.7 cm^3 , a relative efficiency of 25% at 1.33 MeV of ^{60}Co gamma ray peak and a resolution of 1.9 keV at the same energy peak (Canberra, USA). To reduce background radiation, the detector is shielded by a 10 cm thick lead cylinder. A reference standard source (MGS-5, Canberra, USA) was used for energy and efficiency calibration, which emits gamma rays of 60-1461 keV. The standard sample consists of the radionuclides: ^{152}Eu , ^{57}Co , ^{113}Sn , ^{137}Cs , ^{54}Mn , ^{65}Zn and ^{40}K (Table 1). The detector signal was taken to the PC supplied with an

MCA (Multi Channel Analyzer, model DSA-1000). Analysis of data was done using Genie 2000 software (Canberra, USA), containing peak search and nuclide identification modules. The prepared cups (samples) were placed on the detector end cap at a distance of 1 cm. Each sample was counted for 24 h to obtain good statistics with dead time smaller than 10% and quality control tests were performed using reference samples obtained from IAEA (IAEA-375 soil and IAEA-315 marine sediment) in the same geometry as the measured samples. Under identical conditions, empty cup measurements were also carried out to determine the background counts, which were later subtracted from the measured spectrum of each sample to get the net activities of the radionuclides. Fig. 2 shows the gamma ray spectrum for one of the soil samples.

TABLE 1. Data for radionuclides contained in standard sample used for energy and efficiency of calibration (MGS-5).

Nuclide	Energy (keV)	Activity (Bq)	Count rate (C/s)
¹⁵⁵ Eu	60.0	2330	26
	86.5		722
	105.3		503
⁵⁷ Co	122.1	5750	4920
	136.5		604
¹¹³ Sn	255.1	9600	202
	391.7		6230
¹³⁷ Cs	661.6	2220	1880
⁵⁴ Mn	834.8	7520	7520
⁶⁵ Zn	1115.5	10800	5490
⁴⁰ K	1460.8	798	85

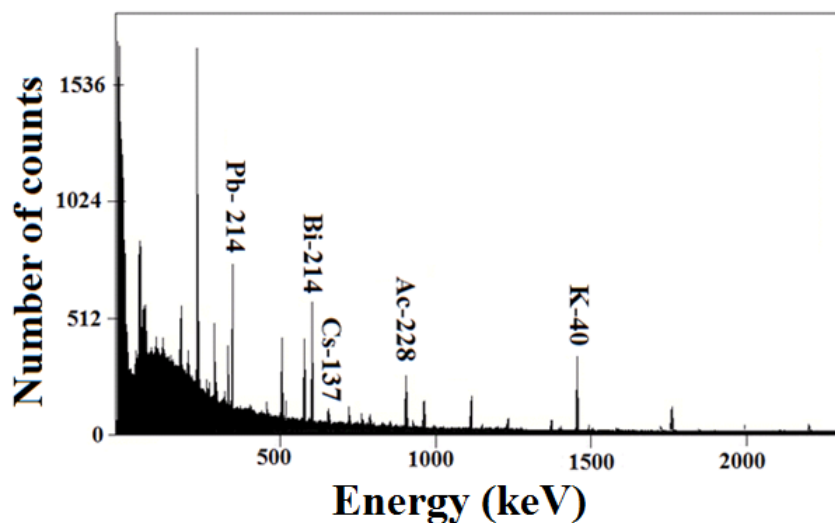


FIG. 2. The gamma ray spectrum for one of the soil samples (S 9).

The determination of ¹³⁷Cs and ⁴⁰K measured activity concentrations for the collected samples from Bani-Kananah District is based upon the detection of their gamma lines (gamma yields) of 662 keV (0.85) and 1461 (0.11) keV, respectively. For ²³²Th radionuclide, the activity was determined using gamma line of 911 keV (0.29) of its daughter ²²⁸Ac. The determination of ²³⁸U activity concentration was based on the detection of gamma rays emitted using weighted mean activity concentration of its first daughter ²³⁴Th of 63.3 keV (0.048).

The minimum detectable activities of (MDAs) for ¹³⁷Cs, ⁴⁰K, ²³⁸U and ²³²Th were 0.18, 8.4, 4.5 and 0.7 Bq/kg, respectively. The MDAs were calculated using the following equation:

$$MDA = \frac{2.71 + 4.65\sqrt{B}}{\varepsilon \times P_{\gamma} \times m} \quad (1)$$

where B is the true mean of the blank, P_{γ} is the gamma yield of the nuclide at given energy, ε is the efficiency of the detector at the peak and m is the mass of the sample.

Calculation of Radiation Hazard Indices

The radium equivalent activity index (Ra_{eq}) in Bq/kg represents the specific activity levels of materials containing different concentrations of ²²⁶Ra (²³⁸U), ²³²Th and ⁴⁰K, taking into account the hazards of radiation correlated with each component. It can be calculated according to the following equation [1]:

$$Ra_{eq} = C_{Ra} + 1.423 C_{Th} + 0.077 C_K \quad (2)$$

where C_{Ra} , C_{Th} and C_K are the activity concentrations of ²²⁶Ra (²³⁸U), ²³²Th and ⁴⁰K, respectively. The above equation is based on the estimate that 1 Bq/kg of ²²⁶Ra (²³⁸U), 0.7 Bq/kg

of ^{232}Th and 13 Bq/kg of ^{40}K produce the same gamma ray dose rate.

The total absorbed dose rate (D) at 1 m above the ground surface due to gamma radiation in air has been calculated by assuming uniform distribution of the natural radionuclides ^{226}Ra (^{238}U), ^{232}Th and ^{40}K using the following equation [1]:

$$D(\text{nGy/h}) = 0.429C_{\text{Ra}} + 0.662C_{\text{Th}} + 0.0427C_{\text{K}} \quad (3)$$

To estimate the annual effective dose rate (D_{eff}), the conversion coefficient from absorbed dose in air to effective dose is 0.7 Sv/Gy and an outdoor occupancy factor of (0.2) is used. The annual effective doses are calculated from the following equation [1]:

$$D_{\text{eff}} (\mu\text{Sv/y}) = D(\text{nGy/h}) \times 8760(\text{h/y}) \times 0.2 \times 0.7(\text{Sv/Gy}) \times 10^{-3} \quad (4)$$

The external and internal hazard indices (H_{ex} and H_{in}), respectively, are widely used and defined as follows [1]:

$$H_{\text{ex}} = C_{\text{Ra}}/370 + C_{\text{Th}}/259 + C_{\text{K}}/4810 \quad (5)$$

$$H_{\text{in}} = C_{\text{Ra}}/185 + C_{\text{Th}}/259 + C_{\text{K}}/4810 \quad (6)$$

The values of these indices must be less than unity for the radiation hazard to be negligible.

Results and Discussion

The activity concentrations of the radionuclides ^{137}Cs , ^{40}K , ^{232}Th and ^{238}U detected in soil samples were reported in Table 2 which shows low level activity concentrations. All concentrations were reported as Bq/kg dry weight. Based on Table 2, the activity concentration values ranged from 5.7 to 32.1 with an average ($\pm\text{SD}$) of 22.7 ± 15.2 for ^{232}Th , 12.2 to 34.6 with an average ($\pm\text{SD}$) of 20.4 ± 9.8 for ^{238}U , 62.0 to 240.2 with an average ($\pm\text{SD}$) of 160 ± 76 for ^{40}K and 1.5 to 12.4 with an average ($\pm\text{SD}$) of 4.6 ± 5.0 for ^{137}Cs .

The world-wide average concentration values of the natural radionuclides ^{238}U , ^{232}Th and ^{40}K are 40, 40 and 370 Bq/kg, respectively [1]. Our data in general agree well and are lower than international reported limits. The artificial source ^{137}Cs in the samples can be considered as being due to nuclear weapons, bomb tests and accidents. The ^{137}Cs concentration is attributed to global fallout.

The correlation between ^{232}Th and ^{40}K shown in Fig. 3 is linear, which is in agreement with other studies [5,9], while there is no theoretical basis for this calculation.

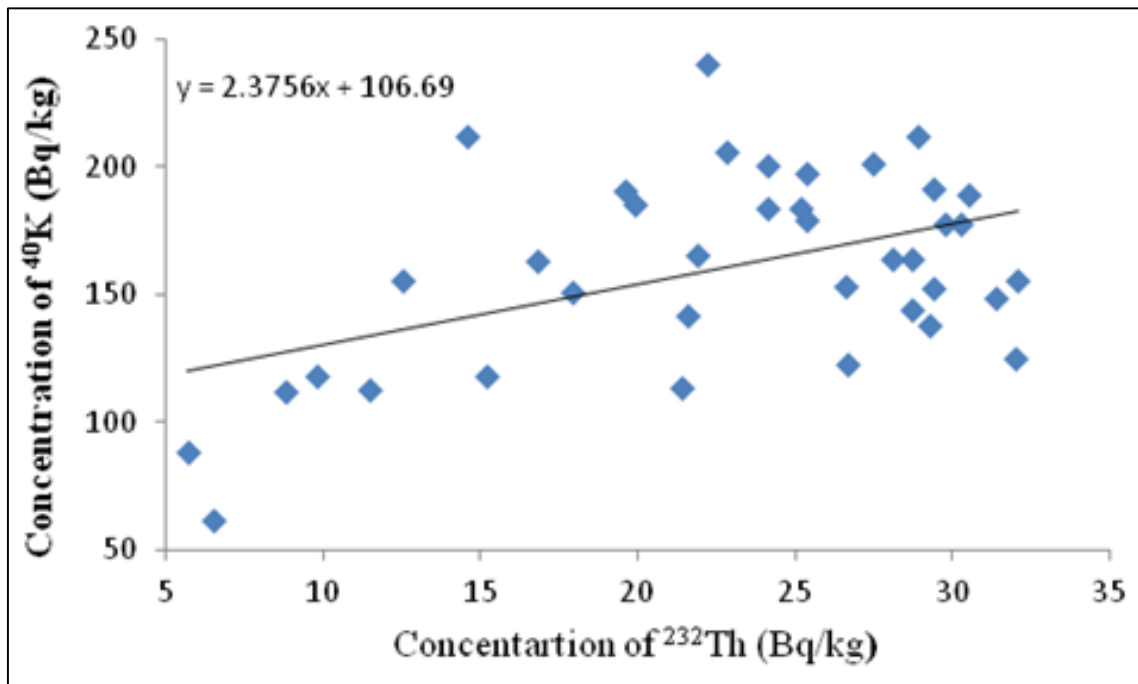


FIG. 3. Plot of the correlation between the activity concentrations of ^{232}Th and ^{40}K for all samples.

TABLE 2. Locations and activity concentrations of ^{238}U , ^{232}Th , ^{40}K and ^{137}Cs in Bq/kg in the studied soil samples.

	Position	Height above sea level (m)	^{137}CS	^{40}K	^{232}Th	^{238}U
S1	(32 ° 44' 02" N, 35° 46' 32" E)	360	5.0±0.4	200.8±16.0	24.1±2.3	17.0±2.8
S2	(32 ° 43' 43" N, 35° 47' 52" E)	368	2.2±0.3	153.1±13.6	26.6±2.7	20.6±3.0
S3	(32 ° 43' 38" N, 35° 48' 42" E)	367	4.1±0.3	185.7±15.2	19.9±2.2	29.7±4.2
S4	(32 ° 43' 39" N, 35° 49' 11" E)	344	11.3±0.7	118.2±12.2	15.2±2.0	34.6±2.2
S5	(32 ° 42' 53" N, 35° 49' 52" E)	395	1.5±0.4	184.1±15.0	24.1±1.9	14.2±2.9
S6	(32 ° 42' 37" N, 35° 52' 21" E)	410	2.1±0.2	184.2±15.0	25.2±2.4	21.1±3.1
S7	(32 ° 40' 45" N, 35° 52' 35" E)	438	2.6±0.4	211.9±16.5	28.9±2.4	20.3±3.0
S8	(32 ° 38' 59" N, 35° 51' 11" E)	502	5.4±0.4	240.2±18.0	22.2±2.2	25.2±3.6
S9	(32 ° 38' 57" N, 35° 53' 10" E)	475	2.5±0.4	177.7±14.7	29.8±2.4	18.7±2.8
S10	(32 ° 37' 13" N, 35° 53' 05" E)	515	2.8±0.3	189.3±15.3	30.5±2.5	27.0±3.6
S11	(32 ° 37' 31" N, 35° 52' 41" E)	493	6.5±0.5	212.3±16.6	14.6±2.1	18.7±3.0
S12	(32 ° 37' 37" N, 35° 51' 26" E)	497	4.9±0.5	179.6±15.0	25.4±2.3	27.5±3.9
S13	(32 ° 38' 07" N, 35° 51' 50" E)	520	4.1±0.4	206.0±16.1	22.8±2.3	19.8±2.8
S14	(32 ° 40' 29" N, 35° 51' 27" E)	482	6.3±0.6	151.1±13.3	17.9±2.0	22.7±3.3
S15	(32 ° 42' 26" N, 35° 49' 48" E)	304	4.9±0.5	112.7±11.8	11.5±1.9	15.6±2.7
S16	(32 ° 41' 30" N, 35° 49' 37" E)	423	2.5±0.3	148.9±13.9	31.4±2.5	16.5±2.7
S17	(32 ° 38' 27" N, 35° 50' 03" E)	569	3.5±0.4	201.8±16.0	27.5±2.4	25.3±3.6
S18	(32 ° 39' 37" N, 35° 48' 54" E)	483	4.5±0.3	155.6±13.7	12.5±1.9	20.7±3.1
S19	(32 ° 40' 10" N, 35° 49' 22" E)	516	4.5±0.3	137.8±13.0	29.3±2.4	17.9±2.8
S20	(32 ° 39' 21" N, 35° 47' 24" E)	493	2.2±0.4	164.1±14.2	28.7±2.4	22.5±3.2
S21	(32 ° 39' 59" N, 35° 46' 41" E)	458	7.6±0.5	141.5±13.1	21.6±2.2	21.5±3.1
S22	(32 ° 41' 06" N, 35° 50' 10" E)	440	8.0±0.6	113.4±12.0	21.4±2.2	16.0±2.6
S23	(32 ° 43' 15" N, 35° 48' 11" E)	201	6.9±0.5	112.0±11.8	8.8±1.9	12.8±2.1
S24	(32 ° 42' 41" N, 35° 44' 10" E)	355	2.9±0.4	164.0±14.2	28.1±5.5	16.7±3.8
S25	(32 ° 42' 14" N, 35° 45' 16" E)	393	2.5±0.4	191.9±15.4	29.4±2.5	15.9±2.5
S26	(32 ° 41' 12" N, 35° 46' 56" E)	442	4.4±0.5	125.1±12.6	32.0±2.5	22.7±3.3
S27	(32 ° 41' 21" N, 35° 46' 13" E)	415	5.8±0.5	144.5±13.2	28.7±2.5	20.3±2.9
S28	(32 ° 40' 47" N, 35° 46' 47" E)	450	4.9±0.4	156.0±13.8	32.1±2.6	18.8±2.9
S29	(32 ° 40' 08" N, 35° 48' 38" E)	481	5.7±0.5	163.6±14.1	16.8±1.7	18.9±2.8
S30	(32 ° 39' 38" N, 35° 45' 20" E)	468	5.9±0.4	62.0±10.0	6.5±1.7	14.8±2.4
S31	(32 ° 39' 04" N, 35° 44' 23" E)	421	12.4±0.7	165.6±14.3	21.9±2.2	22.6±3.2
S32	(32 ° 38' 59" N, 35° 39' 40" E)	328	1.8±0.4	197.3±15.8	25.4±2.4	12.3±2.2
S33	(32 ° 38' 08" N, 35° 38' 28" E)	199	2.5±0.4	191.0±15.5	19.6±2.2	12.2±2.1
S34	(32 ° 39' 20" N, 35° 50' 23" E)	537	3.4±0.5	177.5±14.7	30.3±2.5	24.8±3.5
S35	(32 ° 41' 20" N, 35° 48' 16" E)	218	1.7±0.4	152.5±13.7	29.4±2.4	23.5±3.5
S36	(32 ° 39' 27" N, 35° 41' 01" E)	180	2.1±0.4	118.2±12.1	9.8±1.9	19.8±3.0
S37	(32 ° 40' 35" N, 35° 39' 59" E)	-50	4.9±0.5	88.5±11.2	5.7±1.9	21.9±3.2
S38	(32 ° 40' 23" N, 35° 44' 53" E)	425	6.4±0.5	123.0±12.3	26.7±2.3	23.7±3.4
	MIN.		1.5	62.0	5.7	12.2
	MAX.		12.4	240.2	32.1	34.6
	AVERAGE		4.6	160	22.7	20.4
	SD		2.5	38	7.6	4.9

From Table 3, the radium equivalent activity index (R_{eq}) in the soil samples ranges from 28.77 to 84.93 Bq/kg with a mean value of 65.0 ± 27.8 Bq/kg, which is less than the safe limit (370 Bq/kg) recommended by the Organization for Economic Cooperation and Development (OECD) (1979) [13]. The total absorbed dose

(D) in the study area ranged between 13.21 and 39.65 nGy/h with an average value of 30.5 ± 13.1 nGy/h, which is lower than the range of values given in UNSCEAR (2000) {57(24-160) nGy/h}.

TABLE 3. External hazard indices (H_{ex}), internal hazard indices (H_{in}), radium equivalent (R_a), total absorbed dose (D) and annual effective dose (AEDE) in the studied soil samples.

Sample	H_{ex}	H_{in}	R_{eq} (Bq/kg)	D (nGy/h)	D_{eff} (μ Sv/y)
S1	0.18	0.23	66.76	31.65	38.84
S2	0.19	0.25	70.19	32.81	40.27
S3	0.20	0.28	72.27	33.64	41.28
S4	0.18	0.27	65.37	29.82	36.59
S5	0.17	0.21	62.64	29.73	36.49
S6	0.19	0.25	71.14	33.43	41.02
S7	0.21	0.27	77.69	36.68	45.01
S8	0.20	0.27	75.24	35.52	43.60
S9	0.20	0.25	74.74	35.15	43.14
S10	0.23	0.30	84.93	39.65	48.66
S11	0.15	0.20	55.82	26.57	32.60
S12	0.21	0.28	77.47	36.10	44.30
S13	0.18	0.24	68.06	32.18	39.49
S14	0.16	0.22	59.76	27.87	34.20
S15	0.11	0.15	40.59	18.99	23.30
S16	0.20	0.24	72.65	34.09	41.83
S17	0.22	0.28	79.92	37.46	45.98
S18	0.14	0.19	50.42	23.63	29.00
S19	0.19	0.24	70.15	32.81	40.26
S20	0.21	0.27	75.93	35.48	43.54
S21	0.17	0.23	63.08	29.40	36.08
S22	0.15	0.19	55.18	25.76	31.62
S23	0.09	0.13	33.90	15.97	19.60
S24	0.19	0.23	69.31	32.62	40.03
S25	0.20	0.24	72.46	34.29	42.08
S26	0.21	0.27	77.82	36.11	44.32
S27	0.20	0.25	72.27	33.74	41.40
S28	0.21	0.26	76.44	35.81	43.95
S29	0.15	0.20	55.35	26.04	31.95
S30	0.08	0.12	28.77	13.21	16.21
S31	0.18	0.24	66.46	31.08	38.14
S32	0.17	0.21	63.59	30.33	37.22
S33	0.15	0.18	54.75	26.19	32.14
S34	0.22	0.29	81.53	38.08	46.74
S35	0.21	0.27	77.08	35.90	44.06
S36	0.12	0.17	42.80	19.89	24.40
S37	0.10	0.16	36.83	16.84	20.67
S38	0.19	0.26	71.12	32.94	40.43
MIN.	0.08	0.12	28.77	13.21	16.21
MAX.	0.23	0.30	84.93	39.65	48.66
AVERAGE	0.18	0.23	65.0	30.5	37.4
SD	0.04	0.04	13.9	6.53	8.01

The annual effective dose in this study area ranged from 16.21 to 48.66 μ Sv/y with an average value of 37.4 ± 16.0 μ Sv/y. It's clear that the average value of the annual effective dose (0.037 mSv/y) is lower than the worldwide average value for outdoor effective dose of 0.07 mSv/y, reported by UNSCEAR (2000) [1].

The calculated values of H_{ex} for the soil samples studied ranged from 0.08 to 0.23 with an average value of 0.18 ± 0.08 . In addition, the calculated values of H_{in} ranged from 0.12 to 0.30 with an average value of 0.23 ± 0.08 . Since these values are lower than unity, the soil in the study area is safe and can be used for agriculture

without posing any radiological threat to the population.

The activity concentrations and dose rates of natural radionuclides of soil samples in different regions around the world are shown in Table 4.

TABLE 4. Summary of activity concentrations and dose rates of natural radioisotopes in soil samples in some of the world regions.

Region / Country	^{238}U	^{232}Th	^{40}K	Dose rate (nGy/h)	Reference
Karak, Jordan	228.9	27.2	410.2	-	[7]
Amman, Jordan	56.4	28.8	501.3	-	[7]
Russifa, Jordan	48.3-523.2	8.7-27.1	44-344	97.50	[9]
Northern Jordan	49.9	26.7	291.1	51.5	[14]
Tafila, Jordan	22.03	27.91	285.02	40.12	[11]
Ras Muneef, Jordan	10-73.2	5.8-30.8	108.8-325.6	44.2	[5]
Zarqa, Jordan	41.3	Low	390.8	34.66	[15]
Syria	19	24	336	-	[16]
Istanbul, Turkey	21	37	342	65	[17]
Pakistan	37	18	320	22	[18]
Bushehr, Iran	12-75	8-33	108-520	30.56	[19]
Cyprus	25	20	360	56	[20]
Greece	49	51	840	84	[20]
Spain	42	17	285	30	[19]
Russia	-	33	470	76	[20]
United States	35	35	370	47	[20]
Worldwide Average	40	40	370	57	[20]
Present study	20.4	22.7	160.6	30.46	

Conclusions

The activity concentrations of ^{137}Cs , ^{40}K , ^{238}U and ^{232}Th in soil samples collected from north west Jordan (Bani-Kananah) have clearly shown the existence of low level activity. The calculated average radium equivalent activity index (Ra_{eq}), the mean external (H_{ex}) and internal

hazard indices (H_{in}), the total absorbed dose rate and the annual effective dose in this study show that the radioactivity of radionuclides found in the surveyed area is below the world activity values. It is nominal and does not pose any potential health hazard to the general public.

References

- [1] United Nations Scientific Committee on the Effects of Atomic Radiation (UNSCEAR), Sources and Effects of Ionizing Radiation. Report to General Assembly, (United Nations, New York, 2000).
- [2] Obed, R.I., Farai, I.P. and Jibiril, N.N., J. Radiol. Prot., 25 (2005) 305.
- [3] Avwiri, G.O., Agbalagba, O.E. and Enyinna, P.I., J. Appl. Sci., 7 (2007) 543.
- [4] Akhtar, N., Tufail, M., Ashraf, M., Mohsen, A. and Iqbal, M., Radiat. Meas., 39 (2005) 11.
- [5] Ababneh, A.M., Almomani, A.M., Alyassin, A.M. and Ababneh, Z.Q., Radiat. Prot. Dosim., 150 (2012) 82.
- [6] Almgren, S. and Isaksson, M., J. Environ. Radioact., 91 (2006) 90.
- [7] Ahmad, N., Matiullah, A. and Khatibeh, A.H., Radiat. Prot. Dosim., 71 (1997) 231.
- [8] Al Hamarneh, I., Wreikat, A. and Toukan, K., J. Environ. Radioact., 67 (2003) 53.
- [9] Al-Jundi, J., Radiat. Meas., 35 (2002) 23.
- [10] Abusuni, M., Al-Ayasreh, K. and Al-Jundi, J., Radiat. Prot. Dosim., 128 (2008) 213.
- [11] Abu-Haija, O., Modern. Appl. Sci., 6 (2012) 87.
- [12] Ababneh, A.M., Masa'deh, M.S., Ababneh, Z.Q., Awawdeh, M.A. and Alyassin, A.M., Radiat. Prot. Dosim., 134 (2009) 30.

- [13] Organization for Economic Corporation and Development (OECD), 1979.
- [14] Al-Hamarneh, I.F. and Awadallah, M.I., Radiat. Meas., 44 (2009) 102.
- [15] Afaneh, F., Al-Momani, M., Al-Jundi, J., Aldrabee, A. and Juwhari, H., Inter. J. Low Radiat., 10 (2016) 234.
- [16] Al-Masri, M.S., J. Environ. Radioact., 86 (2006) 187.
- [17] Karahan, G. and Bayulken, A., J. Environ. Radio., 47 (2000) 213.
- [18] Mostajaboddavati, M., Hasanzadeh, A., Faghihian, H., Abdi, M.R. and Kamali, M., J. Radio. Nucl. Chem., 268 (2006) 539.
- [19] Abdi, M.R., Faghihian, H., Mostajaboddavati, M., Hasanzadeh, A. and Kamali, M., J. Radio. Nucl. Chem., 270 (2006) 319.
- [20] United Nations Scientific Committee on the Effects of Atomic Radiation (UNSCEAR), Sources and Effects of Ionizing Radiation. Report to General Assembly, (United Nations, New York, 1988).

Semi-Quantitative Analysis for Pottery Fragments Excavated at Udhruh Site, Jordan Using Non-destructive SR-XRF Analysis Employing Multivariate Statistical Methods

K. AbuSaleem^{a,b}, A. Aldrabee^a, A. Wriekat^a, M. Tarawneh^c and F. Abudanah^c

^a Jordan Atomic Energy Commission (JAEC), Shafa Bdran 11934, Amman, Jordan.

^b Department of Physics, The University of Jordan, Amman 11942, Jordan.

^c Al-Hussein Bin Talal University, Department of Archaeology, P.O. Box 285, Wadi Musa - Petra, Jordan.

Received on: 1/2/2017;

Accepted on: 12/4/2017

Abstract: This paper presents a multielement analysis of fifteen Ayyubid-Mamluk glazed pottery sherds for determining the chemical composition in order to study their provenance. The tested fragments in this work belong to the historical site of Udhruh in southern Jordan. The chemical analysis for samples has been carried out by using Synchrotron Radiation X-ray Fluorescence Spectrometry (SR-XRF) technique. The semi-quantitative analysis of the elements Fe, Cu, Zn, Br, Rb, Sr, Y, Zr, Nb, Mo, Pd, Ag, Cd and Pb has been applied to the samples using SR-XRF technique. The data were analyzed by using Principal Component Analysis (PCA) and Hierarchical Cluster Analysis (HCA) in order to define groups of different glazed pottery sherds by obtaining information about their similarity and clustering. The results provide persuasive evidence that the Udhruh pottery fragments have at least three different sources of provenance.

Keywords: SR-XRF, Semi-quantitative, Udhruh, Ayyubid-Mamluk pottery, PCA.

Introduction

The application of interdisciplinary analytical methods to archaeology is well established to date. The employment of various chemical, geological and physical analytical techniques in order to study archaeological artefacts (e.g. ceramics, mortars, slags, marbles ... etc.) is also a common practice nowadays. The chemical, mineralogical and structural characterization of ancient pottery can shed light on the provenance of raw materials used for ceramic production and determine the technological processes related to pottery manufacture. During the last years, several studies have been carried out concerning the analysis of archaeological ceramics employing various techniques. Most studies deal with the determination of chemical composition. The identification of specific chemical elements

in high concentration could be related to the geological profile of the region of study and thus one can distinguish between local potteries and imported ones [1, 2]. Therefore, one of the most important questions asked by archaeologists can be answered. The question is related to the provenance of the excavated objects, since any ancient item could have been produced locally at the place where it was found or transported to the site from a location where it was originally manufactured [3].

Analysis of cultural objects by X-Ray Fluorescence (XRF) spectroscopy is the most widely used technique due to a number of favorable analytical characteristics. It is a multi-element, non-destructive and high sensitivity technique. In addition, it is applicable to a wide

range of samples (solids, liquids and gases). These features have made the XRF a very popular analytical technique in several archaeometric studies [4,5]. Regarding the possibility of getting quantitative analysis in archaeometric applications, when using the energy dispersive detector for X-ray spectroscopy, the problems arising from the limited detector sensitivity to detect low Z elements and the irregular shape or the non-homogeneous composition of the sample have generated a widespread opinion that only semi-quantitative analyses are possible in XRF applications to archaeometry such as glass and ceramic samples. The problem of quantitative XRF analysis does not arise normally from the irregular shape of the tested object, but because of the impossibility of evaluating the auto absorption correction due to matrix low Z (<11) elements which in most cases cannot be detected by standard solid-state detectors [6, 7].

Semi-quantitative analytical procedures [8] are becoming more and more popular among researchers and using such procedures makes the question of the accuracy of results more profound. The accuracy of any analytical procedure depends to a great extent on the spectral resolution, counting statistics, matrix correction and analytical procedure, which are especially optimized to provide fast analysis of alloy composition [9]. The energy and intensity results of the XRF spectra are not only in accordance with a given element, but also with its abundance in the tested sample(s) [10].

According to the analyzing capability, the Synchrotron Radiation X-ray Fluorescence Spectrometry (SR-XRF) has gained an increasing interest in the field of elemental analysis. Several works showing the advent of technique based on XRF can be found in literature during the past decade [11, 12].

In the present study, two multivariate statistical methods, Principal Component Analysis (PCA) and Hierarchical Cluster Analysis (HCA) have been applied to ancient Ayyubid-Mamluk glazed pottery from Udhruh historical site in southern Jordan. Similar technique, experimental conditions and statistical methods were provided for Karak Castle site [13]. The main goal was to determine similarities and correlation between the selected samples based on their elemental composition. The extracted information will help to know more

about the provenance sources of Ayyubid-Mamluk ceramic in Udhruh historical site. The samples were kindly borrowed from the Department of Archaeology at Al-Hussein bin Talal University.

Site, Samples and Methodology

Udhruh Historical Site

Udhruh is located at the eastern foot of the Al-Shara mountain series to the east of the well-known historical site of Petra, (30° 19' 40" N, 35° 35' 55" E), as shown in Fig. 1. The site draws its importance from its strategic location on the crossroads of the ancient trade routes in addition to the fact that water was always available to the site from its domestic, perennial springs. Udhruh is referred to, in historical literature and sources, as early as the second century A.D. Ptolemy, in the second century A.D, mentioned Udhruh only as a town in Arabia Petraea [14-18]. The site appears more often in Byzantine and Early Islamic sources and documents, where, for example, the Byzantine tax document known as the Beersheba Edict lists Udhruh among the towns of PalestinaTertia as does Stephan of Byzantium. Udhruh is also thought to be the Augustopolis mentioned by George of Cyprus and Hierocles [14], [19- 21]. This belief also is supported by data, which have been recently revealed from the Petra Papyri [22]. Two bishops from Augustopolis have been mentioned attending two church councils in the region during the 5th and 6th centuries AD [23, 24]. Udhruh was also often mentioned in early Islamic sources, as the town's inhabitants agreed to pay the poll tax to Prophet Muhammad in A.D. 630 [14, 25].

The major archaeological remain at Udhruh is the Roman fortress, but there are other significant monuments referred to other times. Outside the curtain wall of the fortress and about 20 m south of the south-western corner tower, a Byzantine church was built to serve a community who lived within the fortress at the time. An Ottoman fort was constructed, against the northern side of the curtain wall of the Roman fortress, since the site might have been a station on the pilgrimage route [26].


Samples under Investigation



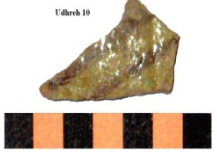




Fifteen pottery samples have been investigated and reported in this work. The macroscopic description of these samples is

presented in Table 1. The name of the sample, the hypothesized types, the characterizations of the ceramic, core fabric and color are given in the table. The sherds have been found in the Udhruh archaeological site (Fig. 1). These ceramic samples were found during an

archaeological excavation campaign in 2008 and 2009 by the Department of Archaeology at Al-Hussein bin Talal University in cooperation with the Department of Antiquities, Ministry of Tourism and Antiquities, Jordan.

TABLE 1. The description of ceramic pottery samples (Udhruh site).

Sample Name (Object)	Object Type	(Characterizations of the ceramic object) - Glaze color*, interior/ exterior. - Core fabric types and color*	Photo (camera)
Udhruh 1	Plain-body	- Glazed bowl (wheelthrown). - Lead glazed color = (5G 5/4) / undecorated. - Medium- hard, friable, dense fabric. Fire pink (5YR 8/6).	 Udhruh 1
Udhruh 2	Body	- Glazed bowl (wheelthrown). - Lead glazed color = (7.5G 6/6), (10GY 4/3) / (2.5GY 4/4). - Medium-hard, dense fabric with regular voids (10Y 8/2).	 Udhruh 2
Udhruh 3	Body	- Glazed bowl (wheelthrown). - Lead glazed color = (2.5GY 8/10). - Comments: Thin mottled glaze with regular intrusions and speckling. - Medium-hard, friable, dense fabric with regular voids (2.5YR 7/8).	 Udhruh 3
Udhruh 4	Plain-body	- Glazed bowl (wheelthrown). - Lead glazed color = (2.5G 8/12) / undecorated. - Medium-hard, friable, dense fabric with regular voids (5YR 7/6).	 Udhruh 4
Udhruh 5	Plain-body	- Glazed bowl (wheelthrown). - Lead glazed color = (5Y 4/6). - Hard, dense fabric with small voids (5YR 7/6).	 Udhruh 5
Udhruh 6	Plain-body (thin)	- Glazed bowl (wheelthrown). - Lead glazed color = (7.5Y 5/6). - Medium, dense fabric with regular voids (10Y 8/6).	 Udhruh 6
Udhruh 7	Plain-body	- Glazed bowl (wheelthrown). - Lead glazed color = (5 GY 4/4). - Medium, friable, dense fabric (2.5YR 7/8).	 Udhruh 7

Sample Name (Object)	Object Type	(Characterizations of the ceramic object)		Photo (camera)
		- Glaze color*, interior/ exterior.	- Core fabric types and color*	
Udhruh 8	Plain-body	- Glazed bowl (wheelthrown). - Lead glazed color = (7.5 YR 5/6). - Medium, dense fabric with regular voids (10YR 8/6).		
Udhruh 9	Plain-body	- Glazed bowl (wheelthrown). - Lead glazed color = (2.5Y 8/10), (5YR 2/4) decorated lines/ undecorated. - Hard, dense fabric (2.5YR 3/4).		
Udhruh 10	Plain-body	- Glazed bowl (wheelthrown). - Lead glazed color = (2.5Y 6/6), (2.5YR 2/4) decorated lines. - Medium-hard, friable, dense fabric with regular voids (2.5YR 6/8).		
Udhruh 11	Plain-body	- Glazed bowl (wheelthrown). - Lead glazed color = (5YR 2/6), (2.5YR 5/8) / undecorated. - Medium, friable, dense fabric with regular voids (5YR 3/4).		
Udhruh 12	Plain-body	- Glazed bowl (wheelthrown). - Lead glazed color = (5G 4/6). - Medium, dense fabric with regular small voids. Fire pink-orange (2.5YR 7/10).		
Udhruh 13	Body	- Blue under turquoise bowl (wheelthrown). - Alkaline glazed color = (7.5 BG 7/6). - Medium, dense, friable fabric. Fire pale pink (10YR 9/3).		
Udhruh 14	Rim	-Black under turquoise bowl (wheelthrown). - Alkaline glazed color = (10Y 9/2), (10YR 1/2). - Medium, dense, friable fabric (7.5 Y 8/4).		
Udhruh 15		- Blue under turquoise bowl (wheelthrown). - Alkaline glazed color = (10 BG 6/8), (2.5 B 3/4). - Medium- hard, dense, friable fabric (7.5 Y 8/4).		

*Colors according to Munsell Book of Colour [26, 27].



FIG. 1. Map of Jordan showing Udhruh site.

Measurements and Analysis

To perform the analysis of the samples using SR-XRF, the inner part (core) of the samples was exposed to synchrotron X-ray beam. All measurements were carried out in BAM Line at BESSY II Synchrotron light source in Berlin-Germany using 40 keV incident energy X-ray beam, focused to a (0.8×0.8) mm² spot size. For each tested sample, the data have been acquired using a Si (Li) detector from two selected points on the core to be representative of the sample. The measurement time was 60 seconds for each sample. All measurements have been performed at room temperature. The spectra were processed by the AXIL-PC computer software program [29] based on IAEA standard program package QXAS. In order to be able to perform a semi-quantitative analysis, the elemental composition of the samples has to be identified. This task could be achieved by calculating the net peak area of the XRF spectrum for which the used software is capable. The importance of the semi-quantitative estimation stems from the fact that it can be useful for determining the elemental concentrations because the latter are proportional to the weight concentrations that can be measured using in the technique. Therefore, comparisons between the content of one chemical element in different samples with similar composition can be directly made through the energy and the area under the

measured peaks. The intensity of emission from each element can lead to classify the elements. The net area under the peak (counts) for certain element in an XRF spectrum is used to calculate the abundance of the element in the sample, since the peak intensities are proportional to the concentrations of the elements present in the sample.

Statistical Methods

In the archaeological field, cluster analysis together with Principal Component Analysis (PCA) represent the most commonly used methods to classify items in subgroups such that individuals within a group are similar to each other. PCA is a mathematical technique that allows n-dimensional identification of sample groups and hence is a very powerful method of exploratory multivariate statistical analysis. Therefore, it is often used in the interpretation of XRF artifact characterization for helping archaeologists to identify discrete compositional groups within a data set. This information may then be applied to formulate and test hypotheses on trade and exchange routes and socio-economic relations. Hierarchical Cluster Analysis is a multivariate method, which allows providing evidence for groups of objects within the data set. The results are commonly presented as dendrograms showing the order and levels of clustering as well as the distances between individual samples [30, 31, 32].

In this work, the Bray-Curtis coefficient [33] was used to calculate similarity matrices for analysis. The Bray-Curtis coefficient is widely used in the study of provenance of cultural heritage artefacts. The dendrograms have been constructed using a group-average linkage hierarchical cluster analysis [34] and the data have been processed by a PC computer software package Unscrambler X Ver.10.1 (Camo ASA software, Oslo, Norway).

Results and Discussion

The SR-XRF results of Udhruh site samples are shown in Table 2. In the table, the net peak area data (in counts) for selected elements: Fe, Cu, Zn, Br, Rb, Sr, Y, Zr, Nb, Mo, Pd, Ag, Cd and Pb of the XRF spectra are given. In order to perform a semi-quantitative analysis, 210 data entries (15 samples \times 14 elements), the PC computer software package Unscrambler X Ver.10.1 (Camo ASA software, Oslo, Norway) has been employed. The multivariate statistical

analysis has been carried out to verify the similarity of the samples.

PCA and Hierarchical Cluster Analysis are routinely applied to the data with the purpose of identifying groups of chemically similar sherds, which can be interpreted as representing sherds made from the same raw materials or mixtures of raw materials and therefore presumably made in the same place, although not necessarily at the same time. Fig. 2 and Fig. 4 show the Principal Component Analysis (PCA) and Cluster Analysis (CA) for the data presented in Table 2.

The analyzed data have been applied to the raw data matrix of dimensions 15×14 (samples \times chemical parameters). Fig. 2 represents the scatter score plot of the readings PC1 versus PC2 data and the loading plot is reported in Fig. 3. The corresponding score plot shows that the data are confined in two large groups except sample UDR15, which does not follow either of the other large groups. It should be mentioned that each group contains the samples belonging to the same pottery provenance source.

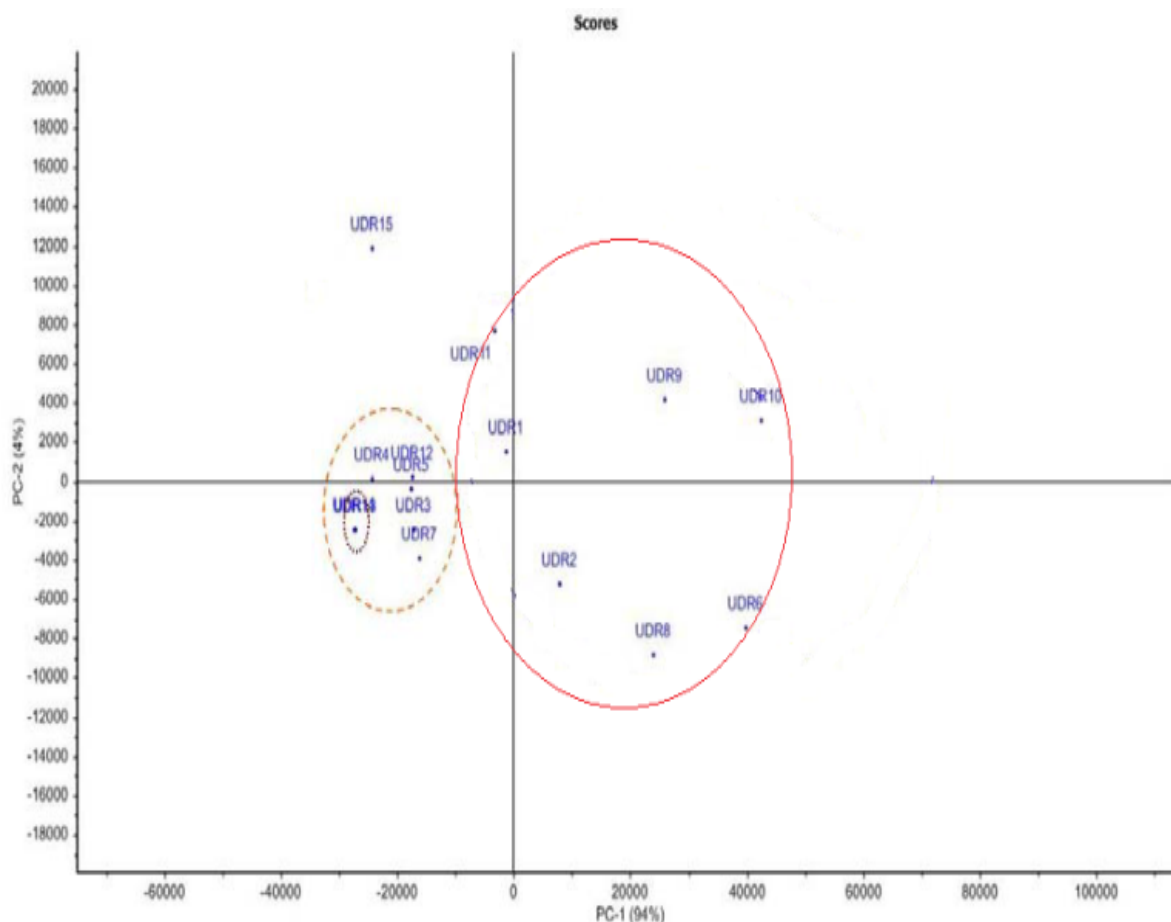


FIG. 2. Score plot of PCA of the normalized area under the peaks of SR-XRF result for Udhruh site samples. PC1 vs. PC2 data matrix of dimensions 15×14 (15= number of samples; 14= number of elements).

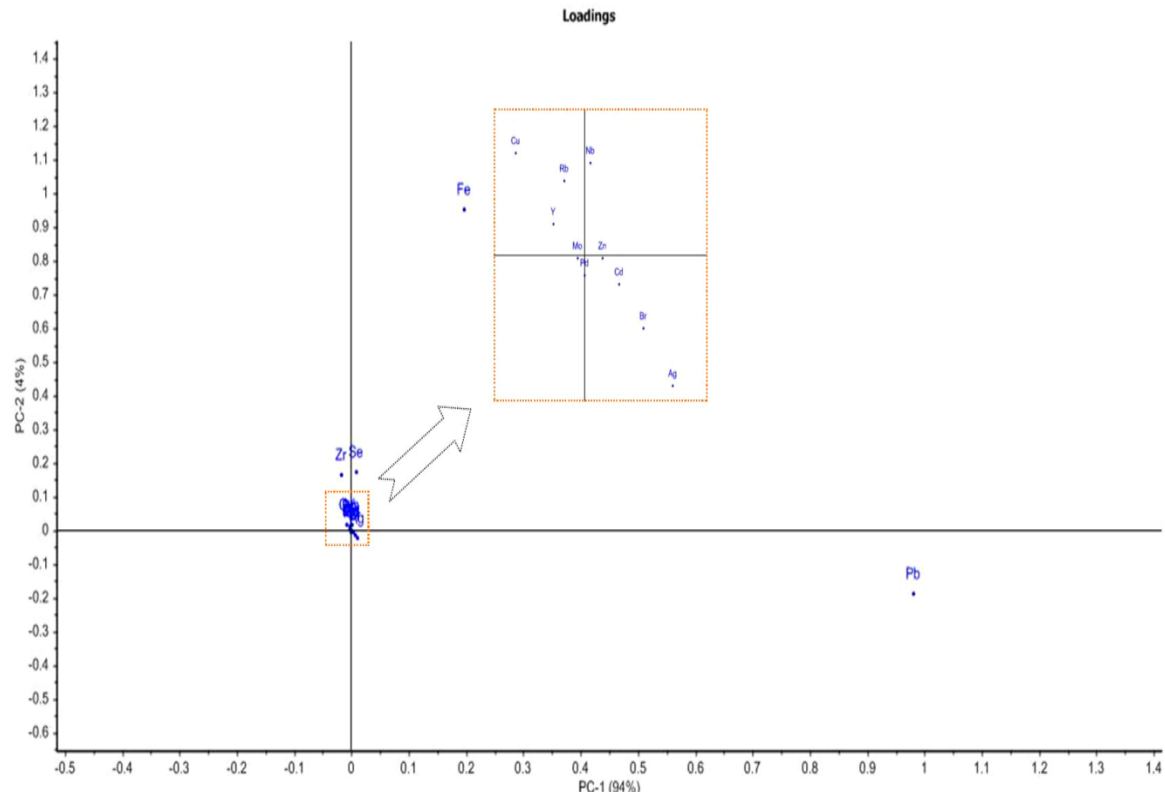


FIG. 3. Loading plot of PCA of the normalized area under the peaks of SR-XRF result for Udhruh site samples. PC1 vs. PC2 data matrix of dimensions 15x14 (15= number of samples; 14= number of elements).

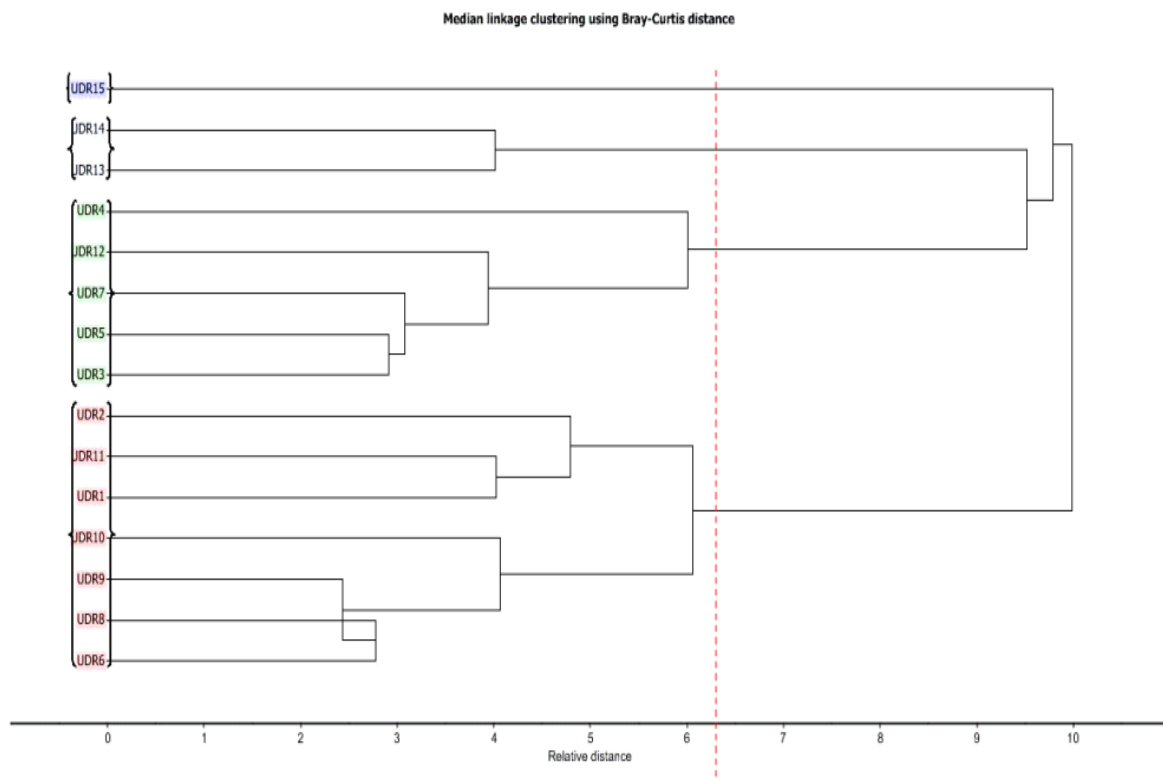


FIG. 4. Hierarchical clustering dendrograms by median linking and Bary-Curtis distance for the 15 ceramic sherd samples from Udhruh site (normalized area under the peaks of SR-XRF result).

TABLE 2. Net peak area (in counts) for selected elements of SR-XRF result for Udhruh site samples.

	²⁶ Fe	²⁸ Cu	³⁰ Zn	³⁵ Br	³⁷ Rb	³⁸ Sr	³⁹ Y	⁴⁰ Zr	⁴¹ Nb	⁴² Mo	⁴⁶ Pd	⁴⁸ Cd	⁴⁷ Ag	⁸² Pb
UDR 1	7660.36	1107.77	210.07	195.76	BDL	5968.74	BDL	12064.11	910.65	260.59	BDL	412.97	BDL	25242.55
UDR 2	5063.89	2046.31	567.19	202.45	BDL	2077.62	BDL	1924.17	101.87	BDL	BDL	443.90	231.74	35146.14
UDR 3	2849.74	181.16	30.17	BDL	BDL	3089.02	BDL	1695.07	98.729	BDL	BDL	BDL	73.85	9978.72
UDR 4	3014.93	38.30	57.35	BDL	121.97	1941.72	337.57	9385.33	407.71	184.34	BDL	472.15	66.11	2822.70
UDR 5	4894.98	36.97	32.79	BDL	225.64	1639.84	523.73	2978.97	213.24	BDL	BDL	BDL	BDL	9057.06
UDR 6	7358.94	633.79	122.17	815.11	BDL	1944.37	BDL	550.09	99.87	BDL	494.49	1538.11	94.69	70318.04
UDR 7	1626.87	211.29	42.93	113.50	BDL	1132.03	BDL	3189.92	199.81	115.83	BDL	125.46	BDL	11287.01
UDR 8	4861.81	379.71	63.46	368.49	BDL	1361.19	BDL	939.23	86.67	BDL	83.61	293.37	BDL	51558.53
UDR 9	21565.12	38.27	125.42	337.73	BDL	839.52	BDL	5399.74	550.49	BDL	124.98	335.97	BDL	59550.83
UDR 10	28657.99	147.59	275.53	359.68	BDL	6845.27	BDL	3306.58	282.75	BDL	253.52	607.63	BDL	67796.03
UDR 11	15440.33	41.49	73.39	BDL	274.68	2348.81	BDL	3998.37	317.48	BDL	BDL	BDL	84.49	22954.89
UDR 12	4514.92	2915.73	BDL	BDL	240.39	2290.93	721.21	7967.36	373.66	BDL	BDL	BDL	BDL	9542.79
UDR 13	1042.65	1081.62	BDL	BDL	108.93	2232.71	BDL	1613.44	74.66	94.44	BDL	BDL	105.59	104.59
UDR 14	834.39	43.76	165.32	80.57	BDL	3280.46	119.67	1708.10	71.45	BDL	BDL	BDL	BDL	BDL
UDR 15	15255.33	2564.09	103.91	42.27	480.63	6208.33	288.64	2363.13	284.77	BDL	BDL	BDL	BDL	217.87

* BDL: Below Detection Limit.

The two large groups are characterized as follows:

- Group A (UDR1, UDR2, UDR6, UDR8, UDR9, UDR10 and UDR11): This group is characterized by large concentrations of lead. It is worth mentioning that the samples in this group do not appear close to each other like the other groups in the PCA.
- Group B (UDR3, UDR4, UDR5, UDR7, UDR12, UDR13 and UDR14): The samples belonging to this group are characterized by large average concentrations of iron except UDR13 and UDR14.

Sample UDR15 does not belong to any of the identified groups. Moreover, this sample shows very high concentration of iron and very low concentration of lead, which does not appear in the other samples of groups A and B.

Hierarchical cluster analysis was employed based on median linking and Bary-Curtis distances. The resulting dendrograms of the 15 ceramic sherd samples, investigating the area under the peak data, from Udhruh site are presented in Fig. (4). The dendrograms suggest that the data fall in two large groups: the first group consists of (UDR1, UDR2, UDR6, UDR8, UDR9, UDR10 and UDR11) and the second group consists of (UDR3, UDR4, UDR5, UDR7 and UDR12) while samples UDR13 and UDR14 appear together in one small group; whereas sample UDR15 still appears alone with no affiliation to any of the groups

Conclusions

This study demonstrates the growing importance of interdisciplinary research. More specifically, it demonstrates the importance of using SR-XRF in archaeological investigations. The increased need for non-destructive investigations has become a major issue in archaeometry. The work performs a chemical characterization of fifteen glazed pottery sherds dated to Ayyubid-Mamluk period from Udhruh archaeological site in southern Jordan in order to extract information about their provenance. Multivariate statistical methods display how objects from various groups can be differentiated according to their elemental composition to

obtain information on their provenance by showing similarity and clustering. The analysis presents good results concerning the fabric characterization of clay (matrix and color) and results from this report are in good agreement with these presented in Table 1. Hence, it is evident that the technique is powerful to confirm the usefulness of chemical characterization of pottery sherds and statistical techniques of data handling to complete and integrate the work of archaeologists in provenance studies.

The ceramic sherds from Udhruh show two large groups representing provenance region, while sample UDR 15 appears apart from these two groups. The latter also appears to contain very high concentration of iron, which is not observed in the other site samples. It is worth noting that the samples in group two are apart of each other, which means that they do not belong to one provenance region. Another interpretation of the variance of chemical composition of the samples of this group is that several kinds of raw material have been brought from different parts around the site to manufacture the sherds. Further analysis of this sample may clarify this point.

The significance of the present work comes from the scarcity of the studies on the Udhruh site. Therefore, the study will help archaeologists to explain the cultural contacts and behaviors during the Islamic period and contribute to better understanding of human behaviors, particularly when integrated with typological, technological and other studies.

Acknowledgment

The authors would like to thank Martin Radtke and Ivo Zizak for their valuable help and discussion on the measurement and analysis of the XRF data. We also acknowledge the synchrotron radiation source BESSY II for provision of SR. Also, we would like to thank all staff members at the BAMLine beamline for their scientific and technical support in obtaining the experimental data at Beamline. This work was supported by the IAEA/SESAME training project grant (CODE: BEAMUSER6MO).

References

- [1] Iordanidis, A., Garcia, G.J. and Karamitrou, M.G., *Materials Characterization*, 60 (4) (2009) 292.
- [2] Giussani, B., Monticelli, D. and Rampazzi, L., *Analytica Chimica Acta*, 635 (1) (2009) 6.
- [3] Cariati, F., Fermo, P. and Gilardoni, S., *Annali di Chimica*, 93 (5-6) (2003) 539.
- [4] Janssen, K.H. and Van Grieken, R., "Non-destructive Microanalysis of Cultural Heritage Materials". (Amsterdam: Elsevier, 2004).
- [5] Papadopoulou, D.N., Zachariadis, G.A., Anthemidis, A.N., Tsirliganis, N.C. and Stratis, J.A., *Talanta*, 68 (2006) 1692.
- [6] Wegstein, M., Urban, H., Rostam-Khani, P., Wittershagen, A. and Kolbesen, B.O., *Spectrochimica Acta Part B: Atomic Spectroscopy*, 52 (1997) 1057.
- [7] Milazzo, M., *Nuclear Instruments and Methods in Physics Research B*, 21 (2004) 683.
- [8] Ferrero, J.L., Roldan, C., Ardid, M. and Navarro, E., *Nuclear Instruments and Methods in Physics Research A*, 422 (1999) 868.
- [9] Zwicky, C.N. and Lienemann, P., *X-ray Spectrometry*, 33 (2004) 294.
- [10] Nuevo, M.J. and Martin, S.A., *Appl. Radiat. Isot.*, 69 (3) (2011) 574.
- [11] Dooryhe, E., Martinetto, P., Walterb, Ph. and Annea, M., *Radiation Physics and Chemistry*, 71 (2004) 863.
- [12] Mahnke, H.E., Denker, A. and Salomon, J., *C. R. Physique*, 10 (2009) 660.
- [13] Aldrabee, A., Wriekat, A., AbuSaleem, K. and Radtke, M., *Jordan J. Phys.*, 8 (3) (2015) 157.
- [14] Killick, A., *Levant*, 15 (1983) 110.
- [15] Killick, A., *Studies in the History and Archaeology of Jordan*, 3 (1987) 173.
- [16] Gregory, S., "Roman Military Architecture on the Eastern Frontier", 3 vols. (Hakkert, Amsterdam, 1996).
- [17] Killick, A., "Udruh: Caravan City and Desert Oasis". (Romsey. England, 1987).
- [18] Al-Muqaddasi, S., "The Best Divisions for Knowledge of the Regions: A Translation of Ahsan Al-taqasim fi Marifat Al-aqalim". Reading, (Centre for Muslim Contribution to Civilization, UK, 1994).
- [19] Parker, S.T., *The American Schools of Oriental Research*, 6 (1986).
- [20] Mayerson, P., *Zeitschrift für Papyrologie und Epigraphik*, 64 (1986) 141.
- [21] Pringle, D., "Crusader Castles in Jordan", In: "The Archaeology of Jordan". (Sheffield Academic Press, Sheffield, 2001), 677-684.
- [22] Graf, D., "Town and Countryside in Roman Arabia during Late Antiquity", In: "Urban Centers and Rural Contexts in Late Antiquity". (John W. East Lansing, Michigan State University Press, 2001), 219-240.
- [23] Koenen, L., *Journal of Roman Archaeology*, 9 (1996) 177.
- [24] Fiema, Z., "Late-Antique Petra and Its Hinterland: Recent Research and New Interpretations", In: "The Roman and Byzantine Near East", (Portsmouth: Rhode Island, 2002), 3: 191-254.
- [25] Schick, R., "The Settlement Pattern of Southern Jordan: The Nature of the Evidence", In: "The Byzantine and Early Islamic Near East; Land Use and Settlement Patterns", (Averill, The Darwin Press, Princeton, 1994), 2: 133-154.
- [26] Walmsley, A., "Fatimid, Ayyubid and Mamluk Jordan and the Crusader Interlude", In: "The Archaeology of Jordan". Burton, (Sheffield Academic Press, Sheffield, 2001), 515-559.
- [27] Munsell Color Company, Inc., "Munsell Book of Color Matte Finish Collection". (Baltimore Md., 1976). (Munsell Color).
- [28] Gerharz, R.R., Lantermann, R. and Spennemann, D.R., *Australian Historical Archaeology*, 6 (1988) 88.
- [29] Van Espen, P., Janssens, K. and Nobels, J., *Chemometrics and Intelligent Laboratory Systems*, 1 (1986) 109.

- [30] Ravisankar, R., Chandrasekaran, A., Kiruba, S., Raghu, Y., Prasad, M.V.R., Satpathy, K.K. and Maheswaran, C., Archives of Applied Science Research, 3 (1) (2011) 289.
- [31] Forster, N., Grave, P., Vickery, N. and Kealhofer, L., X-ray Spectrom, 40 (5) (2011) 389.
- [32] Bakraji, E.H., X-ray Spectrom., 35 (2006) 190.
- [33] Bray, J.R. and Curtis, J.T., Wisconsin Ecological Monographs, 27 (1957) 325.
- [34] Clifford, H.T. and Stephenson, W., "An Introduction to Numerical Classification", (Academic Press, London, 1975).

Jordan Journal of Physics

ARTICLE

Assessment of Indoor Radon Levels in Selected Locations within Lagos State University, Ojo, Lagos

M. A. Olaoye^a, T. J. Aluko^b, O. A. Jegede^b, M. F. Agbesi^a and O. O. Ajayi^b

^a Department of Physics, Lagos State University, Ojo Lagos State, P.M.B. 101001, Ojo, Lagos, 101001, Nigeria.

^b Department of Physics, Federal University of Agriculture, Abeokuta Ogun State, P.M.B. 2240, Abeokuta, 110001, Nigeria.

Received on: 9/2/2017;

Accepted on: 31/7/2017

Abstract: An indoor radon measurement survey was carried out in eleven offices in the campus of Lagos State University, Ojo, Nigeria using Pro series 3, radon gas detector model HS71512. The main objective of this survey was to estimate radiation doses received by the dwellers of these offices due to indoor radon exposure. For this research, radon detectors were suspended, where the ventilation slits will not be blocked at least 1.2m above the floor, a height in the breathing zone of a seated person, for 48 hours. The values of indoor concentration vary from 3.70 Bq/m³ to 218.30 Bq/m³ with an average value of 84.04 Bq/m³. The value of effective dose varies from 0.08 mSv to 3.76 mSv with an average value of 1.45 mSv.

Keywords: Indoor radon concentration, Effective dose, Average effective dose.

Introduction

Naturally occurring radon originates from the presence of radium in soil and rocks. It is generated within the mineral grains by alpha decay of radium, which migrates from the solid mineral and grains into the air through pores in the soil or ground water [1]. Radon is a chemical element having the symbol ²²²Rn and the atomic number 86. It is a radioactive, colorless, odorless and tasteless noble gas occurring naturally as an indirect decay of uranium [2].

Radon has a half-life of about 3.8 days (91hrs and 10min), a density of 9.73 kg/m³ and is one of the densest gases at room temperature (25°C). Radon is soluble in water but more soluble in organic solvents. Under normal condition, Rn is a radioactive isotope, which makes it a health hazard due to radioactive reactions [1-2].

Radon is naturally occurring as radioisotope and is about 55% main source of internal radiation exposure [3]. 1mSv of the 2.4mSv estimated average annual effective dose value is

due to radon exposure [4]. Radon concentration in air varies in accordance with location, height, material of the built houses, ventilation rate at homes and meteorological parameters [5-8].

A combined analysis of lung cancer mortality among 11 cohorts of underground miners confirmed that high levels of exposure to radon are associated with increased lung cancer risk. Cellular mutagenesis studies, experimental research in animals and occupational epidemiologic studies have established radon as a human lung carcinogen [9]. Several studies have been carried out on indoor radon in various parts of the world [7, 10, 11].

Potential hazard of exposure to radon gas radiation from natural background, e-waste, dumpsites, quarries, underground water, building materials and cracks in walls, among others, cannot be underestimated.

Despite the associated hazards of radon, it is used as tracer in studying indoor and outdoor air

and investigating atmospheric conductivity and mobility spectra. Research on radon inhalation and ingestion in Africa and the developing countries is still minimal.

The present research was carried out at the campus of Lagos State University, Ojo, Nigeria (situated at 6.4677°N and 3.180°E) to provide information on radon concentration levels and risk of lung cancer in some offices at the campus. Radon concentration level was measured in 11 offices within the vicinity of the university. The choice of the offices was strategically pre-determined with respect to natural potential factors that influence concentration level, yet all occurring in the most natural conditions.

Material and Methods

In this study, an active electronic device (Pro series 3, radon gas detector) was employed for the measurement of indoor radon in 11 offices in the above-mentioned university. The detector measures radon in picocuries per litre (pCi/L). It was pre-calibrated to measure radon activity between 0.0 and 999.9pCi/L and measured values were converted to Bq/m³ by multiplying the measured value by 37.

Pro series 3 radon gas detector was designed to take samples for 48 hours before an accurate result can be displayed. For the same location, the readings are updated every hour and new values of indoor radon concentration are consequently displayed if the concentration of radon differs from the initial stored value previously determined from the 48-hour

sampling. Radon samples were classified based on WHO, 2009 handbook on indoor radon.

Sampling Procedure

Sampling was conducted in eleven offices containing the same building materials and having the same dimensions and geographical age. The dimensions of the offices were within a floor area of 21m², a gross volume of 63m³ and a net volume of about 56.38m³ (obtained by subtracting the volume of fixture). Natural ventilation conditions involving opening of windows and doors were employed during the period of measurement.

The radon gas detector was suspended where the ventilation slits will not be blocked and such that it was at least 1.2m above the floor, a height in the breathing zone of a seated person. The detector was at least 0.9m from windows, doors or any other potential openings in the exterior walls. No objects were placed within 0.1m from the detector. These positions, which were fixed throughout this work, were maintained, since it was shown that radon level depends remarkably on the sampling position. These procedures were followed according to the research work conducted by [12].

Results and Discussion

The annual average radon concentration, average effective dose, lifetime fatality risk and excess lifetime cancer risk for each study location have been calculated as shown in Table1.

TABLE 1. Radon concentration and annual effective dose.

S/N	Sampling Points	Radon Concentration (pCi/L)	Radon Concentration (Bq/m ³)	Annual Exposure WLM	Lifetime Fatality Risk X10 ⁻⁴	Annual Effective Dose (mSv)	ELCR
1	OF1	4.60	170.20	0.76	2.28	2.95	11.36
2	OF2	5.90	218.30	0.97	2.91	3.76	14.48
3	OF3	0.10	3.70	0.02	0.06	0.08	0.31
4	OF4	0.20	7.40	0.03	0.09	0.12	0.46
5	OF5	1.50	55.50	0.25	0.75	0.97	3.73
6	OF6	0.40	14.80	0.06	0.18	0.23	0.89
7	OF7	5.20	36.40	0.16	0.48	0.62	2.39
8	OF8	1.70	62.90	0.28	0.84	1.09	4.20
9	OF9	4.80	177.60	0.79	2.37	3.07	11.82
10	OF10	4.30	159.10	0.71	2.13	2.75	10.59
11	OF11	0.30	18.50	0.08	0.24	0.31	1.19

The values of indoor concentration vary from 3.70 Bq/m³ to 218.30 Bq/m³ with an average value of 84.04 Bq/m³. Radon concentration was used to calculate the annual exposure in working level months (WLM) using the following equation [15]:

$$\text{Annual Exposure (WLM)} = \frac{FC_o}{3700} \frac{t}{170} \quad (1)$$

where $t = 8760\text{h/y}$ is the number of hours per year, C_o is the radon concentration in Bq/m³ and F is the equilibrium factor (0.4).

The conversion factors of 3×10^{-4} WLM and 3.88 mSvWLM [3] are used for calculating the lifetime fatality risk and the annual effective dose, respectively. The value of effective dose varies from 0.08 mSv to 3.76 mSv with an average value of 1.45 mSv, while the excess lifetime cancer risk (ELCR) is given as:

$$\text{ELCR} = \text{AEDE} * \text{DL} * \text{RF} \quad (2)$$

where AEDE, DL and RF are the annual effective dose, duration of life of 70 years and risk factor of 0.05, respectively.

Conclusion

In this study, radon concentration levels in some offices in Lagos State University, Ojo were measured with the average radon concentration higher than the world average radon concentration of 40 Bq/m³ [13]. This might be as a result of low air flushing, ventilation and location of these offices, since the higher the elevation in a building, the lower the radon level [14] and that higher concentration of radon are present in basement and ground floor buildings. Furthermore, radon operates through the process of diffusion, where the farther from the contact source the lower the concentration of radon. The radiological implication of these values should not be ignored and periodical studies of offices should be carried out for monitoring and proactive actions taken.

References

- [1] Mehra, R. and Bala, P., Pelagia Research Library, 4(1) (2013) 212.
- [2] Kant, K., Upadhyay, S.B., Sharma, G.S. and Chakervarti, S.K., Iran J. Radiat. Res., 1(4) (2004) 181.
- [3] ICRP, "Protection against Radon-222 at Home and at Work". International Commission on Radiological Protection, (Oxford: Pergamon Press, ICRP Publication No.65, 1993).
- [4] UNSCEAR, "Sources, Effects and Risks of Ionizing Radiation", United Nations Scientific Committee on the Effects of Atomic Radiation, Report to the General Assembly, (United Nations, New York, 2000).
- [5] Salih, L.M., Journal of Al-Nahrain University, 17(3) (2014) 94.
- [6] Mustapha, A.O., Alatis, O.O., Okeyode, I.C., Makinde, V., Akinyemi, O.D., Akinboror, F.G., Rabi, A.J., Dawodu, G.A., Gbadebo, A.M., Olaoye, M.A., Okedeyi, A.S. and Al-Azmi, D., Proceedings of an International Symposium, Beijng, China, (2013) 645-651.
- [7] Obed, R.I., Lateef, H.T. and Ademola, A.K. Journal of Medical Physics, 35(4) (2010) 242.
- [8] Quarto, M., Pugliese, M., La Verde, G., Loffredo, F. and Roca, V., Int. J. Environ. Res. Public Health, 12 (2015) 14948.
- [9] Krewski, D., Lubin, J.H., Zielinski, J.M., Alavanja, M., Catalan, V.S., William Field, R. and Sandler, D.P., Journal of Toxicology and Environmental Health, Part A, 69(7-8) (2006) 533.
- [10] Rahman, S., Faheem, M., Rehman, S. and Matiullah, Radiat. Prot. Dosimetry, 121 (2006) 333.
- [11] Virk, H.S. and Sharma, N., Proceedings of Fifth International Conference on High Levels of Natural Radiation and Radon Areas: Radiation Dose and Health Effects. Germany: Munich, (2000) 193.
- [12] Oni, O.M., Isola, G.A., Oladapo, O.O. and Oni, E.A., Research Journal of Environmental and Earth Sciences, 4(1) (2012) 131.
- [13] World Health Organization, WHO Handbook on Indoor Radon: A Public Health Perspective (Internet). Geneva, WHO, 2009. http://whqlibdocwho.int/publications/2009/9789241547673_eng.pdf.
- [14] Shirav, M. and Vulkan, V., Environ. Geol., 31(3-4) (1997) 167.
- [15] Mansur, H.H., Radiation Measurement, 40 (2005) 544.

Fuel Ignition Conditions in Thermonuclear Fusion

M. Mahdavi

Physics Department, University of Mazandaran, P.O.Box 47415-416, Babolsar, Iran.

Received on: 27/2/2017;

Accepted on: 16/7/2017

Abstract: The isobaric and isochoric models of inertial confinement fusion (ICF) are compared in hot spot concept. Heating and cooling mechanisms of fuel are theoretically investigated. Some corrections are suggested to improve the Bremsstrahlung emission calculation at ultra-relativistic regime and super high temperature plasma situation. An admissible region of values is determined which satisfy hot spot spark-ignition condition to start a self-sustaining fusion burn. An optimized point of this region is specified to achieve a maximum fuel gain. The density and radius of this optimum point are determined applying a hydrodynamic model. The results show that a fuel gain maximum will be achieved with the required minimum laser energy supply through the optimization process.

Keywords: Isobaric, Isochoric, Spark-ignition, Self-sustaining burn, Fuel gain.

Introduction

For a typical inertial confinement fusion, ICF, target implosion will undergo four phases: ablation, compression, ignition and burn. The energy delivering to the target is based on direct or indirect irradiation. The ignition starts in conventional manner or isobaric model at the consequence of high compression and hot spot formation in center of pellet, but during the implosion stage, some accompanying hydrodynamic instabilities such as; *Rayleigh - Taylor* and *Richtmyer - Meshkov* instabilities, set an upper limit on the implosion velocity and then tend at first to destroy the imploding shell and later hinder the formation of the central hot spot [1, 2]. There is an alternative approach to ICF; namely isochoric model in which these instabilities have no important role. In isochoric model, compression and ignition stages are distinct [3]. In isochoric fast ignition model, the energy is delivered to the target at three stages: at first the compression with usual laser, second, hole boring with a short pulse laser beam (usually 10^{18} W/cm^2 and 100 ps) drilling a hole through the under dense plasma surrounding the dense fuel core [4] (this hole acts as an open

channel which is relatively free of plasma for the ignition pulse to reach the pre-compressed fuel with minimum energy loss). In the third phase, an ultra-short pulse with a power in excess of a petawatt is used to ignite the fuel [5]. The pellet consists of three regions known as: the ablator, a layer of solid-ice fuel occupying most of the volume and central region of Deuterium-Tritium ($D - T$) gas [6]. During implosion, the layer of fuel has a velocity in the order of $3 - 4 \times 10^7 \text{ cm/s}$ at the stagnation time (the end of implosion phase). The main fuel conversion ratio is: $\frac{R_0}{R_c} = 20 - 40$ and the ratio of outer shell to hot spot radius is typically $\frac{R_c}{R_s} \approx 10$. The hot spot life time is assumed approximately $(100 - 200) \text{ ps}$ [1, 2, 4]. To achieve a maximum gain from an optimized condition, it is necessary to consider the ignition and spark formation conditions simultaneously.

This paper is organized as follows: in section 2, the heating and cooling mechanisms in hot spot region are discussed. Section 3 investigates the conditions to achieve an optimal point of hot spot areal density and temperature leading to

maximum fuel gain. In section 4, the parameters of optimized point versus laser energy driver are specified by applying hydrodynamic model. In section 5, the fuel gain calculation corresponding to optimal point values in isochoric fuel is performed. Finally, section 6 presents a conclusion about optimization process in ICF context.

Heating and Cooling Mechanisms in Hot Spot Region

In Deuterium-Tritium ($D - T$) fusion reaction, ${}^2_1D + {}^3_1T \rightarrow {}^4_2\alpha(3.5MeV) + {}^1_0n(14.1MeV)$, the energy contributions are related to masses ratio as: $\frac{E_\alpha}{E_n} = \frac{M_n}{M_\alpha} \approx \frac{1}{4}$. The neutron mean free path is $l_n = \frac{1}{\sigma n_i}$, where n_i and σ are the ion density and the cross section averaged over the plasma ions, respectively. For $D - T$ plasma, $\rho_n l_n = 4.7 g/cm^2$. This is much larger than $\rho_s R_s$ of a typical igniting hot spot ($\approx 0.3 g/cm^2$). Therefore, the neutron energy deposition can be neglected for central ignition. So, when a $D - T$ fusion reaction is started in ignition region, 20 percent of the energy deposition of α particles is considered as a heating mechanism. On the other hand, if the plasma to be considered is optically thin, the cooling mechanisms will be mainly Bremsstrahlung emission, electron thermal conduction for isobaric model and in addition, mechanical work due to fuel expansion in isochoric model. To generate a spark in hot spot region, firstly the cooling time should be greater than the time of mechanical wave propagation (sound) which corresponds to disassembly time or confinement time of spark region (spark formation condition). Secondly, the thermonuclear heating rate should be greater than the cooling rate [7]. The volumetric power generation from α particle energy deposition can be determined by [1, 8]:

$$P_\alpha = 1/5 P_{(\alpha+n)} = A_\alpha < \sigma v > \rho_s^2 f_\alpha \quad (1)$$

where ρ_s and f_α are hot spot density and the fraction of alpha particles that remain in the spark region and deposit their energy, respectively. $A_\alpha = 8 \times 10^{40} erg/g^2$ and $< \sigma v >$ is reactivity which is given by[9]:

$$< \sigma v > = \exp \left[A_1 + A_2 \left| \ln \frac{T_s}{A_3} \right|^{A_4} \right] (cm^3/s) \quad (2)$$

where $A_1 = -34.629731$, $A_2 = -0.57164663$, $A_3 = 64.221524$ and $A_4 = 2.1373239$. The plasma has non-degenerate state with a Maxwellian energy distribution function; therefore, the volumetric power loss of Bremsstrahlung from a hydrogen isotope plasma by same temperature assumption for electrons and ions in spark region $T_s = T_e = T_i$ can be given by [1,7]:

$$P_{br}(erg, s^{-1}, cm^{-3}) = 3.36 \times 10^{-24} n_e \times (n_T + n_D) T_s^{\frac{1}{2}} \quad (3)$$

where n_e , n_T and n_D are electron, tritium and deuterium densities in cm^{-3} , respectively and T_s is the hot spot temperature. For equimolar fuel, $n_T = n_D = n_e/2$; so, we have:

$$P_{br}(erg, s^{-1}, cm^{-3}) = 3.36 \times 10^{-24} n_s^2 T_s^{1/2}. \quad (4)$$

The above equation is only valid in non-relativistic regime with Maxwellian distribution function. In this regime, the e-i collisions are only important and the quantum relativistic corrections are not included. Some quantum relativistic corrections are needed at the ultra-relativistic regimes. Firstly, non-relativistic Maxwellian distribution function (for non-degenerate plasma) should be replaced by relativistic distribution function. Secondly, the quantum relativistic and the screening effect corrections are strongly necessary to apply in differential cross-section equations. Also, the Bremsstrahlung emission due to e-e collisions should be taken into account. The relativistic Maxwellian energy distribution function is given by:

$$\begin{aligned} f(v) &= \left[2 \left(\frac{T_e}{mc^2} \right)^2 K_1 \left(\frac{mc^2}{T_e} \right) \right. \\ &\quad \left. + \left(\frac{T_e}{mc^2} \right) K_0 \left(\frac{mc^2}{T_e} \right) \right]^{-1} c^{-3} v^2 \gamma^5 \exp \left(-\frac{\gamma mc^2}{T_e} \right) \end{aligned} \quad (5)$$

where m is the electron rest mass, c is light velocity, K_1 and K_0 are the modified Bessel functions of the second kind.

Applying the quantum relativistic and the screening effect corrections indicated as Gaunt factor $G(E_k, hv)$ on *Kramer's* cross-section, the improved differential cross-section is read as:

$$\frac{d\sigma(E_k, hv)}{d(hv)} = G(E_k, hv) \frac{d\sigma_{kr}(E_k, hv)}{d(hv)}. \quad (6)$$

Here, $G(E_k, hv)$ represents corrections including quantum, relativistic and screening effects. Although $G(E_k, hv)$ is a complex function of E_k and (hv) , in our discussion we consider a simple approximation for $G(E_k, hv)$ as $G \approx \frac{2\sqrt{3}}{\pi} \approx 1.10$ [1]. Kramer's cross-section is given as:

$$\frac{d\sigma_{kr}(E_k, hv)}{d(hv)} = \frac{Z^2}{hv \left(\frac{v}{c}\right)^2} S_{kr} \quad (7)$$

$$S_{kr} = \frac{16\pi}{3^{1/3}} \alpha_{fs}^3 \left(\frac{\hbar}{mc}\right)^2 \quad (8)$$

where $v.m$ and α_{fs} are the relative velocity of particles (which simply can be related to energy parameters), the emitter rest mass and fine structure constant, respectively. For electron, we have: $S_{kr} = 5.61 \times 10^{-31}$. The emitted *Volumetric power (Specific power)* of electrons

with distribution function $f(v)$ in plasma medium is obtained by:

$$P_{br}^{e-i, e-e}(hv) = \int \frac{d\sigma^{e-i, e-e}(E_k, hv)}{d(hv)} n_{i,e} n_e v f(v) dv. \quad (9)$$

Fig.1 shows Bremsstrahlung specific power versus electron energy by comparing relativistic and non-relativistic Maxwellian energy distribution functions while the improved formula on differential cross-section is applied too. It is found that the considerable difference in results is only formed at high temperature far from ICF region ($T \gg 5 - 10$ keV). So, these corrections are only necessary for fuels with ultra-temperatures. It should be noticed that in degenerate plasma practically, there is no considerable Bremsstrahlung emission.

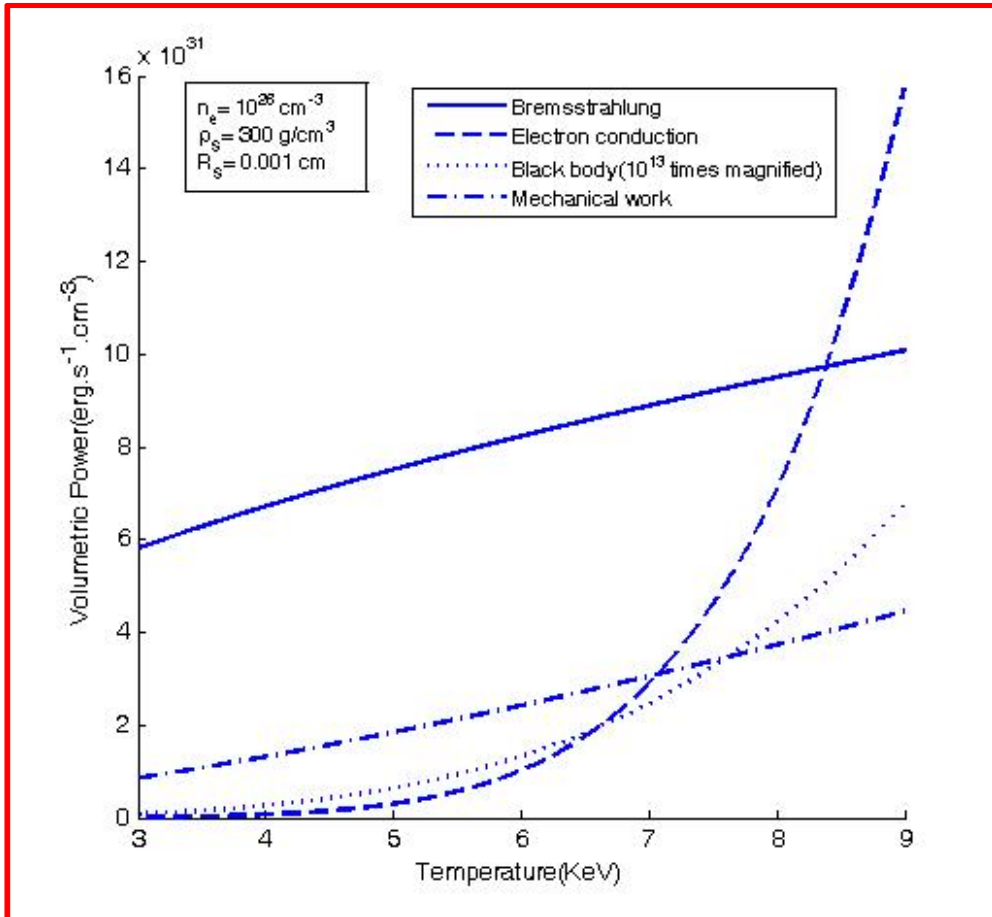


FIG. 1. The variation of Bremsstrahlung (solid line), electron conduction (dashed line), black body (dotted line, 10^{13} times magnified) and mechanical work (dash-dotted line) versus plasma temperature.

Volumetric power loss of electrons' thermal conduction in hot spot is determined by [1]:

$$P_{ec}(erg, s^{-1}, cm^{-3}) = -\frac{\chi_e \nabla T_s S}{V} \quad (10)$$

where S and V denote the surface and volume of hot spot region,

$A_e = 9.5 \times 10^{19} \left(\text{erg}, s^{-1}, \text{cm}^{-3} \text{keV}^{-\frac{7}{2}} \right)$,
 $\chi_e = A_e T_e^{5/2} / \ln \Lambda$, where $\ln \Lambda$ is Coulomb logarithm which is given by [7]:

$$\ln \Lambda = \ln \left(60 T_s \sqrt{\frac{2.5}{\rho_s}} \right). \quad (11)$$

So, finally we will have:

$$P_{ec}(\text{erg}, s^{-1}, \text{cm}^{-3}) \simeq \frac{3 C_e A_e T_s^{7/2}}{\ln \Lambda R_s^2} \quad (12)$$

where C_e is a numerical coefficient close to unity. The other cooling mechanism in hot spot is mechanical work due to pressure imbalance between hot spot P_s and surrounding fuel P_c . When the igniting fuel is perfectly isobaric ($P_s = P_c$), then there is no mechanical work, but when the fuel is isochoric, there is a large pressure gradient between hot spot and surrounding fuel $P_s \gg P_c$, so that a shock is driven into the lower pressure cold fuel. The volumetric mechanical work power is given by [1]:

$$P_m(\text{erg}, s^{-1}, \text{cm}^{-3}) = A_m \rho_s R_s^{-1} T_s^{3/2} \quad (13)$$

with $A_m = 0$ for isobaric ignition and $A_m = 5.5 \times 10^{22} \text{cm}^3 \text{s}^{-3} \text{keV}^{-3/2}$ for isochoric ignition and ρ_s, R_s and T_s are density, radius and temperature of hot spot, respectively. When the radius of hot spot is much smaller than Planck mean free path of photons, $l_{ph} = 14.4 T_s^{7/2} / \rho_s^2$, ($l_{ph} = 14.4 T_s^{7/2} / \rho_s^2$), the plasma will be optically thin and black body radiation as a cooling mechanism is negligible (for example, $\rho_s = 300$, $R_s = 0.001 \text{cm}$, $T_s = 7.5 \text{keV}$, $l_{ph} = 0.1849 \text{cm}$, $R_s / l_{ph} = 0.0054$). The volumetric power of black body radiation is determined by $P_{bb}(\text{erg}, s^{-1}, \text{cm}^{-3}) = \sigma_B T_s^4 R_s^{-1}$, where $\sigma_B = 1.03 \times 10^{24} \text{erg}, s^{-1}, \text{cm}^{-2}, \text{keV}^{-4}$. On the other hand, the mechanisms of heating through reabsorption such as Compton scattering and inverse Bremsstrahlung are also negligible due to thinness condition. Fig. 2 shows the contribution of each different cooling mechanism versus temperature of overdense plasma.

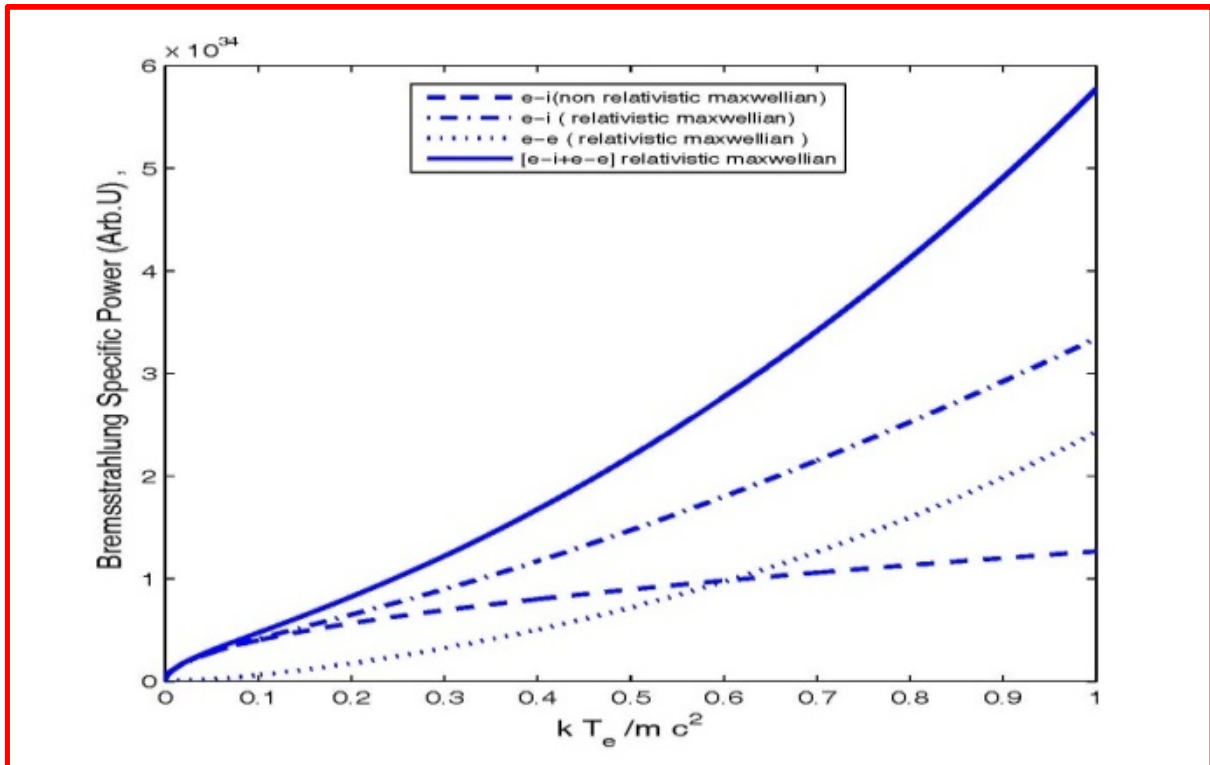


FIG. 2. Bremsstrahlung specific power versus electron energy normalized to electron rest mass with relativistic and non-relativistic Maxwellian energy distribution functions.

Optimization Condition to Achieve Maximum Fuel Gain

To achieve a self-heating fusion burn condition, it is needed to determine the

admissible region inside the enclosed area between the spark formation and ignition condition curves through crossing them in $H_s - T_s$ plane, where H_s is the areal density of hot spot. Optimal point which leads to a

maximum gain is actually the minimum point of this admissible region.

The ignition condition for isobaric fuel is written as:

$$P_\alpha + P_n + P_{Re} \geq P_{br} + P_{ec} + P_{bb}. \quad (14)$$

The plasma is assumed optically thin, so that the reabsorption mechanisms P_{Re} and black body radiation P_{bb} contributions are neglected [9]. Because the value of neutron mean free path is greater than hot spot areal density, the neutron heating contribution P_n is also neglected. Finally, the above relation leads to:

$$\left(A_\alpha < \sigma v > f_\alpha - A_{br} T_s^{\frac{1}{2}}\right) H_s^2 - \frac{3C_e A_e T_s^{7/2}}{\ln \Lambda} \geq 0. \quad (15)$$

On the other hand, condition for a thin isochoric fuel is written as:

$$P_\alpha \geq P_{br} + P_{ec} + P_m. \quad (16)$$

This leads to:

$$\left(A_\alpha < \sigma v > f_\alpha - A_{br} T_s^{\frac{1}{2}}\right) H_s^2 - A_m T_s^{\frac{3}{2}} H_s - \frac{3C_e A_e T_s^{7/2}}{\ln \Lambda} \geq 0. \quad (17)$$

The spark formation condition can be written as [10]:

$$t_{co} \leq t_c \quad (18)$$

where t_{co} and t_c are confinement time and cooling time scale, respectively. Confinement time is given by:

$$t_{co} = \frac{R_s}{c_s} \quad (19)$$

where $c_s = 3.5 \times 10^7 T_s^{1/2}$ (cm/s) with T_s in keV is sound propagation velocity in $D-T$ homogenous plasma. The cooling time scale is also given by [7]:

$$t_c = \frac{3kn_s T_s}{P_{br} + P_{ec}} \quad (20)$$

where $k = 1.6 \times 10^{-9}$ erg/keV. Finally, by substituting Eqs. (19 and 20) in Eq.18 we shall have:

$$(7.6) \frac{H_s}{T_s} + (7.1 \times 10^{-3}) \frac{T_s^2}{H_s \ln \Lambda} \leq 1. \quad (21)$$

According to Fig. 3, this optimized point is $H_s = 0.25 \text{ g/cm}^2$ and $T_s = 5 \text{ keV}$ for isobaric fuel and $H_s = 0.3 \text{ g/cm}^2$ and $T_s = 7.5 \text{ keV}$ for isochoric fuel.

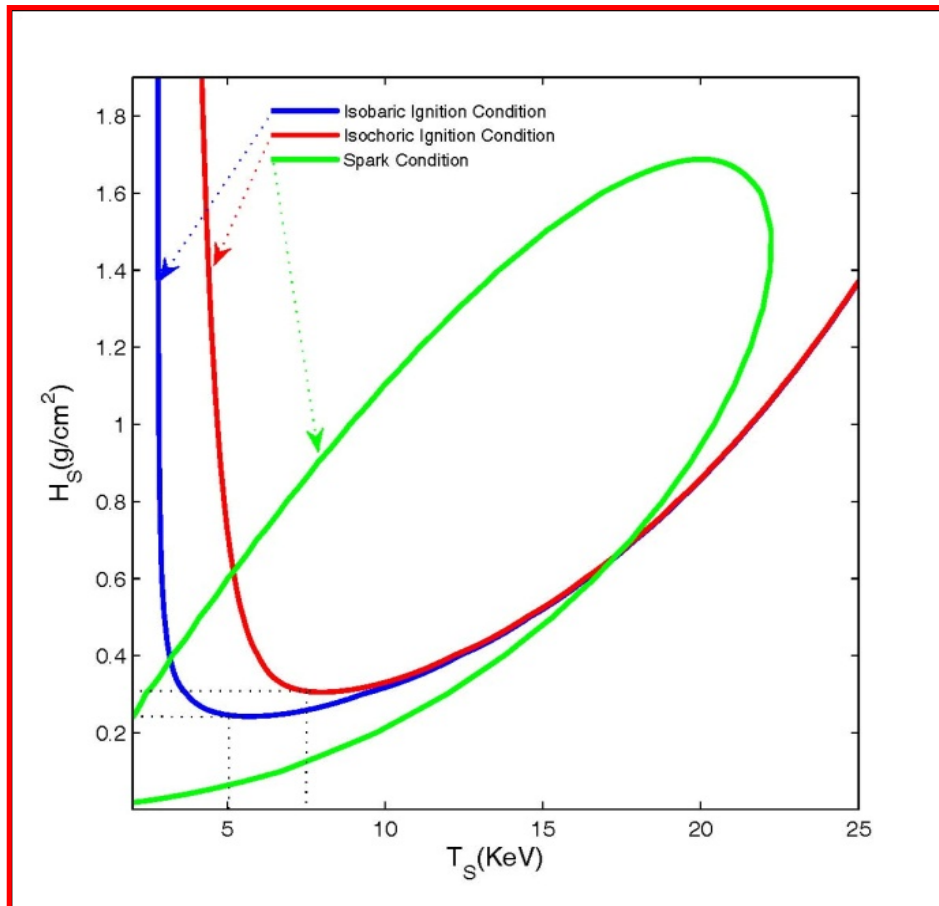


FIG. 3. Crossing of spark formation and ignition condition curves in $(H_s - T_s)$ plane to obtain optimal point.

Hot Spot Parameters According to Optimal Point

The parameters of optimized point in self-heating condition can be determined versus implosion parameters by hydrodynamic model of shock- ignition. The characteristics of hot spot and the surrounding shell versus implosion parameters are listed in Table. 1 [11]. While $\alpha = \frac{P_c}{P_{FD}}$ is isentropic parameter with P_{FD} as Fermi degenerate pressure, $\epsilon = \frac{P_c}{P_s}$ indicates the dropping pressure factor and $\beta = \frac{H_s}{0.4}$. Considering $\eta E_L = E_c + E_s$ and the fuel mass as $M_F = M_c + M_s$, by substituting the related formulae, the fuel mass can be obtained as:

$$M_F = \frac{\eta E_L - 2.4 \times 10^3 (\gamma \beta)^3 \epsilon^2 P_c^{-2}}{3.9 \alpha^{3/5} P_c^{2/5}} + 4.3 \frac{\beta^3 (\gamma \epsilon)^2}{P_c^2}. \quad (22)$$

In **isobaric** fuel, the shell pressure is equal with hot spot region, but in **isochoric** fuel, the density of shell is equal with the hot spot. The laser energy versus hot spot radius R_s is shown in Fig. 4 in optimized point, $H_s = 0.25 \text{ g/cm}^2$, $\beta = \frac{0.25}{0.4}$, $\gamma = 5/3$, $\epsilon = 1$ and assuming $\eta = 0.1$. $M_F = 0.3 \text{ (mg)}$ for isobaric fuel. It is shown that the minimum laser energy corresponds to hot spot radius $R_s = 8.33 \times 10^{-4} \text{ cm}$ and density $\rho_s = 300 \text{ g/cm}^3$. Repeating this route to determine the values for isochoric fuel, according to Fig. 5, $R_s = 10^{-3} \text{ cm}$, $\rho_s = 300 \text{ g/cm}^3$ and $\epsilon = 0.03$ correspond to minimum required laser energy. In addition, Figs. 4 and 5 show the pellet conversion ratio and the variation of shell radius too. The conversion ratio in isobaric fuel is greater than the isochoric one (about 30/20); therefore, more compression energy is needed with an increase in hydrodynamic instabilities.

Fuel Gain in Isochoric Fuel

The fuel gain in isochoric fuel is: $\frac{E_F}{E_c + E_{ig}}$, where E_F , E_c and E_{ig} indicate the fusion released energy, compression energy and the ignition energy required to supply the fuel driver to start fusion reaction, respectively. The fusion energy is determined by:

$$E_F = \epsilon_{DT} f_b M_F \quad (23)$$

where $f_b = \frac{\rho R}{\rho R + 7}$, $\rho R = H_F$ is fuel areal density and $\epsilon_{DT} = 17.6/5 \text{ AMU}$ is specific fusion energy. Then, the fusion released energy is rewritten as:

$$E_F (\text{MJ}) = 3.37 \times 10^5 \left(\frac{\rho R}{\rho R + 7} \right) M_F. \quad (24)$$

According to implosion parameters, the fuel areal density is $\rho R = 0.4\beta + \rho_c(R_c - R_s)$ [11]. The compression energy required to compress the fuel to η times more than liquid hydrogen density in isentropic model is given by:

$$E_c (\text{MJ}) = 0.12 \alpha \eta^{2/3} M_F \quad (25)$$

where $\eta^{2/3} = \frac{H_F}{H_0} \cdot H_0 = \left(\frac{3M_F \rho_0}{4\pi} \right)^{1/3}$ and ρ_0 is liquid hydrogen density ($67.8 \times 10^{-3} \text{ g/cm}^3$). The ignition energy is given by:

$$E_{ig} = 3 f_s T_s \left(\frac{M_F}{M_i} \right) \quad (26)$$

where $f_s = \left(\frac{M_s}{M_F} \right) = \left(\frac{H_s}{H_F} \right)^3$. Submitting $M_i = 25 \text{ g}$ as ion average mass and the value of f_s in Eq. 26, the ignition energy is rewritten as:

$$E_{ig} = 0.00324 T_s \left(\frac{M_F}{H_F^3} \right). \quad (27)$$

The fuel gain can be determined by applying the optimal point parameters to Eqs. (24, 25 and 27). Fig. 6 shows that the fuel gain is maximized just in optimized point ($H_s = 0.3 \text{ g/cm}^2$).

TABLE 1. Some useful relations which are driven from hydrodynamics shock-ignition model [11].

Quantity	Hot spot	Main fuel
(Density: g/cm^3)	$\rho_s = \frac{0.4\beta}{R_s}$	$\rho_c = 51 \left(\frac{\beta \gamma \epsilon}{\alpha R_s} \right)^{3/5}$
(Energy: MJ)	$E_s = 10^3 \beta \gamma R_s^2$	$E_c = 0.32 \alpha \rho_c^{2/3} M_c$
(Mass: g)	$M_s = \frac{4\pi}{3} \rho_s R_s^3$	$M_c = 0.21 \left(\frac{R_s}{\beta \gamma \epsilon} \right)^{2/5} \alpha^{-3/5} \times (\eta E_L - E_s)$
(Radius: cm)	$R_s = \frac{0.4\beta}{\rho_s}$	$R_c = \left(\frac{3M_c}{4\pi \rho_c} + R_s^3 \right)^{1/3}$
(Pressure: MBar)	$P_s = \frac{1.6\beta \gamma}{R_s}$	$P_c = 2.2 \times 10^{-3} \alpha \rho_c^{5/3}$

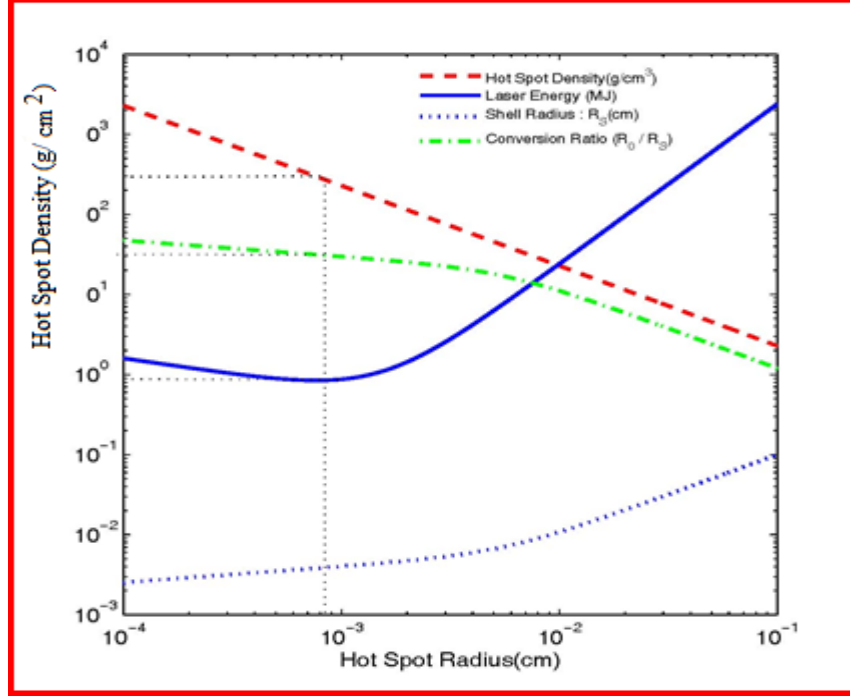


FIG. 4. The variation of hot spot density (g/cm^2 , dashed line), laser driver energy with coupling efficiency $\eta_L = 0.1$ (MJ, solid line), surrounding shell radius (cm, dotted line) and fuel conversion ratio (R_0/R_S , dot-dashed line) with considering optimal point ($H_S = 0.25 g/cm^2$, $T_S = 5 keV$) of isobaric fuel versus hot spot radius.

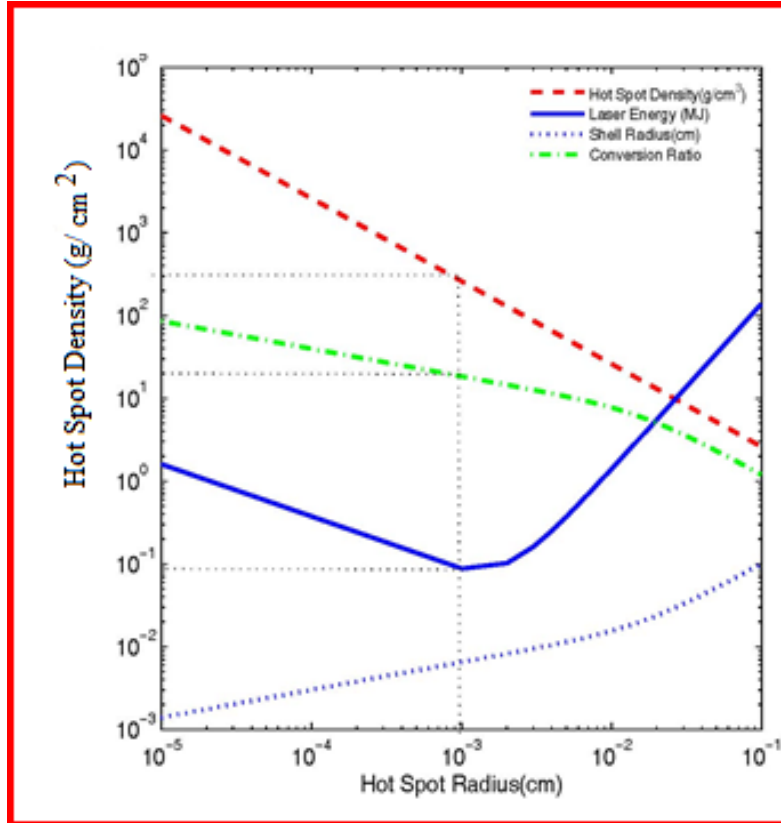


FIG. 5. The variation of hot spot density (g/cm^2 , dashed line), laser driver energy with coupling efficiency $\eta_L = 0.1$ (MJ, solid line), surrounding shell radius (cm, dotted line) and fuel conversion ratio (R_0/R_S , dot-dashed line) with considering optimal point ($H_S = 0.3 g/cm^2$, $T_S = 7.5 keV$) of isochoric fuel versus hot spot radius.

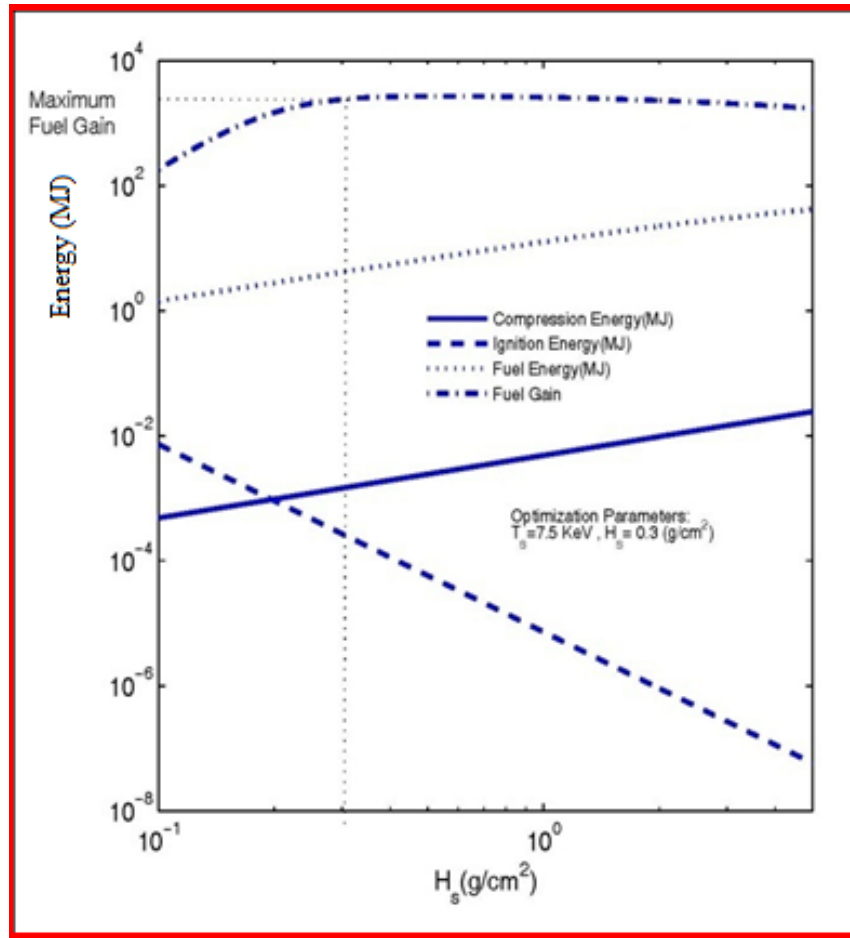


FIG. 6. The variation of compression energy (MJ, solid line), ignition energy (MJ, dashed line), fuel energy (MJ, dotted line) and fuel gain (dot-dashed line) versus hot spot areal density (g/cm^2) for isochoric fuel.

Conclusion

To obtain the required conditions to start a self-sustaining fusion burn, it is necessary to apply spark formation and ignition conditions simultaneously. Crossing the related curves gives an admissible region of hot spot areal density and temperature values which satisfy a self-sustaining fusion burn ($H_s = 0.3 \text{ g/cm}^2$, $T_s = 7.5 \text{ keV}$ (isochoric fuel)) (Fig. 3). The special values of radius and density ($R_s = 0.001 \text{ cm}$, $\rho_s = 300 \text{ g/cm}^3$ (isochoric fuel)) which correspond to required minimum laser energy describe the real optimized point of hot spot determined through applying the hydrodynamic model. It is shown that to calculate bremsstrahlung emission at high temperature ($T_e \gg 5 - 10 \text{ keV}$), some important corrections must be included, such as; relativistic

Maxwellian distribution function and quantum relativistic effects (Gaunt factor) on differential cross-sections. Also, it is not necessary to include the black body radiation (as cooling mechanism) and the reabsorption mechanism (as heating mechanism) in energy balance equation for optically thin plasma. The isochoric fuel needs less energy than the isobaric fuel in optimal point. In isobaric model, the shell with density about 8 times greater than hot spot should be compressed with higher pellet conversion ratio; therefore, higher compression energy is necessary. So, a higher fuel gain is obtained from the isochoric model (about 8000), while it is needed to generate a hot spot with higher areal density and temperature in the isobaric model.

References

- [1] Atzeni, S. and Meyer Ter Vehn, J., "Inertial Fusion", (Oxford Science Publication, 2004).
- [2] Pfalzner, S., "An Introduction to Inertial Confinement Fusion", (Taylor and Francis Group, LLC, 2006).
- [3] Kidder, R.E., Nucl. Fusion, 16 (1976) 405.
- [4] Tabak, M., Hammer, J., Glinsky, M.E., Eilks, S.C. et al., Phys. Plasma, 1 (1994) 1626.
- [5] Guérin, S.M., Bell, A.R., Davies, J.R. and Haines, M.G., Plasma Phys. Contr. Fusion, 41 (1999) 285.
- [6] Jones, O.S., Schein, J., Rosen, M.D., Suter, L.J., Wallace, R.J. et al., Phys. Plasma, 14 (2007) 056311.
- [7] Basko, M.M., Plasma Phys. Contr. Fusion, 30 (1990) 2443.
- [8] Basko, M.M., Nucl. Fusion, 35 (1995) 1.
- [9] Piriz, A.R., Nucl. Fusion, 36 (1996) 1395.
- [10] Pourhosseini, S. and Ghasemizad, A., J. of Theoretical and Applied Phys. (JTAP), 3 (2009) 7.
- [11] Lafon, M., Ribeyre, X. and Shurtz, G., Phys. Plasma, 17 (2010) 52704.

Assessment of Human Exposures to Radiation Arising from Radon in Groundwater Samples from Parts of Abeokuta, Ogun State, Nigeria

J. A. Rabi^a, O. A. Mustapha^b, V. Makinde^b and A.M. Gbadebo^c

^a Department of Physics, Federal University, Kashere, P.M.B. 0182, Gombe State, Nigeria.

^b Department of Physics, Federal University of Agriculture, Abeokuta, P.M.B. 2240, Abeokuta, Nigeria.

^c Department of Environmental Management and Toxicology, Federal University of Agriculture, Abeokuta, P.M.B. 2240, Abeokuta, Nigeria.

Received on: 11/3/2017;

Accepted on: 8/8/2017

Abstract: This study aimed at assessing the level of radiation dose arising from consumption of well-water from different parts of Abeokuta metropolis by measuring the concentrations of ^{222}Rn and ^{220}Rn in well-water samples using two types of solid state nuclear track detector; namely, CR-39 and LR-115. At each well location, water sample of 3.7ml was dispensed into two specially designed plastic cups. The two detectors were exposed to alpha particles emitted by ^{222}Rn , ^{220}Rn and their decay products emanating from each water sample for forty days. The ^{222}Rn concentration obtained ranged from 3.1 to 90.8 kBq/m³. The statistical analysis of radon concentration showed that 94% of the wells studied had radon concentration above the United States Environmental Protection Agency's maximum contaminant level of 11.1 kBq/m³, while none of the samples had up to 1000 kBq/m³ above which remedial action is recommended by the European Union. The calculated ranges and means of the annual effective doses from water consumption for children and adults are 44.5-1325.7, 484.7 and 22.3-66.8, 242.3μSv/y, respectively. These results showed that radon in drinking water could constitute a radiological concern for people in the areas studied.

Keywords: Radionuclides, Radon concentration, Groundwater, Effective dose, Human exposure.

Introduction

The chemical composition of groundwater does not affect the activity concentration of ^{222}Rn . The main parameters that affect the activity concentration of ^{222}Rn in groundwater are the activity concentration of ^{226}Ra in bedrock and soil, rock porosity and the ^{222}Rn emanation efficiency [1]. The mobility of ^{222}Rn is mainly influenced by diffusion or by transport processes caused by the motion of gaseous or liquid phases [2, 3]. Due to the relatively short half-life, the distance of transport of ^{222}Rn is in the range of some metres. The disequilibrium between ^{222}Rn and other uranium series radionuclides is caused by the diffusive escape of ^{222}Rn [3]. Normally, the activity concentration of ^{222}Rn in

groundwater is higher than the activity concentration of other uranium series nuclides [4].

Water from wells dug in soil aquifers usually contains 5-50 Bq /I in soils with low uranium concentrations and 10-100 Bq/I in soil with normal concentrations [5]. Radon is principally a problem in wells drilled in bedrocks that contain average or high concentrations of uranium. Uranium, on the other hand, can be a significant problem in both dug and drilled wells. [6] recommends that the limit of uranium concentration in drinking water should be below 15μg/I.

Studies have established the level of ^{222}Rn absorption in the gastrointestinal tract and subsequent elimination via the lungs. In about an hour, 95% of the initial ^{222}Rn exits through the lungs; therefore, the main health risk from ^{222}Rn is caused directly to the stomach. The National Research Council [7] has estimated that about 30% of the activity concentration of ^{222}Rn in the stomach was integrated in the walls of the stomach. The short-lived progenies of ^{222}Rn (^{218}Po , ^{214}Pb , ^{214}Bi and ^{214}Po) together contribute 7.7% of the effective dose caused by ^{222}Rn , assuming that they are in radioactive equilibrium with ^{222}Rn in water [8, 9]. The exception is when ^{222}Rn gas is aerated from water but ^{222}Rn daughters remain in the water. However, in this case, the dose from short-lived ^{222}Rn progenies in aerated water is still less than 10% of the dose from the ^{222}Rn in the untreated water [10].

Materials and Methods

The study area is Abeokuta, which lies between latitudes $7^{\circ} 5' \text{ N}$ and $7^{\circ} 20' \text{ N}$ and longitudes $3^{\circ} 17' \text{ E}$ to $3^{\circ} 27' \text{ E}$, is a town located in the sub-humid tropical region of South-western Nigeria (Fig. 1). Abeokuta is underlain by basement complex rocks, and the populace depend largely on municipal water supplied from the River Ogun. This source of water supply is, however, not sufficient and does not meet the demand of the populace. This surface water, which is the major source of drinking water in Abeokuta, has a very low output, especially during the dry season when the evaporation rate is high (and precipitation is lower than the annual average). Most of the commercial bottle and sachet water industries also rely on water from the municipal water corporations, thus they (commercial bottle/sachet water industries) are unable to ease the prevailing water scarcity in the area.

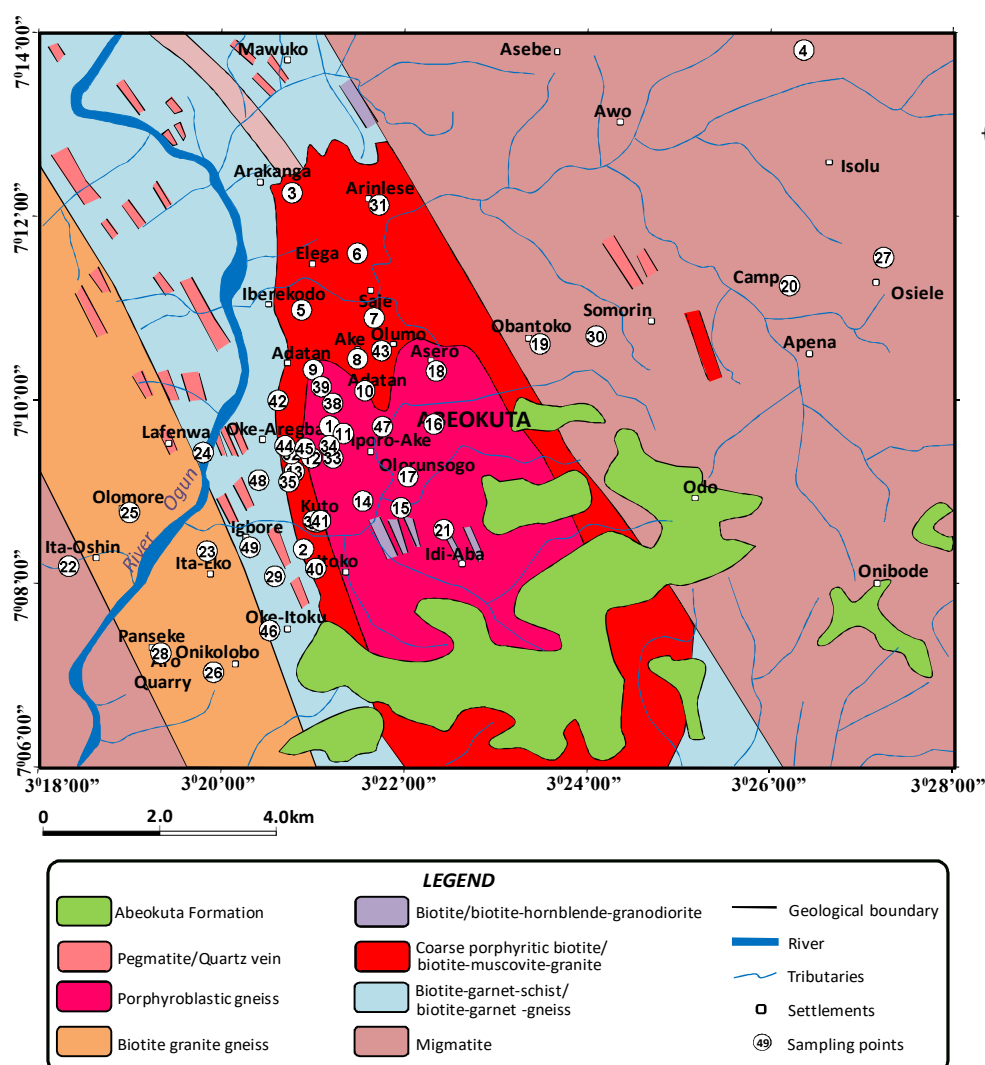
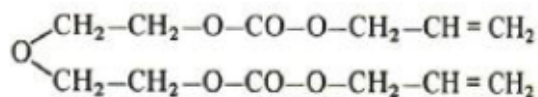


FIG. 1. Geological map of Abeokuta and its environs showing water sampling locations.

Solid State Nuclear Track Detectors (SSNTDs)

Polyallyldiglycol carbonate ($C_{12}H_{18}O_7$), known as CR-39, rigid plastic, with clear, colourless appearance and density of 1.30g.cm^{-3} , has the chemical structure shown below:



It has been used in the manufacture of eyeglass lenses since 1947. It was firstly applied during World War II to coat aircraft fuel tanks for the B-17 bomber aircraft to make them more durable. The abbreviation (CR) stands for Columbia Resin #39, because it was the 39th formula of a thermosetting plastic (Fig. 2) developed by the Columbia Resins project in 1940 [11]. The CR-39 detectors used in this study were obtained from ENEA, institute di Radio protezione, Bologna, Italy. They are rectangular with $500\mu\text{m}$ thickness.

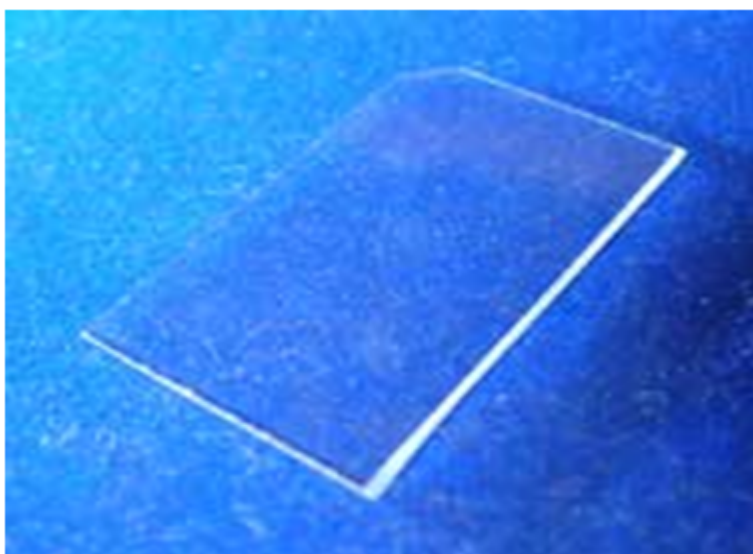


FIG. 2. Photograph of CR-39 solid state nuclear track detector (SSNTD).

LR-115 Films (Type II)

LR-115 films consist of thin films of a special cellulose nitrate coloured deep red and coated on a $100\mu\text{m}$ thick polyester base. Only one side of these films is sensitive. With a needle, it gives white scratches, which must be taken into consideration when used.

LR-115 type films consist of a $100\mu\text{m}$ thick polyester base that is coated with a $12\mu\text{m}$ thin, α -sensitive layer of red coloured cellulose nitrate. Fig. 3 shows the red sensitive layer of the type 2 stripping film (strippable) which must be removed from the base while it is still wet at the conclusion of the washing stage. In the present study, LR-115 detectors (LR-115, Type II) were obtained from DOSIRAD, France. The detectors consist of a $12\mu\text{m}$ active layer of red cellulose nitrate on top of a $100\mu\text{m}$ clear polyester base substrate. It is a circular detector with a diameter of 2cm. It is manufactured by Kodac Pattie, France and marketed by Dosirad, France.

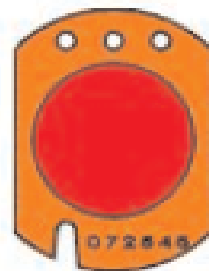


FIG. 3. Photograph of LR-115 film badge type II.

Experimental Method

Exposure of SSNTDs to Water Samples

Each piece of CR-39 and LR-115 detector was placed 9cm above water sample in a hermetically sealed cylindrical plastic container of radius $q=2.75\text{cm}$, as shown in Fig. 4. During the exposure time (40 days), α -particles emitted by radon, thoron and their corresponding daughters bombarded the SSNTD films. This setup and dimensions were based on an earlier optimization described by [12].

All the α -particles emitted by the radionuclides in the radon and thoron series, that reach the LR-115 detector under an angle lower than its critical angle of etching with a residual energy between 1.6 and 4.7 MeV, are registered as bright track-holes. The CR-39 detector is sensitive to all α particles reaching its surface

under an angle smaller than its critical angle of etching (the critical angle for a detector is defined as the angle between the direction of the projectile and the normal to the detector surface, under which no track can be revealed by etching).

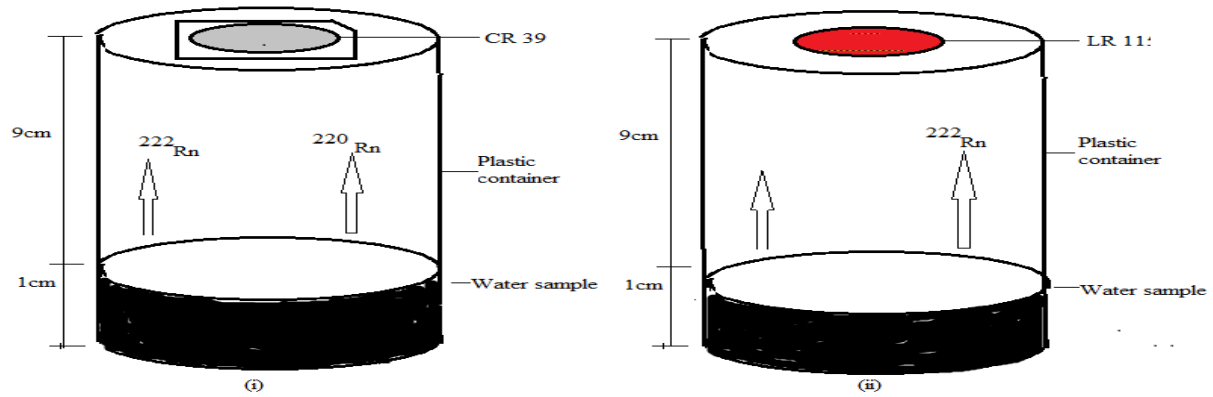


FIG. 4. Setup for measuring radon and thoron concentrations in water comprising two plastic containers (i) with CR-39 and (ii) with LR-115.

Calculation of Radon and Thoron Concentrations

Tracks of alpha-particles, emitted by the nuclei of radon and thoron series, which reached the CR-39 and LR-115 SSNTDs placed at 9 cm above the water sample, were registered. The corresponding track density for each detector was calculated using the equation:

$$\text{Track Density} = \frac{\text{Average number of tracks}}{\text{area of one field of view}} \quad (1)$$

Let dv represent the volume of an elementary cylinder situated between r and $r + dr$ with depth dh inside the gas volume (Fig. 5).

$$dv = 2\pi r dr dh \quad (2)$$

Let dN_i represent the number of α -particles of index i and energy $E_{\alpha i}$ emitted from the radioactive nuclei during the exposure time t_e .

$$dN_i = \lambda_i dn_i t_e \quad (3)$$

where dn_i is the number of α -emitters of index i and radioactive decay constant λ_i in the volume dv .

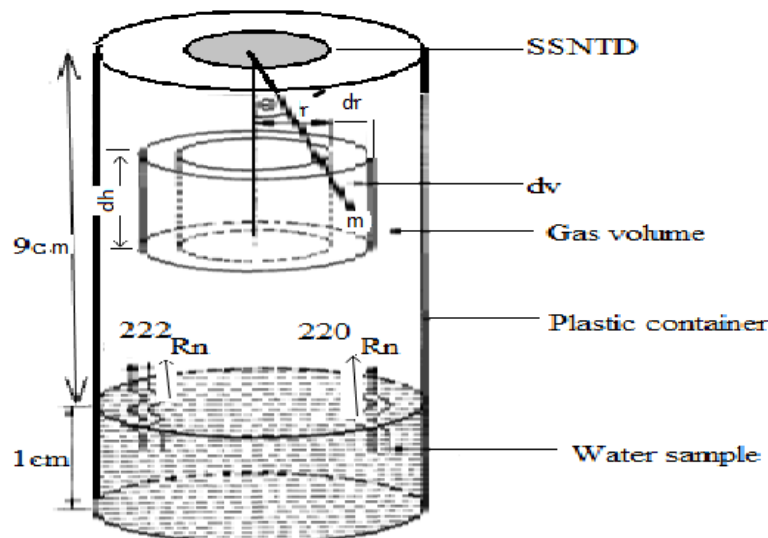


FIG. 5. Arrangement of the SSNTD films placed at a distance of 9 cm above a water sample in a cylindrical plastic container of radius $q = 2$ cm.

Equation (3) may be rewritten as:

$$dN_i = \lambda_i \tilde{\omega}_i dv t_e \quad (4)$$

where $\tilde{\omega}_i$ is the number of α -emitters of index i per unit volume.

Assuming a secular equilibrium between the two radionuclides (^{222}Rn , ^{220}Rn) and their corresponding daughters ($\lambda_u \tilde{\omega}_u = \dots = \lambda_i \tilde{\omega}_i$ and $\lambda_{Th} \tilde{\omega}_{Th} = \dots = \lambda_i \tilde{\omega}_i$), equation (4) becomes:

$$dN_i = \lambda_{222} \tilde{\omega}_{222} 2\pi r dr dh t_e \quad (5)$$

for the ^{222}Rn family and

$$dN_i = \lambda_{220} \tilde{\omega}_{220} 2\pi r dr dh t_e \quad (6)$$

for the thoron family, where λ_{222} and λ_{220} are the ^{222}Rn and ^{220}Rn decay constants, respectively.

Let P_i^{CR} represent the probability for an α -particle of energy $E_{\alpha i}$ and index i emitted at a distance x from the detector to reach and be registered on the CR-39 SSNTD [13]:

$$P_i^{CR} = \int_0^{R_i} [1 - \cos \theta_c(x)] dx \quad (7)$$

where R_i is the range of the α -particle of energy $E_{\alpha i}$ and index i in gas volume and θ_c is the critical angle of etching of the CR-39 SSNTD.

The number of α -particles emitted from the radon family nuclei, in the volume dv , which reach and are registered on the CR-39 SSNTD, is given by:

$$dN^{CR} (^{222}\text{Rn}) = \left\{ \lambda_{222} \tilde{\omega}_{222} t_e 2\pi r dr \sum_{i=1}^3 k_i P_i^{CR} dh \right\} \quad (8)$$

where k_i is the branching ratio in %.

Consequently, the total number of α -particles emitted from the radon family nuclei in the whole sample which are registered on the CR-39 SSNTD is given by:

$$N_T^{CR} (^{222}\text{Rn}) = \left\{ A_C^{222} (Bq \cdot cm^{-3}) \pi q^2 t_e \sum_{i=1}^3 k_i P_i^{CR} R_i \right\} \quad (9)$$

where q is the radius of the plastic container in cm (Fig. 6), k_i is the branching ratio in %, $A_C^{222} (Bq \cdot cm^{-3})$ is the radon activity per unit volume.

The corresponding density of tracks (tracks $cm^{-2} \cdot s^{-1}$) registered on the CR-39 SSNTD due to the α -particles of the radon group is:

$$\rho_T^{CR} (^{222}\text{Rn}) = A_C^{222} (Bq \cdot cm^{-3}) \sum_{i=1}^3 k_i P_i^{CR} R_i \quad (10)$$

Similarly, the density of tracks (tracks $cm^{-2} \cdot s^{-1}$) due to the α -particles of the thoron family, registered on the CR-39 SSNTD is:

$$\rho_T^{CR} (^{220}\text{Rn}) = A_C^{220} (Bq \cdot cm^{-3}) \sum_{i=1}^4 k_i P_i^{CR} R_i \quad (11)$$

where $A_C^{220} (Bq \cdot cm^{-3})$ is the thoron activity per unit volume.

The global density of tracks due to the α -particles of the radon and thoron series, registered on the CR-39 SSNTD is then:

$$\rho_G^{CR} = A_C^{222} (Bq \cdot cm^{-3}) \left[\sum_{i=1}^3 k_i P_i^{CR} R_i + \sum_{i=1}^4 k_i P_i^{CR} R_i \right] \quad (12)$$

Let P^{LR} represent the probability for an emitted α -particle to reach and be registered on the LR-115 SSNTD.

$$P^{LR} = \int_{R_{min}}^{R_{max}} [1 - \cos \theta_c^1(x)] dx \quad (13)$$

where θ_c^1 is the critical angle of etching, which depends on the residual LR-115 SSNTD thickness.

R_{min} and R_{max} are the α -particle ranges in the sample which correspond to the lower and upper ends of the energy window and depend on the residual thickness of the LR-115 SSNTD [14].

Consequently, the density of tracks (tracks $cm^{-2} \cdot s^{-1}$), due to the α -particles of the radon group, registered on the LR-115 SSNTD is given by:

$$\rho_T^{LR} (^{222}\text{Rn}) = A_C^{220} (Bq \cdot cm^{-3}) 3 P^{LR} \Delta R \quad (14)$$

where $\Delta R = R_{max} - R_{min}$.

Similarly, the density of tracks (track $cm^{-2} \cdot s^{-1}$) due to the α -particles of the thoron group, registered on the LR-115 SSNTD is:

$$\rho_T^{LR} (^{220}\text{Rn}) = A_C^{220} (Bq \cdot cm^{-3}) 4 P^{LR} \Delta R \quad (15)$$

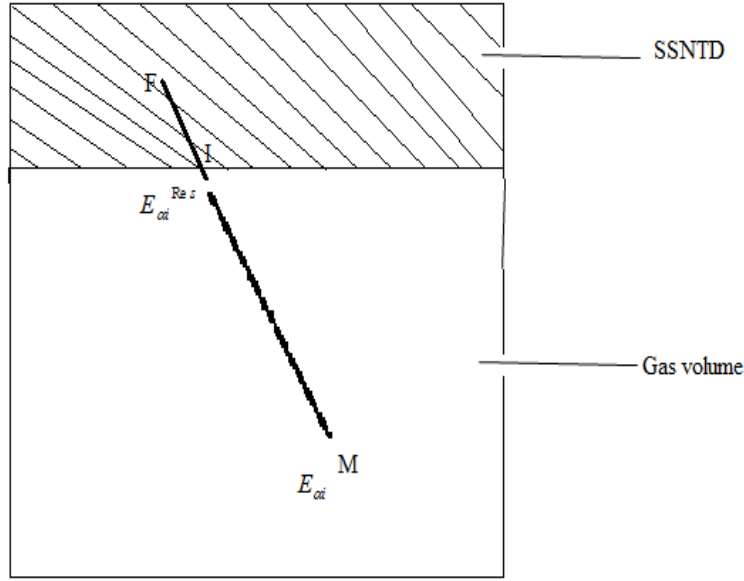


FIG. 6. Diagram illustrating primary trajectory of an α -particle inside the gas volume (MI = X) and SSNTD (IF = RD). $E_{\alpha i}$ is the initial energy of the α -particle and $E_{\alpha i}^{\text{Res}}$ is its residual energy on reaching point I.

The global density of tracks (tracks $\text{cm}^{-2} \cdot \text{s}^{-1}$) due to the α -particles of the radon and thoron series, registered on the LR-115 SSNTD is equal to:

$$\rho_G^{LR} = A_c^{222} (\text{Bq} \cdot \text{cm}^{-3}) (3P^{LR} \Delta R + 4P^{LR} \Delta R \frac{A_c^{220}}{A_c^{222}}) \quad (16)$$

Combining equations (12) and (16), we obtained the following relationship between track densities and thoron to radon ratio.

$$\frac{\rho_G^{CR}}{\rho_G^{LR}} = \frac{\sum_{i=1}^3 k_i P_i^{CR} R_i + \frac{A_c^{220}}{A_c^{222}} \sum_{i=1}^4 k_i P_i^{CR} R_i}{3P^{LR} \Delta R + 4P^{LR} \Delta R \frac{A_c^{220}}{A_c^{222}}}. \quad (17)$$

By measuring ρ_G^{CR} and ρ_G^{LR} and knowing the values of P_i^{CR} and P^{LR} from Tables 1 and 2,

respectively, one can determine the $\frac{A_c^{220}}{A_c^{222}}$ ratio using Eq. 17 and consequently the thoron A_c^{220} and radon A_c^{222} activities of the studied water samples by substituting Eq. 18 into Eq. 16.

From Eq. 17, one can determine the $\frac{A_c^{220}}{A_c^{222}}$ ratio as follows,

$$\frac{A_c^{220}}{A_c^{222}} = \frac{\sum_{i=1}^3 K_i P_i^{CR} R_i - 3P^{LR} \Delta R \frac{\rho_G^{CR}}{\rho_G^{LR}}}{4P^{LR} \Delta R \frac{\rho_G^{CR}}{\rho_G^{LR}} - \sum_{i=1}^4 K_i P_i^{CR} R_i}. \quad (18)$$

TABLE 1. Data obtained for the probability (P_i^{CR}) for radon group α -particles and thoron group α -particles to be registered on the CR-39 SSNTD for the gas volume of the α -particles of energy $E_{\alpha i}$ and index i in the gas volume [12].

Nuclides	$E_{\alpha i}$ (MeV)	R_i (cm)	$P_i^{CR} \times 10^{-3}$	k_j
Radon group α -particles				
^{222}Rn	5.49	3.90	2.871	1
^{218}Po	6.00	4.65	3.383	1
^{214}Po	7.68	6.65	4.440	1
Thoron group α -particles				
^{220}Rn	6.28	4.80	3.391	1
^{216}Po	6.78	5.45	3.433	1
^{212}Bi	6.08	4.75	3.527	0.36
^{212}Po	8.78	8.36	5.711	0.64

TABLE 2. Values of the probability (PLR) for the α -particles of the radon and thoron groups to be registered on the LR-115 SSNTD for different residual thicknesses for (LR-115 films) for the gas volume of the water samples. R_{\min} and R_{\max} are the α -particle ranges in the gas volume which correspond to the lower and upper ends of the energy window [12].

Residual thickness (μm)	R_{\min} (cm)	R_{\max} (cm)	$p^{\text{LR}} \times 10^{-3}$
3	0.46	3.83	203.299
4	0.61	3.52	11.302
5	0.80	3.44	4.329
6	0.98	2.71	1.536
7	1.07	2.66	1.405
8	1.29	2.53	1.336
9	1.42	2.31	0.267
10	1.60	2.02	0.191

The activity concentrations in groundwater samples ranged from 3050.49 to 90798.69 Bq/m³ and from 660.76 to 57181.68 Bq/m³ for ²²²Rn and ²²⁰Rn, respectively. The frequency distribution analyses are shown on Figs. 7 and 8 for track densities on the CR-39 and LR-115

detectors, respectively. The error on track density counting is smaller than 7% for the samples studied.

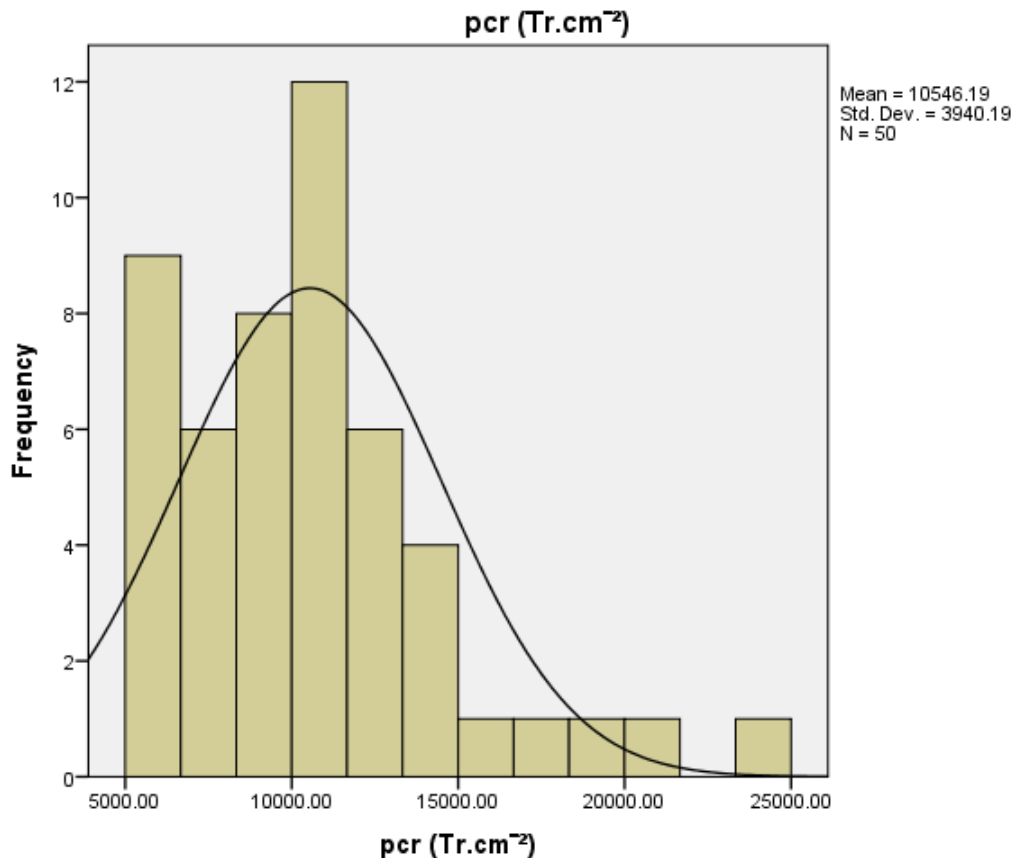


FIG. 7. Frequency curve for track density of radon in CR-39.

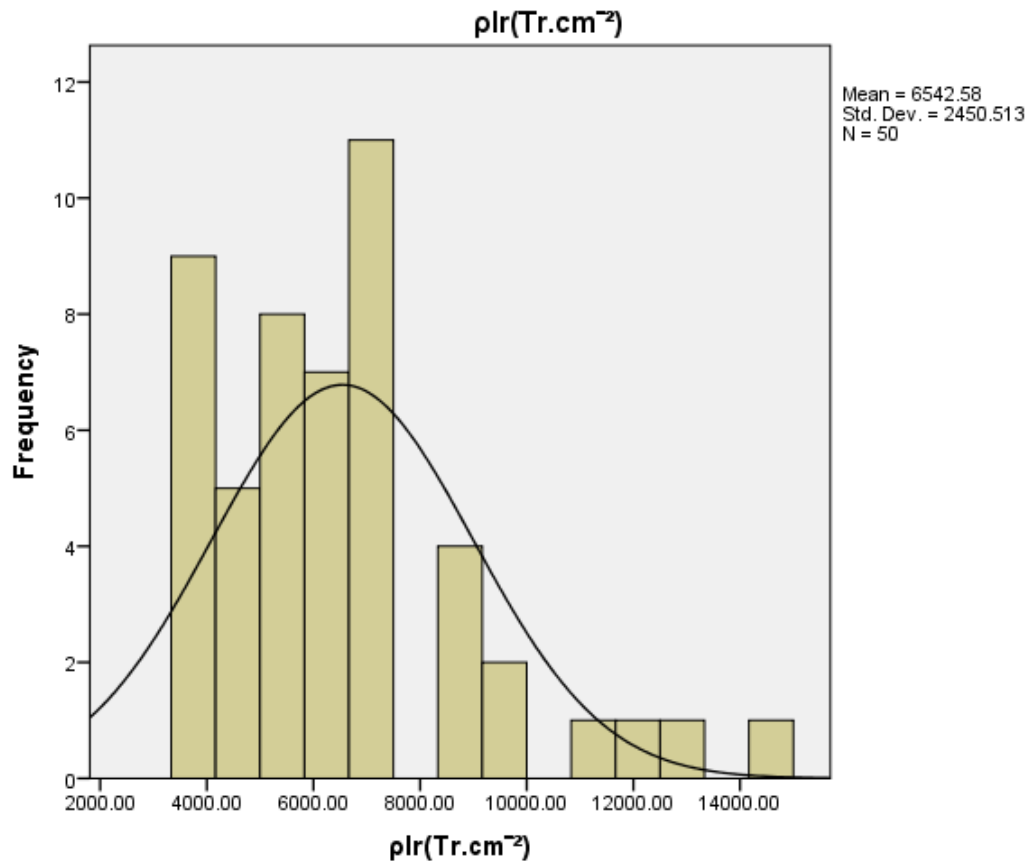


FIG. 8. Frequency curve for track density of radon in LR-115.

Calculation of Annual Effective Dose

The annual effective doses due to the intake of radon were calculated from the mean activity concentration using the following equation [15]:

$$E_{Rn} = DF_{Rn} \cdot I_w \cdot A_{Rn} \quad (19)$$

where DF_{Rn} is the effective dose per unit intake of radon in water, taken as 10^{-8} Sv/Bq for adults and 2×10^{-8} Sv/Bq for children from UNSCEAR 1993 report [16] and I_w is the water consumption rate, taken to be 2 litres per day from WHO report [17].

Results and Discussion

The values of the annual effective dose per person caused by different drinking groundwater samples in this study are presented in Table 3. The estimated total annual effective dose for children ranged from 71 μ Sv/y from drinking water of sample code GW 031 to 1326 μ Sv/y from drinking water of sample code GW006, with an average of (273) μ Sv/y, while for adults the total annual effective dose ranged from 35 μ Sv/y from drinking water of sample code

GW031 to 663 μ Sv/y from drinking water of sample code GW006, with an average (136) μ Sv/y.

It is also noted from the results that among the 50 samples analyzed, the water sample from Panseke area recorded the highest ^{222}Rn concentration and the corresponding annual effective dose among all the other water samples.

More than 90% of the water samples resulted in annual effective doses for children above the 0.1mSv/y safe limit and 80% of the annual effective doses for adults were found to be above the safe limit of 0.1 mSv/y recommended by World Health Organization [18] and EU Council [8].

The results obtained showed that radon in drinking water could constitute a radiological concern for people using the areas and further research should be conducted to determine the prevalence and whether remediation action would be required.

TABLE 3. Results of annual effective dose in groundwater samples

SAMPLE CODE	LATITUDE	LONGITUDE	$^{222}\text{A}(\text{Bq.m}^{-3})$	$\pm\text{Error}$	$^{222}\text{A}(\text{Bq.L}^{-1})$	Annual effective dose ingestion ($\mu\text{Sv/year}$) for children	Annual effective dose ingestion ($\mu\text{Sv/year}$) for adults
GW 001	7.1743	3.35787	15692.01	± 864.00	15.69	229.1	114.55
GW002	7.13982	3.34797	20044.33	± 1718.00	20.04	292.65	146.32
GW003	7.16213	3.35272	38315.87	± 977.00	38.32	559.41	279.71
GW004	7.23027	3.43965	40342.13	± 1829.00	40.34	589	294.5
GW005	7.18316	3.3476	49679.72	± 1766.00	49.68	725.32	362.66
GW006	7.12097	3.32184	90798.69	± 3838.00	90.80	1325.66	662.83
GW007	7.18172	3.36091	46721.01	± 823.00	46.72	682.13	341.06
GW008	7.16676	3.34329	51458.57	± 1786.00	51.46	751.3	375.65
GW009	7.17234	3.34977	78330.88	± 2003.00	78.33	1143.63	571.82
GW010	7.16853	3.3592	41390.51	± 2437.00	41.39	604.3	302.15
GW011	7.15634	3.35335	15789.83	± 465.00	15.79	230.53	115.27
GW012	7.15638	3.34943	27532.87	± 444.00	27.53	401.98	200.99
GW013	7.19343	3.35785	41049.10	± 2240.00	41.05	599.32	299.66
GW014	7.13489	3.34268	58084.87	± 4081.00	58.08	848.04	424.02
GW015	7.1473	3.3658	46225.88	± 1181.00	46.23	674.9	337.45
GW016	7.16248	3.37185	39018.71	± 1250.00	39.02	569.67	284.84
GW017	7.15296	3.36709	12140.36	± 556.00	12.14	177.25	88.62
GW018	7.1721	3.37229	27954.36	± 1125.00	27.95	408.13	204.07
GW019	7.177	3.39131	46525.38	± 1238.00	46.53	679.27	339.64
GW020	7.18759	3.437	44844.35	± 827.00	44.84	654.73	327.36
GW021	7.14334	3.37364	23400.36	± 953.00	23.40	341.65	170.82
GW022	7.13674	3.30494	50278.71	± 2509.00	50.28	734.07	367.03
GW023	7.13946	3.33029	22024.86	± 1618.00	22.02	321.56	160.78
GW024	7.15733	3.32958	23498.17	± 418.00	23.50	343.07	171.54
GW025	7.14647	3.3161	16095.37	± 693.00	16.10	234.99	117.5

SAMPLE CODE	LATITUDE	LONGITUDE	$^{222}\text{A}(\text{Bq.m}^{-3})$	$\pm\text{Error}$	$^{222}\text{A}(\text{Bq.L}^{-1})$	Annual effective dose ingestion ($\mu\text{Sv/year}$) for children	Annual effective dose ingestion ($\mu\text{Sv/year}$) for adults
GW026	7.11752	3.33147	54331.54	± 1353.00	54.33	793.24	396.62
GW027	7.19266	3.45426	50376.53	± 1076.00	50.38	735.5	367.75
GW028	7.15388	3.34628	52552.69	± 3229.00	52.55	767.27	383.63
GW029	7.15204	3.34529	13418.03	± 784.00	13.42	195.9	97.95
GW030	7.17844	3.40159	20479.45	± 416.00	20.48	299	149.5
GW031	7.2044	3.34587	4829.33	± 279.00	4.83	70.51	35.25
GW032	7.2022	3.36179	48597.68	± 2077.00	48.60	709.53	354.76
GW033	7.15711	3.34572	33486.53	± 2331.00	33.49	488.9	244.45
GW034	7.16079	3.35528	22024.86	± 2163.00	22.02	321.56	160.78
GW035	7.15854	3.3527	36237.52	± 1352.00	36.24	529.07	264.53
GW036	7.15233	3.33974	23803.71	± 1675.00	23.80	347.53	173.77
GW037	7.14853	3.35883	8582.66	± 822.00	8.58	125.31	62.65
GW038	7.14492	3.34972	25778.19	± 1712.00	25.78	376.36	188.18
GW039	7.16625	3.353303	32985.36	± 1154.00	32.99	481.59	240.79
GW040	7.16927	3.35122	27954.36	± 2203.00	27.95	408.13	204.07
GW041	7.13633	3.35022	35161.53	± 2809.00	35.16	513.36	256.68
GW042	7.145	3.3511	20044.33	± 1412.00	20.04	292.65	146.32
GW043	7.14471	3.35035	12335.99	± 414.00	12.34	180.11	90.05
GW044	7.17578	3.36225	56306.02	± 1463.00	56.31	822.07	411.03
GW045	7.15855	3.34456	20723.02	± 691.00	20.72	302.56	151.28
GW046	7.15809	3.34825	18257.52	± 1636.00	18.26	266.56	133.28
GW047	7.12508	3.34173	27654.86	± 1784.00	27.65	403.76	201.88
GW048	7.16201	3.36243	21523.69	± 1023.00	21.52	314.25	157.12
d.wtater			3050.49	± 111.00	3.05	44.54	22.27
GW050	7.14017	3.33817	22024.86	± 1035.00	22.02	321.56	160.78

Conclusion

Two types of Solid State Nuclear Track Detector (SSNTD); i.e., CR-39 and LR-115 type II, were used in this study to evaluate the concentrations of ^{222}Rn and ^{220}Rn in groundwater samples from different locations in Abeokuta. This technique has the advantages of being simple, accurate, inexpensive and non-destructive and does not need the use of any standard for its calibration. The results showed a range of ^{222}Rn concentrations between 3050.49 and 90798.69 Bq/m³. Generally, there was a higher concentration of ^{222}Rn in the well-water samples compared to ^{220}Rn , although there were exceptional cases where ^{220}Rn concentrations were higher than those of ^{222}Rn . A well in Panseke area recorded the highest ^{222}Rn concentration (90798.69 Bq/m³). Other areas with high radon concentration values are Sapon (52552.69 Bq/m³), Okearegba (56306.02 Bq/m³) and Ake (38315.87 Bq/m³). The results of ^{222}Rn concentrations agree well with those obtained earlier by [19] using RAD7 connected to a bubbling kit to degas radon from water samples.

Going by the results of this study and the strong dependence of the populace on groundwater, it is concluded that water consumption may be a relevant radiological exposure pathway among some of the inhabitants of Abeokuta. It is therefore pertinent to recommend that more consideration should be given to further study of radon in indoor air and drinking water in different parts of Abeokuta with a view to ascertain prevalence and remediation required. The results of this study revealed that many of the groundwater samples in the study area have high levels of ^{222}Rn . Considering that a large population of Nigerians derive water for drinking and other domestic uses from underground sources, it is recommended that study of radon concentration in water and indoor air should be promoted among researchers, e.g. by giving grants for large-scale regional or national surveys. The SSNTD method for radon studies and for measurement of other natural radionuclides should be further encouraged.

References

- [1] Veeger, A.I. and Ruderman, N.C., *Ground Water*, 36(4) (1998) 596.
- [2] Juntunen, R., "Uranium and Radon in Wells Drilled into Bedrock in Southern Finland", Report of Investigation, Helsinki: Geological Survey of Finland, 98 (1991).
- [3] Salih, I., Bäckström, M., Karlsson, S., Lund, E. and Pettersson, H.B.L., *Applied Radiation and Isotopes*, 60(1) (2004) 99.
- [4] Salonen, L., *Future Groundwater Resources at Risk: IAHS Publ.*, 222 (1994) 71.
- [5] Akerblom, G. and Lindgren, J., *European Geologist*, 5 (1997) 13.
- [6] WHO, "Guidelines for Drinking Water Quality". Recommendations, Vol. 1, 3rd Edition. (World Health Organization, Geneva, 2004).
- [7] National Research Council, "Risk Assessment of Radon in Drinking Water", (Washington D.C.: National Academy Press, 1999).
- [8] European Commission, *Official Journal of the European Commission*, Official J L 330 (1998).
- [9] Kendall, G.M., Fell, T.P. and Phipps, A.W., *Radiological Protection Bulletin*, 97 (1988) 7.
- [10] Swedjemark, G.A. and Linden, A.H., *Radiation Protection Dosimetry*, 80(4) (1998) 405.
- [11] Fleischer, R.L., Price, P.B. and Walker, R.K., "Nuclear Tracks in Solids, Principles and Applications", Berkeley, (California: University of California, 1975).
- [12] Misdaq, M.A. and Satif, C., *J. Radioanal. Nucl. Chem.*, 207 (1996) 107.
- [13] Misdaq, M.A., Gilane, M., Ouguidu, J. and Outeqabit, K., *Radiat. Prot. Dosim.*, 142 (2000) 136.
- [14] Somogyi, G., 15th Int. Symp. on Autoradiography, Matarfured, Hungary, 20-23 Oct., (1986).

- [15] IAEA, "Water for People, Water for Life", UN World Water Development Report, 2001.
- [16] United Nations Scientific Committee on the Effects of Atomic Radiation, UNSCEAR. "Sources and Effects of Ionizing Radiation", UNSCEAR Report to the General Assembly with Scientific Annexes, United Nations, New York, (1993).
- [17] World Health Organization, WHO, "Guidelines for Drinking Water Quality", Vol.1, 2nd ed. (WHO, Geneva, 1993).
- [18] WHO, "Guidelines for Drinking Water Quality", 3rd Ed., (WHO, Geneva, 2008).
- [19] Oni, O.M., Oladapo, O.O., Amuda, D.B, Oni, E.A., Adelodun, A.O., Adewale, K.Y. and Fasina, M.O., Nigerian Journal of Physics, 25(1) (2014).

Electromagnetic Transmission from a Dielectric Loaded Resistive Cylindrical Pipe

M. S. Bawa'aneh, A. M. Al-Khateeb and N. Laham

Department of Physics, Yarmouk University, Irbid, Jordan.

Received on: 24/5/2017;

Accepted on: 9/8/2017

Abstract: We obtained analytically closed form expressions for longitudinal electric impedance and transmission coefficient of a dielectric loaded resistive cylindrical pipe of finite thickness. These expressions are valid for an axial current in a form of a point source moving parallel to the pipe axis with an offset a . The resistive-wall impedance and the transmission coefficient have been numerically visualized for some representative machine parameters. For wall thicknesses less than the skin penetration depth, the wall becomes transparent for the excited electromagnetic fields. Very good shielding for standard operation can be achieved by thin metallic walls of thicknesses of the order of few skin penetration depths. Effects of the dielectric constant and thickness on the transmission coefficient are found to be negligibly small, while the presence of the dielectric leads to a suppression of resistive-wall impedance for large thicknesses of the dielectric layer.

Keywords: Cylindrical pipe, Electrical impedance, Transmission coefficient, Wave guides.

Introduction

Axial currents, like a beam of charged particles or an RF-source, may excite electromagnetic fields in its environment and periodic excitations can occur depending on the coupling of the beam to its environment at a particular frequency.

For pipe walls that are not perfectly conducting, electromagnetic fields excited by the beam penetrate partially into the pipe wall with a penetration depth given by the skin depth $\delta_s(\omega)$. Image currents induced in the wall lead to heating when the wall conductivity is not infinite. In the literature of electric impedances [1, 2], one finds different expressions for the corresponding resistive-wall impedance with different ranges of validity. When the skin depth is larger than the wall thickness, the beam induces electromagnetic fields that can penetrate through the wall. In such cases, the impedance depends on the structures outside the pipe. In this situation, in addition to the impedance, detailed calculations of the shielding effectiveness of the

pipe are necessary in order to estimate the currents that could be induced in hardware components behind the pipe.

The well known ability of a thin layer of thickness d (less than the skin depth δ_s) to shield electromagnetic fields produced by a particle beam was considered in Ref. [3]. Because of the relevance of the issue for the design of high-current ring machines, it is important to have closed form expressions for the resistive wall impedance and for the shielding effectiveness covering the relevant range of frequencies, beam energies and wall thicknesses. Krinski et al. [4] derived asymptotic formulae for the impedance of a cylindrical metal tube of a specific radius, length and conductivity attached at each end to perfect conductors of semi-infinite length and computed the short-range wake field. Metral et al. [5] derived a formula for the resistive wall impedances of an infinitely long cylindrical beam pipe. They found that the resistive impedance is about two orders of magnitude

lower at this frequency, which is explained by the fact that the skin depth is much larger than the beam pipe radius. Zhilichev [7] derived an analytical form for the impedance of short conductors in the form of a convergent series and applied it to the calculation of the impedance of a resistive cylinder between two superconductors. Biancacci et al. [8] studied the effect of different material conductivities, finite length and particle beam velocity on the coupling impedance of azimuthally symmetric cavities of finite length loaded with a toroidal slab of lossy dielectric using the method of mode matching technique for an azimuthally uniform structure of finite length.

In the present work, we consider the problem of the interaction between a dielectric-lined resistive cylindrical pipe and a point source moving off-axis with an offset a (an infinitesimally thin ring with radius a). Such a scheme was used in investigating dielectric wake-field accelerators, in which charged particle beams excite electromagnetic wake fields known as Cerenkov radiation [9, 10, 11]. In the frequency domain, we are interested in evaluating the excited electromagnetic fields in such a dielectric-lined cylindrical pipe and then in finding the corresponding resistive-wall impedance and transmission coefficient for our problem.

The paper is organized as follows. In the next section, we present the model equations for the pipe structure under consideration. Then, in the following two sections, we use the exact field matching technique to calculate the excited electromagnetic fields and the corresponding longitudinal electric impedance and transmission coefficient. In the last section, the analytical expressions for resistive-wall impedance and transmission will be numerically visualized and main conclusions will be presented.

Model Equations

The general wave equations satisfied by the electric and magnetic fields \vec{E} and \vec{B} in a linear medium of conductivity S , permittivity f and permeability μ are obtained from Faraday's and Ampere's laws [12, 13, 14]; namely,

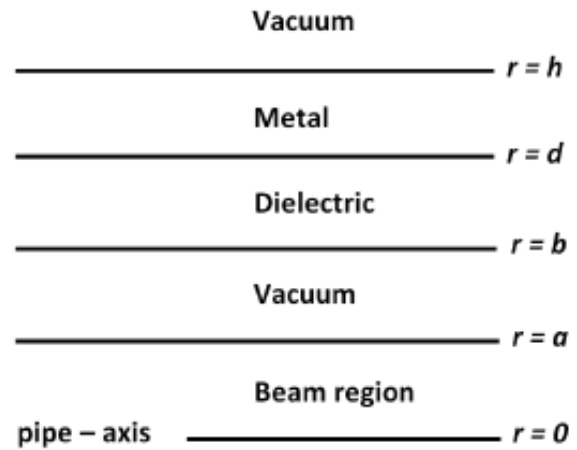


FIG. 1. Schematic of the problem geometry.

$$\nabla^2 \vec{B}(\vec{r}, t) - \mu\epsilon \frac{\partial^2 \vec{B}(\vec{r}, t)}{\partial t^2} - \mu S \frac{\partial \vec{B}(\vec{r}, t)}{\partial t} = -\mu \vec{\nabla} \times \vec{j}(\vec{r}, t), \quad (1)$$

$$\nabla^2 \vec{E}(\vec{r}, t) - \mu\epsilon \frac{\partial^2 \vec{E}(\vec{r}, t)}{\partial t^2} - \mu S \frac{\partial \vec{E}(\vec{r}, t)}{\partial t} = \mu \frac{\partial \vec{j}(\vec{r}, t)}{\partial t} + \frac{\vec{\nabla} \rho(\vec{r}, t)}{\epsilon}, \quad (2)$$

where ρ and \vec{j} are the beam charge and current densities, respectively, which obey the following continuity equation:

$$\frac{\partial \rho(\vec{r}, t)}{\partial t} + \vec{\nabla} \cdot \vec{j}(\vec{r}, t) = 0. \quad (3)$$

The axial current is modeled as a point charge q_0 moving down a cylindrical pipe with an offset a in the $\theta_0 = 0$ direction with a constant longitudinal velocity $\vec{v} = \beta_0 c \hat{z}$. In decomposing the corresponding charge and current densities in

terms of multipole moments, the lowest monopole moment is:

$$\rho(\vec{r}, t) = \frac{q_0}{2\pi a} \delta(a - r) \delta(z - \beta_0 ct) , \quad (4)$$

$$\vec{j}(\vec{r}, t) = \frac{q_0}{2\pi a} \delta(a - r) \delta(z - \beta_0 ct) \beta_0 c \hat{z} . \quad (5)$$

This monopole source has an axially symmetric transverse charge distribution and it represents an infinitesimally thin ring with radius a . The beam is moving in a cylindrical pipe of radius b , enclosed from inside to outside, respectively, by a dielectric of thickness t_d and

dielectric constant κ_d , a conducting layer of conductivity S and thickness t_c , then vacuum outside, as shown in Fig 1.

Time Fourier-transformed charge and current densities in Eqs. (4) and (5) are:

$$\rho(r, z, \omega) = \frac{q_0}{2\pi a \beta_0 c} \delta(a - r) e^{ik_z z} , \quad (6)$$

$$j(r, z, \omega) = \frac{q_0}{2\pi a} \delta(a - r) e^{ik_z z} , \quad (7)$$

where $\omega = k_z \beta_0 c$ has been used and k_z is the wave number in the direction of beam propagation.

Due to the symmetry of the source under consideration, only transverse magnetic (TM) cylindrical waveguide modes couple to the propagating beam such that $B_z = 0$. All other field components are obtained from $E_z(r, z, \omega)$ using Maxwell's equations, where $E_\theta(r, z, \omega)$ and $B_r(r, z, \omega)$ vanish identically because of the axial symmetry of the beam.

We assume normal mode solution for the time Fourier-transformed electric field such that $E_z(r, z, \omega) = E_z(r, \omega) e^{ik_z z}$. This is in agreement with the source terms in Eqs. (6) and (7). Upon Fourier transforming Eq. (2) in time and making use of $\rho(r, z, \omega)$ and $j(r, z, \omega)$ of Eqs. (6) and (7), respectively, we obtain the following equations for the longitudinal electric field component E_z within each region of interest:

$$\left[\frac{d^2}{dr^2} + \frac{1}{r} \frac{d}{dr} - \sigma_0^2 \right] E_z^{(1)}(r, \omega) = i \frac{q_0}{2\pi a \epsilon_0 \gamma_0^2 \beta_0 c} \delta(a - r) , \quad 0 \leq r \leq a \quad (8)$$

$$\left[\frac{d^2}{dr^2} + \frac{1}{r} \frac{d}{dr} - \sigma_0^2 \right] E_z^{(2)}(r, \omega) = 0 , \quad a \leq r \leq b \quad (9)$$

$$\left[\frac{d^2}{dr^2} + \frac{1}{r} \frac{d}{dr} - \sigma_d^2 \right] E_z^{(3)}(r, \omega) = 0 , \quad b \leq r \leq d = b + t_d \quad (10)$$

$$\left[\frac{d^2}{dr^2} + \frac{1}{r} \frac{d}{dr} - \sigma_c^2 \right] E_z^{(4)}(r, \omega) = 0 , \quad d \leq r \leq h = d + t_c \quad (11)$$

$$\left[\frac{d^2}{dr^2} + \frac{1}{r} \frac{d}{dr} - \sigma_0^2 \right] E_z^{(5)}(r, \omega) = 0 , \quad h \leq r < \infty \quad (12)$$

where the propagation wave numbers σ_0 , σ_d and σ_c are given by the following expressions:

$$\sigma_0^2 = \frac{k_z^2}{\gamma_0^2} , \quad \sigma_d^2 = k_z^2 (1 - \beta_0^2 \kappa_d) , \quad \sigma_c^2 = \sigma_0^2 \left(1 + i \frac{\omega \gamma_0^2 \mu_0 S}{k_z^2} \right) , \quad \gamma_0^{-2} = 1 - \beta_0^2 . \quad (13)$$

Since the structure under consideration supports only transverse magnetic modes due to azimuthal symmetry of the source, the electromagnetic field components $B_\theta(r, z, \omega)$ and $E_r(r, z, \omega)$ are non-vanishing and are needed for

matching the solutions at the different interfaces involved in the problem. These fields are obtained from $E_z(r, z, \omega)$ via Maxwell equations as follows:

$$E_r(r, z, \omega) = -i \frac{k_z}{\sigma_\alpha^2} \frac{\partial E_z(r, z, \omega)}{\partial r}, \quad (14)$$

$$B_\theta(r, z, \omega) = \left(\frac{\beta}{c} + i \frac{\mu_0 \beta c S}{\omega} \right) E_r(r, z, \omega) \quad (15)$$

where σ_α stands for σ_0 , σ_d and σ_c .

Excited Electromagnetic Fields

In this section, we solve the wave equation for E_z in each region and then find the associated integration constants using exact field matching. For TM modes in azimuthally symmetric pipe structures, we only solve for the z -component of

the electric field in the five regions involved in the problem. The general solution for the electric field E_z in each region is:

$$E_z(r, \omega) = \begin{cases} A_1 I_0(\sigma_0 r) & 0 \leq r \leq a \\ A_2 I_0(\sigma_0 r) + A_3 K_0(\sigma_0 r) & a \leq r \leq b \\ A_4 I_0(\sigma_d r) + A_5 K_0(\sigma_d r) & b \leq r \leq d = b + t_d \\ A_6 I_0(\sigma_c r) + A_7 K_0(\sigma_c r) & d \leq r \leq h = b + t_c \\ A_8 K_0(\sigma_0 r) & h \leq r < \infty, \end{cases} \quad (16)$$

where I_0 and K_0 are the zero-order modified Bessel functions of first and second kinds, respectively. In addition to the finiteness of E_z as $r \rightarrow 0$ and $r \rightarrow \infty$, we still have eight arbitrary constants and therefore eight boundary

conditions are needed. Integrating the differential equation for E_z from $r = a - \delta$ to $r = a + \delta$ for vanishingly small δ , we obtain the following boundary condition for the discontinuity of $\partial E_z / \partial r$ at $r = a$:

$$(E'_z{}^{r \geq a} - E'_z{}^{r \leq a}) \big|_{r=a} = i \frac{1}{\epsilon_0 \gamma_0 \beta c} \frac{q_0}{2\pi a} \equiv i q_0 f_0, \quad (17)$$

where E'_z is the derivative of E_z with respect to $\sigma_0 r$. We also use the continuity of E_z at $r = a$, the continuity of E_z and B_θ at $r = b$, $r = d$ and $r = h$.

Applying the above mentioned eight boundary conditions, we obtain the following eight algebraic equations:

$$A_1 I_0(\sigma_0 a) = A_2 I_0(\sigma_0 a) + A_3 K_0(\sigma_0 a), \quad (18)$$

$$A_2 I_1(\sigma_0 a) - A_3 K_1(\sigma_0 a) - A_1 I_1(\sigma_0 a) = i \frac{1}{\epsilon_0 \gamma_0 \beta c} \frac{q_0}{2\pi a} \equiv i q_0 f_0, \quad (19)$$

$$A_2 I_0(\sigma_0 b) + A_3 K_0(\sigma_0 b) = A_4 I_0(\sigma_d b) + A_5 K_0(\sigma_d b), \quad (20)$$

$$A_2 I_1(\sigma_0 b) - A_3 K_1(\sigma_0 b) = \eta_{dv} [A_4 I_1(\sigma_d b) - A_5 K_1(\sigma_d b)], \quad (21)$$

$$A_4 I_0(\sigma_d d) + A_5 K_0(\sigma_d d) = A_6 I_0(\sigma_c d) + A_7 K_0(\sigma_c d), \quad (22)$$

$$A_4 I_1(\sigma_d d) - A_5 K_1(\sigma_d d) = \eta_{cd} [A_6 I_1(\sigma_c d) - A_7 K_1(\sigma_c d)], \quad (23)$$

$$A_6 I_0(\sigma_c h) + A_7 K_0(\sigma_c h) = A_8 K_0(\sigma_0 h), \quad (24)$$

$$\eta_{cv} [A_6 I_1(\sigma_c h) - A_7 K_1(\sigma_c h)] = -A_8 K_1(\sigma_0 h), \quad (25)$$

where η_{cv} , η_{cd} and η_{dv} are defined as follows:

$$\eta_{cv} = i \frac{\sigma_0}{\sigma_c} \frac{S - i\omega\epsilon_0}{\omega\epsilon_0}, \quad \eta_{cd} = i \frac{\sigma_d}{\sigma_c} \frac{S - i\omega\epsilon_0}{\omega\epsilon_0 \kappa_d}, \quad \eta_{dv} = \frac{\kappa_d \sigma_0}{\sigma_d}. \quad (26)$$

The arbitrary constant A_1 needed for the determination of the longitudinal electric field inside the beam region and for the calculation of longitudinal impedance is obtained by simultaneously solving the system of Eqs. (18–25); namely,

$$E_z^{r \leq a}(\vec{r}, \omega) = -i \frac{Z_0 k_z I_0(\sigma_0 a) I_0(\sigma_0 r) e^{ik_z z}}{2\pi \gamma_0^2 \beta_0} \left[\frac{f_1 f_3}{f_4} \frac{\alpha_{12} - \alpha_{22}}{\alpha_{11} \alpha_{22} - \alpha_{12} \alpha_{21}} - f_2 + \frac{K_0(\sigma_p a)}{I_0(\sigma_p a)} \right], \quad (27)$$

where the parameters in Eq. (27) are given by the following relations:

$$\alpha_{11} = \frac{K_0(\sigma_d d)}{I_0(\sigma_d d)} - \frac{f_5}{f_4}, \quad \alpha_{22} = \eta_{cd} \left[\frac{K_1(\sigma_c d)}{I_1(\sigma_d d)} + \frac{f_7}{f_6} \frac{I_1(\sigma_c d)}{I_1(\sigma_d d)} \right] \quad (28)$$

$$\alpha_{12} = - \left[\frac{K_0(\sigma_c d)}{I_0(\sigma_d d)} - \frac{f_7}{f_6} \frac{I_0(\sigma_c d)}{I_0(\sigma_d d)} \right], \quad \alpha_{21} = - \left[\frac{f_5}{f_4} + \frac{K_1(\sigma_d d)}{I_1(\sigma_d d)} \right] \quad (29)$$

$$f_1 = \frac{K_0(\sigma_d b)}{I_0(\sigma_0 b)} - \frac{f_5}{f_4} \frac{I_0(\sigma_d b)}{I_0(\sigma_0 b)}, \quad f_2 = \frac{K_0(\sigma_0 b)}{I_0(\sigma_0 b)} - \frac{f_3}{f_4} \frac{I_0(\sigma_d b)}{I_0(\sigma_0 b)} \quad (30)$$

$$f_3 = \frac{K_1(\sigma_0 b)}{I_1(\sigma_0 b)} + \frac{K_0(\sigma_0 b)}{I_0(\sigma_0 b)}, \quad f_4 = \frac{I_0(\sigma_d b)}{I_0(\sigma_0 b)} - \eta_{dv} \frac{I_1(\sigma_d b)}{I_1(\sigma_0 b)} \quad (31)$$

$$f_5 = \frac{K_0(\sigma_d b)}{I_0(\sigma_0 b)} + \eta_{dv} \frac{K_1(\sigma_d b)}{I_1(\sigma_0 b)} \quad (32)$$

$$f_6 = \frac{I_0(\sigma_c h)}{K_0(\sigma_0 h)} + \eta_{cv} \frac{I_1(\sigma_c h)}{K_1(\sigma_0 h)} \quad (33)$$

$$f_7 = \frac{K_0(\sigma_c h)}{K_0(\sigma_0 h)} - \eta_{cv} \frac{K_1(\sigma_c h)}{K_1(\sigma_0 h)} \quad (34)$$

Longitudinal Impedance and Transmission

Longitudinal electric impedance will now be calculated as a volume integral over the beam current by assuming a circular accelerator of circumference L [1, 2]:

$$\begin{aligned} Z_{\parallel}^{(\text{total})}(\omega, S) &= -\frac{1}{q_0^2} \int_{V_b} d^3 r \vec{E}^{(r \leq a)}(\vec{r}, \omega) \cdot \vec{j}^*(\vec{r}, \omega) \\ &= -\frac{1}{q_0^2} \int_0^L dz \int_0^{2\pi} d\theta \int_0^a dr r E_z^{(r \leq a)}(\vec{r}, \omega) j^*(\vec{r}, \omega). \end{aligned} \quad (35)$$

Substituting for E_z and j results in the following expression for the electric impedance:

$$Z_{\parallel}^{(\text{total})}(\omega, S) = i \frac{n Z_0 I_0^2(\sigma_0 a)}{\beta_0 \gamma_0^2} \left[\frac{f_1 f_3}{f_4} \frac{\alpha_{12} - \alpha_{22}}{\alpha_{11} \alpha_{22} - \alpha_{12} \alpha_{21}} - f_2 + \frac{K_0(\sigma_0 a)}{I_0(\sigma_0 a)} \right], \quad (36)$$

where $Z_0 = 1/\epsilon_0 c$ is the vacuum impedance and n denotes the harmonic number which is related to the ring radius R by the relation $n = k_z R$ [1, 2].

The resistive-wall part of the longitudinal electric impedance $Z_{\parallel}^{(rw)}(\omega, S)$ is as follows:

$$Z_{\parallel}^{(rw)}(\omega, S) = Z_{\parallel}^{(\text{total})}(\omega, S) - Z_{\parallel}^{(\text{total})}(\omega, S \rightarrow \infty), \quad (37)$$

where $Z_{\parallel}^{(rw)}(\omega, S \rightarrow \infty)$ accounts for the absence of resistivity and represents the space-charge part of the electric impedance.

The longitudinal transmission coefficient $\tau_{||}$ of the resistive cylindrical pipe is obtained as the ratio of the transmitted to incident field amplitudes [2] and can be written as follows:

$$\tau_{||} = \frac{(\alpha_{11} - \alpha_{21}) \left[K_0(\sigma_c h) - \frac{f_7}{f_6} I_0(\sigma_c h) \right]}{\left(\frac{f_5}{f_4} (\alpha_{12} - \alpha_{22}) - (\alpha_{11} \alpha_{22} - \alpha_{12} \alpha_{21}) \right) I_0(\sigma_d d) - (\alpha_{22} - \alpha_{12}) K_0(\sigma_d d)} . \quad (38)$$

Numerical Examples

We obtained analytically closed form expressions for longitudinal electric impedance and transmission coefficient of a resistive cylindrical pipe of a conducting wall of finite thickness t_c [Eqs. (36–38)]. The conducting wall is coated from inside by a dielectric of thickness t_d . We also obtained the electromagnetic fields excited by an off-axis motion of a point source.

In Fig. 2, the transmission coefficient τ [Eq. (38)] has been visualized as a function of the conducting wall thickness normalized to the skin

depth t_c/δ_s , where $\delta_s = \sqrt{2/(\mu_0 S \omega)}$. As in Fig. 2, Fig. 3 shows the transmission coefficient τ as a function of t_c/δ_s using logarithmic scale. Representative machine parameters used in the numerical estimations in Figs. 2 and 3 are: circumference $L = 125$ m, pipe radius $b = 10$ cm, beam radius $a = 5$ cm, dielectric layer with $t_d = 3$ μm and $\kappa_d = 6$, injection energy $\gamma_0 = 1.02$, harmonic number $n = 5$, reference frequency $\omega_0 = \beta_0 c/R = 2.41 \times 10^6$ rad/s, $\omega = n\omega_0$, wall conductivity $S = 1.1 \times 10^6$ ($\Omega \text{ m}$)⁻¹ and $\delta_s = 0.31$ mm.

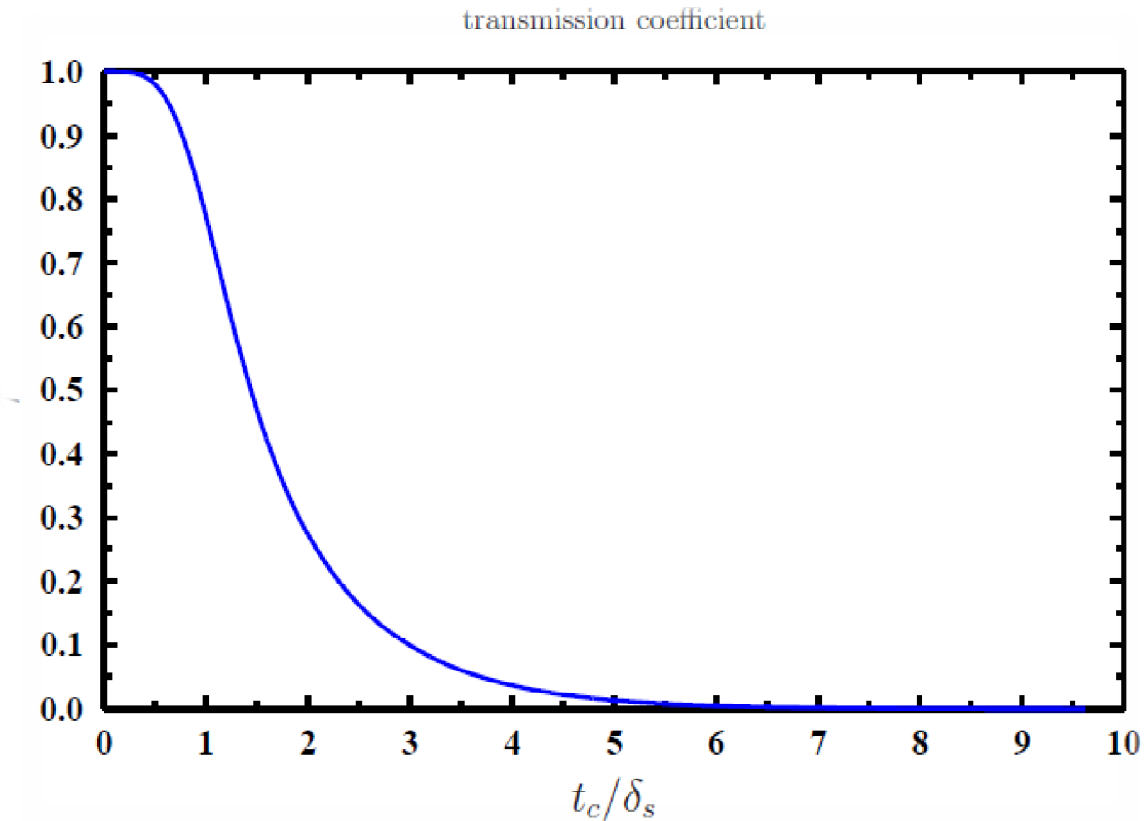


FIG. 2. Transmission coefficient τ as a function of the conducting wall thickness t_c/δ_s . The parameters used are: circumference $L = 125$ m, pipe radius $b = 10$ cm, beam radius $a = 5$ cm, dielectric thickness $t_d = 3$ μm and $\kappa_d = 6$, injection energy $\gamma_0 = 1.02$, harmonic number $n = 5$ and reference frequency $\omega_0 = 2.41 \times 10^6$ rad/s.

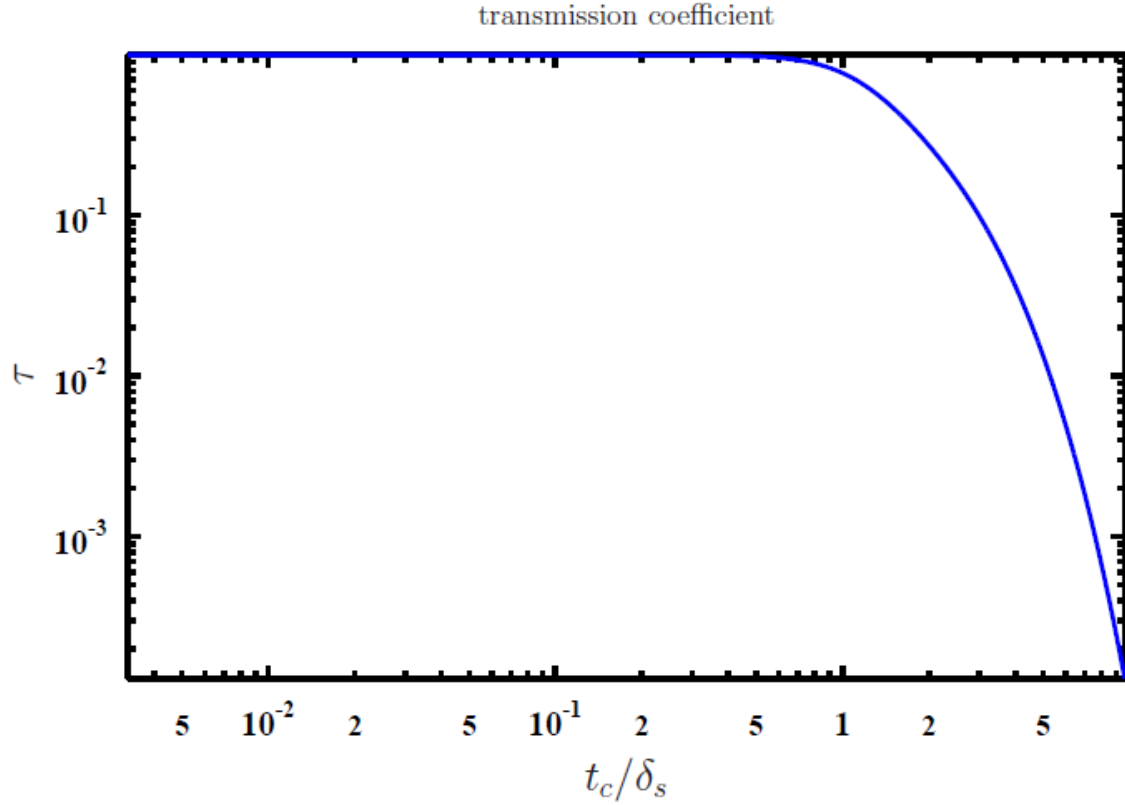


FIG. 3. Transmission coefficient τ (log scale) as a function of the normalized conducting wall thickness t_c/δ_s . The parameters used are: circumference $L = 125$ m, pipe radius $b = 10$ cm, beam radius $a = 5$ cm, dielectric thickness $t_d = 3$ μm and $\kappa_d = 6$, injection energy $\gamma_0 = 1.02$, harmonic number $n = 5$ and reference frequency $\omega_0 = 2.41 \times 10^6$ rad/s.

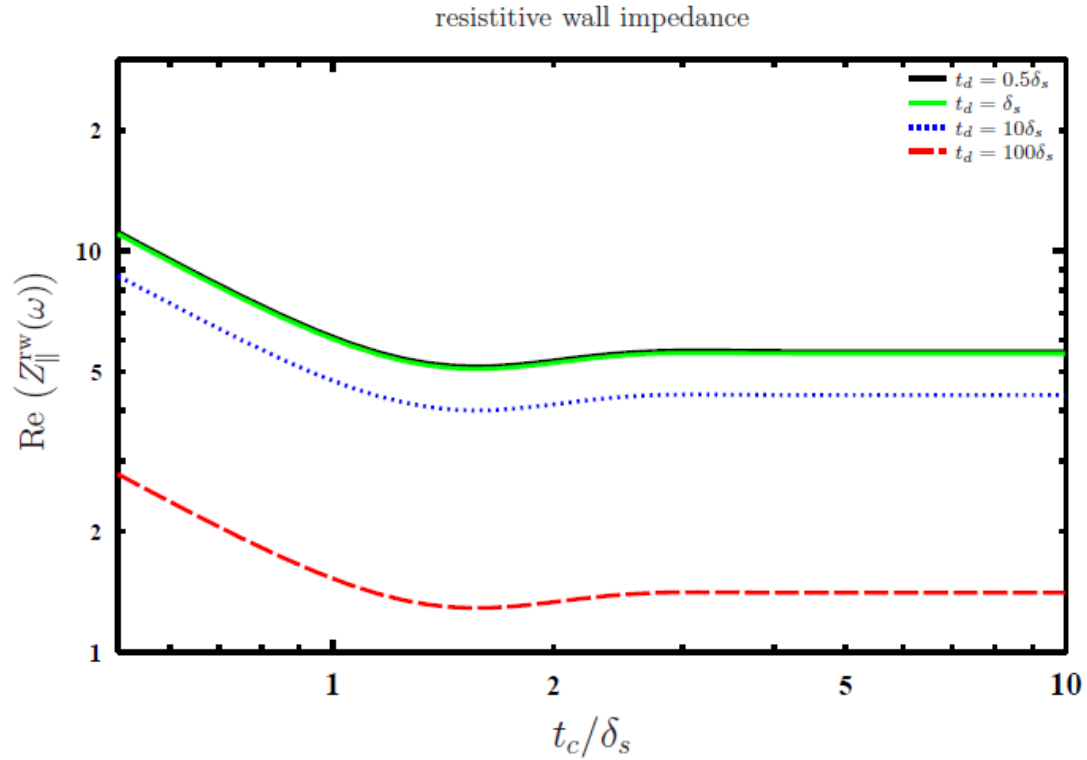


FIG. 4. Real part of the resistive-wall impedance in Ω as a function of the conducting wall thickness t_c/δ_s . The parameters used are: circumference $L = 125$ m, pipe radius $b = 10$ cm, beam radius $a = 5$ cm, dielectric constant $\kappa = 6$, injection energy $\gamma_0 = 1.02$, harmonic number $n = 5$ and reference frequency $\omega_0 = 2.41 \times 10^6$ rad/s.

As can be seen in Figs. 2 and 3, the pipe wall is transparent at wall thicknesses t_c less than the skin depth δ_s . At $t_c = \delta_s$, about 0.77% of the incident field penetrates the pipe. By increasing the wall thickness, we observe that only 0.25 % of the incident field can penetrate at $t_c = 2\delta_s$. For standard operation, less than one percent of the field penetrates for $t_c > 5\delta_s$ and field penetration becomes vanishingly small in the thick wall limit. This numerical example shows the importance of the shielding issue in the design of accelerators. Detailed knowledge of the accelerator environment and detailed beam

parameters are important in determining the required wall thicknesses needed to shield the wall effectively in order to reduce noise and pipe heating.

Fig. 4 shows, in log-scale, the real part of the resistive-wall impedance of Eq. (37) measured in Ohms as a function of the conducting wall thickness normalized to the skin depth; namely, t_c/δ_s . By varying the dielectric thickness t_d , we observe a suppression in resistive-wall impedance with increasing t_d . As expected, the thick wall limit is reached for $t_c > \delta_s$.

Conclusion

Very good shielding of electromagnetic fields can be achieved by thin metallic walls of thicknesses of the order of few skin penetration depths. Exact field matching has been used to calculate the excited electromagnetic fields and the corresponding longitudinal electric impedance and transmission coefficient. The derived analytical expressions for resistive-wall impedance and transmission have been numerically visualized for some relevant parameters. The validity of the analytical expressions presented in this work is restricted to thin-ring particle beams with a jump discontinuity at $r = a$. In future work, different beam-pipe geometries can be used to investigate

impedance and transmission for other beam distributions (RF sources).

The effect of the dielectric thickness t_d on the transmission coefficient is found to be negligibly small, while it leads to a suppression of the resistive-wall impedance for large values of t_d [see Fig.3]. From many numerical runs, we also observed a weak dependance on the dielectric constant κ_d ; a result which is already reported in literature [15]. In numerically investigating impedances of multi-layered pipes, the analytical results presented in this work for transmission coefficient and resistive-wall impedance will hopefully be useful in benchmarking numerical codes.

References

- [1] Al-Khateeb, A.M., Boine-Frankenheim, O., Hofmann, I. and Ru-molo, G., Phys. Rev. E, 63 (2001) 026503.
- [2] Al-Khateeb, A.M., Boine-Frankenheim, O., Hasse, R.W. and Hofmann, I., Phys. Rev. E, 71 (2005) 026501.
- [3] Schelkunoff, A., "Electromagnetic Waves", 2nd ed., (D. Van Nostrand Company, Inc, 1943).
- [4] Krinski, S., Podobedov, B. and Gluckstern, R.L., Phys. Rev. ST Accel. Beams, 7 (2004) 114401.
- [5] Metral, E., Zotter, B. and Slavant, B., IEEE Particle Accelerator Conference, June (2007), p.4216, ISSN 1944-4680.
- [6] Hahn, H., Phys. Rev. ST Accel. Beams, 13 (2010) 012002.
- [7] Zhilichev, Y., IEEE Trans. Supercond., 23 (2013) 8201810.
- [8] Biancacci, N. et al., Phys. Rev. ST Accel. Beams, 17 (2014) 021001.
- [9] Cherenkov, P.A., Doklady Akademii Nauk SSSR, 2: 451. Reprinted in Selected Papers of Soviet Physicists, Usp. Fiz. Nauka, 93 (1967) 385.
- [10] Sbornike, V. et al., Nauka, (1999), p. 149-153. (Ref. Archived October 22, 2007, at the Wayback Machine).
- [11] Genevet, P., Wintz, D., Ambrosio, A., She, A., Blanchard, R. and Capasso, F., Nature Nanotechnology, 10 (2015) 804809.
- [12] Jackson, J.D., "Classical Electrodynamics", 3rd ed., (Wiley, New York, 1998).
- [13] Collin, R.E., "Foundations of Microwave Engineering", 2nd ed., (McGraw - Hill, N. Y., 1992) pp.108–111.
- [14] Pozar, D.M., "Microwave Engineering", Ch. 5, (Addison - Wesley, 1990).
- [15] Wang, T.-S. F. and Kurennoy, S., Phys. Rev. STAB, 4 (2001) 104201.

Authors Index

A. Aldrabee.....	127
A. M. Al-Khateeb	165
A. Wriekat.	127
A.M. Gbadebo.	153
F. Abudanah	127
Hamed S. Hamadneh.....	117
J. A. Rabi.	153
K. AbuSaleem.....	127
M. A. Olaoye	139
M. F. Agbesi.	139
M. Mahdavi.	143
M. S. Bawa'aneh.....	165
M. Tarawneh.....	127
Manal J. Abdallah.....	117
Molham M. Eyadeh	117
N. Laham.....	165
O. A. Jegede	139
O. A. Mustapha.....	153
O. O. Ajayi.	139
Omar A. Al-Khdirat.....	117
R. M. A. Azzam.....	113
T. J. Aluko.	139
V. Makinde.	153

Subject Index

Average effective dose	139
Ayyubid-Mamluk pottery	127
Cylindrical pipe	165
Effective dose	139, 153
Electrical impedance	165
Fuel gain.....	143
Gamma ray spectrometry	117
Groundwater.....	153
Hazard indices	117
Human exposure	153
Indoor radon concentration.....	139
Interference.....	113
Isobaric.....	143
Isochoric	143
PCA.....	127
Polarization.....	113
Radionuclides	117, 153
Radon concentration	153
Reflection	113
Self-sustaining burn	143
Semi-quantitative	127
Soil	117
Spark-ignition	143
SR-XRF.....	127
Thin films	113
Transmission coefficient	165
Udhruh	127
Wave guides	165

المراجع: يجب طباعة المراجع بأسطر مزدوجة ومرقمة حسب تسلسلها في النص. وتكتب المراجع في النص بين قوسين مربعين. ويتم اعتماد اختصارات الدوريات حسب نظام Wordlist of Scientific Reviewers.

الجدول: تعطى الجداول أرقاماً متسلسلة يشار إليها في النص. ويجب طباعة كل جدول على صفحة منفصلة مع عنوان فوق الجدول. أما الحواشي التفسيرية، التي يشار إليها بحرف فوقي، فتكتب أسفل الجدول.

الرسوم التوضيحية: يتم ترقيم الأشكال والرسومات والرسومات البيانية (المخططات) والصور، بصورة متسلسلة كما وردت في النص.

تقبل الرسوم التوضيحية المستخرجة من الحاسوب والصور الرقمية ذات النوعية الجيدة بالأبيض والأسود، على أن تكون أصيلة وليست نسخة عنها، وكل منها على ورقة منفصلة ومعرفة برقمها بالمقابل. ويجب تزويد المجلة بالرسومات بحجمها الأصلي بحيث لا تحتاج إلى معالجة لاحقة، وألا تقل الحروف عن الحجم 8 من نوع Times New Roman، وألا تقل سماكة الخطوط عن 0.5 وبكثافة متجانسة. ويجب إزالة جميع الألوان من الرسومات ما عدا تلك التي ستنتشر ملونة. وفي حالة إرسال الرسومات بصورة رقمية، يجب أن تتوافق مع متطلبات الحد الأدنى من التمايز (1200 dpi Resolution) لرسومات الأبيض والأسود الخطية، و 600 dpi للرسومات باللون الرمادي، و 300 dpi للرسومات الملونة. ويجب تخزين جميع ملفات الرسومات على شكل (jpg)، وأن ترسل الرسوم التوضيحية بالحجم الفعلي الذي سيظهر في المجلة. وسواء أرسل المخطوط بالبريد أو عن طريق الشبكة (Online)، يجب إرسال نسخة ورقية أصلية ذات نوعية جيدة للرسومات التوضيحية.

مواد إضافية: تشجع المجلة الباحثين على إرفاق جميع المواد الإضافية التي يمكن أن تسهل عملية التحكيم. وتشمل المواد الإضافية أي اشتقاق رياضية مفصلة لا تظهر في المخطوط.

المخطوط المنقح (المعدل) والأقراص المدمجة: بعد قبول البحث للنشر وإجراء جميع التعديلات المطلوبة، فعلى الباحثين تقديم نسخة أصلية ونسخة أخرى مطابقة للأصلية مطبوعة بأسطر مزدوجة، وكذلك تقديم نسخة إلكترونية تحتوي على المخطوط كاملاً مكتوباً على Microsoft Word for Windows 2000 أو ما هو استجد منه. ويجب إرفاق الأشكال الأصلية مع المخطوط النهائي المعدل حتى لو تم تقديم الأشكال إلكترونياً. وتخزن جميع ملفات الرسومات على شكل (jpg)، وتقدم جميع الرسومات التوضيحية بالحجم الحقيقي الذي ستظهر به في المجلة. ويجب إرفاق قائمة ببرامج الحاسوب التي استعملت في كتابة النص، وأسماء الملفات على قرص مدمج، حيث يعلم القرص بالاسم الأخير للباحث، وبالرقم المرجعي للمخطوط والمراسلة، وعنوان المقالة، والتاريخ. ويحفظ في مغلف واقٍ.

حقوق الطبع

يُشكّل تقديم مخطوط البحث للمجلة اعترافاً صريحاً من الباحثين بأن مخطوط البحث لم يُنشر ولم يُقدّم للنشر لدى أي جهة أخرى كانت وبأي صيغة ورقية أو إلكترونية أو غيرها. ويشتترط على الباحثين ملء نموذج ينصّ على نقل حقوق الطبع لتصبح ملكاً لجامعة اليرموك قبل الموافقة على نشر المخطوط. ويقوم رئيس التحرير بتزويد الباحثين بنموذج نقل حقوق الطبع مع النسخة المُرسلة للتنقيح. كما ويُمنع إعادة إنتاج أي جزء من الأعمال المنشورة في المجلة من دون إذن خطي مُسبق من رئيس التحرير.

إخلاء المسؤولية

إن ما ورد في هذه المجلة يعبر عن آراء المؤلفين، ولا يعكس بالضرورة آراء هيئة التحرير أو الجامعة أو سياسة اللجنة العليا للبحث العلمي أو وزارة التعليم العالي والبحث العلمي. ولا يتحمل ناشر المجلة أي تبعات مادية أو معنوية أو مسؤوليات عن استعمال المعلومات المنشورة في المجلة أو سوء استعمالها.

الفهرسة: المجلة مفهرسة في:

1- Emerging Sources Citation Index (ESCI)

معلومات عامة

المجلة الأردنية للفيزياء هي مجلة بحوث علمية عالمية متخصصة مُحكمة تصدر بدعم من صندوق دعم البحث العلمي، وزارة التعليم العالي والبحث العلمي، عمان، الأردن. وتقوم بنشر المجلة عمادة البحث العلمي والدراسات العليا في جامعة اليرموك، إربد، الأردن. وتنتشر البحوث العلمية الأصلية، إضافة إلى المراسلات القصيرة Short Communications، والملاحظات الفنية Technical Notes، والمقالات الخاصة Feature Articles، ومقالات المراجعة Review Articles، في مجالات الفيزياء النظرية والتجريبية، باللغتين العربية والإنجليزية.

تقديم مخطوط البحث

تقدم البحوث عن طريق إرسالها إلى البريد الإلكتروني : jjp@yu.edu.jo

تقديم المخطوطات إلكترونياً: اتبع التعليمات في موقع المجلة على الشبكة العنكبوتية.

ويجري تحكيمُ البحوث الأصلية والمراسلات القصيرة والملاحظات الفنية من جانب مُحكمين اثنين في الأقل من ذوي الاختصاص والخبرة. وتُشجّع المجلة الباحثين على اقتراح أسماء المحكمين. أما نشر المقالات الخاصة في المجالات الفيزيائية النشطة، فيتم بدعوة من هيئة التحرير، ويُشار إليها كذلك عند النشر. ويُطلب من كاتب المقال الخاص تقديم تقرير واضح يتسم بالدقة والإيجاز عن مجال البحث تمهيداً للمقال. وتنتشر المجلة أيضاً مقالات المراجعة في الحقول الفيزيائية النشطة سريعة التغير، وتشجّع كاتبي مقالات المراجعة أو مُستكثبيها على إرسال مقترح من صفحتين إلى رئيس التحرير. ويُرفق مع البحث المكتوب باللغة العربية ملخص (Abstract) وكلمات دالة (Keywords) باللغة الإنجليزية.

ترتيب مخطوط البحث

يجب أن تتم طباعة مخطوط البحث ببنت 12 نوعه Times New Roman، وبسطر مزدوج، على وجه واحد من ورق A4 (21.6 × 27.9 سم) مع حواشي 3.71 سم، باستخدام معالج كلمات ميكروسوفت وورد 2000 أو ما استُجد منه. ويجري تنظيم أجزاء المخطوط وفق الترتيب التالي: صفحة العنوان، الملخص، رموز التصنيف (PACS)، المقدمة، طرق البحث، النتائج، المناقشة، الخلاصة، الشكر والعرفان، المراجع، الجداول، قائمة بدليل الأشكال والصور والإيضاحات، ثم الأشكال والصور والإيضاحات. وتُكتب العناوين الرئيسة بخط غامق، بينما تُكتب العناوين الفرعية بخط مائل.

صفحة العنوان: وتشمل عنوان المقالة، أسماء الباحثين الكاملة وعناوين العمل كاملة. ويكتب الباحث المسؤول عن المراسلات اسمه مشاراً إليه بنجمة، والبريد الإلكتروني الخاص به. ويجب أن يكون عنوان المقالة موجزاً وواضحاً ومعبراً عن فحوى (محتوى) المخطوط، وذلك لأهمية هذا العنوان لأغراض استرجاع المعلومات.

الملخص: المطلوب كتابة فقرة واحدة لا تزيد على مائتي كلمة، موضحة هدف البحث، والمنهج المتبع فيه والنتائج وأهم ما توصل إليه الباحثون.

الكلمات الدالة: يجب أن يلي الملخص قائمة من 4-6 كلمات دالة تعبر عن المحتوى الدقيق للمخطوط لأغراض الفهرسة.

PACS: يجب إرفاق الرموز التصنيفية، وهي متوفرة في الموقع <http://www.aip.org/pacs/pacs06/pacs06-toc.html>.

المقدمة: يجب أن توضّح الهدف من الدراسة وعلاقتها بالأعمال السابقة في المجال، لا أن تكون مراجعة مكثفة لما نشر (لا تزيد المقدمة عن صفحة ونصف الصفحة مطبوعة).

طرائق البحث (التجريبية / النظرية): يجب أن تكون هذه الطرائق موضحة بتفصيل كاف لإتاحة إعادة إجرائها بكفاءة، ولكن باختصار مناسب، حتى لا تكون تكراراً للطرائق المنشورة سابقاً.

النتائج: يستحسن عرض النتائج على صورة جداول وأشكال حيثما أمكن، مع شرح قليل في النص ومن دون مناقشة تفصيلية.

المناقشة: يجب أن تكون موجزة وتركز على تفسير النتائج.

الاستنتاج: يجب أن يكون وصفاً موجزاً لأهم ما توصلت إليه الدراسة ولا يزيد عن صفحة مطبوعة واحدة.

الشكر والعرفان: الشكر والإشارة إلى مصدر المنح والدعم المالي يكتبان في فقرة واحدة تسبق المراجع مباشرة.

Jordan Journal of

PHYSICSAn International Peer-Reviewed Research Journal issued by the
Support of the Scientific Research Support Fund

Published by the Deanship of Research & Graduate Studies, Yarmouk University, Irbid, Jordan

Name: الأسم:
 Specialty:..... التخصص:
 Address: العنوان:
 P.O. Box:..... صندوق البريد:
 City & Postal Code: المدينة/الرمز البريدي:
 Country: الدولة:
 Phone: رقم الهاتف:
 Fax No:..... رقم الفاكس:
 E-mail:..... البريد الإلكتروني:
 No. of Subscription: عدد الاشتراكات:
 Method of Payment: طريقة الدفع:
 Amount Enclosed:..... المبلغ المرفق:
 Signature: التوقيع:

Cheques should be paid to Deanship of Research and Graduate Studies - Yarmouk University.

I would like to subscribe to the Journal
For

- ☐ One Year
☐ Two Years
☐ Three Years

One Year Subscription Rates

	Inside Jordan	Outside Jordan
Individuals	JD 8	€ 40
Students	JD 4	€ 20
Institutions	JD 12	€ 60

Correspondence**Subscriptions and Sales:**

Prof. Ibrahim O. Abu Al-Jarayesh
 Deanship of Research and Graduate Studies
 Yarmouk University
 Irbid – Jordan
Telephone: 00 962 2 711111 Ext. 2075
Fax No.: 00 962 2 721121



جامعة اليرموك



المملكة الأردنية الهاشمية

المجلة الأردنية
للفيزياء

مجلة بحوث علمية عالمية متخصصة محكمة
تصدر بدعم من صندوق دعم البحث العلمي

المجلة الأردنية
للفيزياء
مجلة بحوث علمية عالمية محكمة

المجلد (10)، العدد (3)، كانون الأول 2017م / ربيع الأول 1439هـ

المجلة الأردنية للفيزياء: مجلة علمية عالمية متخصصة محكمة تصدر بدعم من صندوق دعم البحث العلمي، عمان، الأردن، وتصدر عن عمادة البحث العلمي والدراسات العليا، جامعة اليرموك، إربد، الأردن.

رئيس التحرير:

ابراهيم عثمان أبو الجرايش
قسم الفيزياء، جامعة اليرموك، إربد، الأردن.
ijaraysh@yu.edu.jo

هيئة التحرير:

ضياء الدين محمود عرفة
رئيس جامعة آل البيت، المفرق، الأردن.
darafah@ju.edu.jo
نبيل يوسف أيوب
رئيس الجامعة الأمريكية في مادبا، مادبا، الأردن.
nabil.ayoub@gju.edu.jo
جميل محمود خليفة
قسم الفيزياء، الجامعة الأردنية، عمان، الأردن.
jkalifa@ju.edu.jo
سامي حسين محمود
قسم الفيزياء، الجامعة الأردنية، عمان، الأردن.
s.mahmood@ju.edu.jo
نهاد عبدالرؤوف يوسف
قسم الفيزياء، جامعة الأميرة سمية للتكنولوجيا، عمان، الأردن
o.n.yusuf@psut.edu.jo
مروان سليمان الموسى
قسم الفيزياء، جامعة مؤتة، الكرك، الأردن.
mmousa@mutah.edu.jo
أكرم عبد المجيد الروسان
قسم الفيزياء التطبيقية، جامعة العلوم والتكنولوجيا الأردنية، إربد، الأردن.
akram@just.edu.jo
محمد خالد الصغير
قسم الفيزياء، الجامعة الهاشمية، الزرقاء، الأردن.
msugh@hu.edu.jo

سكرتير التحرير: مجدي الشناق

ترسل البحوث إلى العنوان التالي:

الأستاذ الدكتور إبراهيم عثمان أبو الجرايش
رئيس تحرير المجلة الأردنية للفيزياء
عمادة البحث العلمي والدراسات العليا، جامعة اليرموك
إربد، الأردن

هاتف 00 962 2 7211111 فرعي 2075

E-mail: jjp@yu.edu.jo Website: <http://Journals.yu.edu.jo/jjp>